

Technische Universität München
Institut für Energietechnik

Lehrstuhl für Thermodynamik

Computation of the Thermoacoustic Driving Capability of Rocket Engine Flames with Detailed Chemistry

Attila Lehel Török

Vollständiger Abdruck der von der Fakultät für Maschinenwesen der Technischen Universität München zur Erlangung des akademischen Grades eines

DOKTOR-INGENIEURS

genehmigten Dissertation.

Vorsitzender:

Univ.-Prof. P.-S. Koutsourelakis, Ph.D.

Prüfer der Dissertation:

1. Univ.-Prof. Dr.-Ing. T. Sattelmayer

2. Prof. Dr ir J. Steelant, Universität Leuven

Die Dissertation wurde am 16.09.2014 bei der Technischen Universität München eingereicht und durch die Fakultät für Maschinenwesen am 17.11.2015 angenommen.

Danksagung

Die vorliegende Arbeit entstand am Lehrstuhl für Thermodynamik der Technischen Universität München und wurde durch die Network Partnering Initiative von ESA-ESTEC gefördert.

Besonders danke ich Herrn Prof. Dr.-Ing. Thomas Sattelmayer für das mir entgegengebrachte Vertrauen, für die gewährten wissenschaftlichen Freiräume und die mir - sowohl während meiner Zeit als wissenschaftlicher Mitarbeiter als auch danach - bereitgestellten Rahmenbedingungen. Weiterhin danke ich Herrn Prof. Dr. ir Johan Steelant für die Betreuung meiner Arbeit während meines zwölfmonatigen Forschungsaufenthaltes bei ESTEC, die fachlichen Impulse und die freundliche Übernahme des Koreferats. Herrn Prof. Phaedon-Stelios Koutsourelakis Ph.D. danke ich für die Übernahme des Prüfungsvorsitzes.

Sowohl während meiner Zeit am Lehrstuhl als auch bei ESTEC habe ich viele Menschen kennengelernt, denen ich in vielerlei Hinsicht dankbar bin. Bei administrativen Angelegenheiten konnte ich mich stets auf die Unterstützung in den Sekretariaten verlassen. Auf der Suche nach Hilfe bei technischen Problemen wurde ich oft im Büro der Admins, aber auch immer wieder in den Werkstätten fündig. Und bei fachlichen Fragen haben mich die Anregungen meiner Kolleginnen und Kollegen vorangebracht. Von der kameradschaftlichen Unterstützung und dem freundschaftlichen Umgang untereinander hat aber nicht nur mein Wissen sondern auch meine Gemütslage immer wieder profitiert. Die Zeit am Lehrstuhl wird mir daher, trotz schwieriger Phasen, stets in schöner Erinnerung bleiben.

Mein größter Dank gilt aber meiner wunderbaren Familie. Insbesondere meinen Eltern für die Unterstützung während der langen Jahre meiner Ausbildung und den Zuspruch den ich schon mein ganzes Leben erfahren darf; und meiner Ehefrau und meinen Kindern für all das Glück das wir teilen dürfen und all die Freude die sie in mein Leben bringen. Ihnen möchte ich dieses Buch von ganzem Herzen widmen.

München, im Juli 2016

Attila Török

Kurzfassung

Berechnungstools für die Vorhersage von Verbrennungsinstabilitäten in Raketentriebwerken benötigen ein Modell für die Wärmefreisetzung der Flamme. In dieser Arbeit werden die Parameter eines solchen Modells für eine H₂-O₂ Flamme mittels CFD und detaillierter Chemie berechnet. Diverse Anregungsmethoden und ihr Einfluss auf die Wärmefreisetzung werden untersucht. Simulationen mit der so errechneten Flammentransferfunktion bestätigen das Auftreten der in Experimenten beobachteten Instabilitäten.

Abstract

Computational tools for the prediction of combustion instabilities in rocket engines require a heat release model to represent the flame. In this thesis parameters of such a model are calculated for a H₂-O₂ flame using CFD with detailed chemistry. Several excitation methods are considered and their effects on heat release fluctuations are analyzed. Simulations with the thus determined flame transfer function confirm the appearance of thermoacoustic oscillations that were observed in experiments.

Contents

- Contents..... i**
- List of Tables..... v**
- List of Figures vii**
- Nomenclature.....xiii**
- 1 Introduction 1**
 - 1.1 Space Flight Today 1
 - 1.2 Combustion Instabilities in Rocket Engines 2
 - 1.3 This Thesis..... 5
- 2 Computational Fluid Dynamics 7**
 - 2.1 Basic Equations of Fluid Dynamics 7
 - 2.2 Closing the System of Equations..... 8
 - 2.2.1 Ideal Gases..... 8
 - 2.2.2 Real Gases 9
 - 2.3 Transport Properties 11
 - 2.4 Multicomponent Flow 14
 - 2.5 Mass Diffusion 17
 - 2.6 Turbulence 20
 - 2.7 Solver Theory in ANSYS CFX 21
 - 2.8 Non-Reflecting Boundary Conditions in CFX..... 23
- 3 Combustion 25**
 - 3.1 Chemical Kinetics..... 25
 - 3.1.1 System of Equations..... 25
 - 3.1.2 Thermodynamic Data 26
 - 3.1.3 Chemical Rate Expressions..... 26

3.1.4	Third Body Reactions.....	27
3.1.5	Pressure-Dependent Rate Constant.....	28
3.1.6	Intermediate Complex-Forming Bimolecular Reactions	29
3.1.7	Stiff System of ODEs	30
3.1.8	Choice of Reaction Mechanism	32
3.2	Turbulence-Chemistry Interaction.....	33
3.2.1	Assumed PDF of Temperature.....	33
3.2.2	Assumed PDF of Composition.....	35
3.2.3	Mean Chemical Production Rates	36
3.2.4	Additional Equations in the Flow Solver	37
3.3	Tabulation.....	38
3.3.1	Tabulation of Chemical Kinetics.....	38
3.3.2	Tabulation of Turbulence-Chemistry Interaction.....	40
3.4	Approach for the Simulation of Combustion in this Thesis.....	41
4	Simulation of Combustion in Reacting Flows	45
4.1	Constant Volume Reactor.....	45
4.1.1	Validation of the implementation in CFX.....	45
4.1.2	Influence of the Reaction Mechanism.....	47
4.2	Laminar Non-Premixed Flame.....	49
4.2.1	Experimental Data.....	50
4.2.2	Numerical Simulation.....	50
4.2.3	Results	51
4.3	Turbulent Flame at Atmospheric Pressure	53
4.3.1	Experimental Data.....	53
4.3.2	Numerical Simulation.....	54
4.3.3	Simulation with Detailed Chemistry	55
4.3.4	Influence of Tabulation	59
4.3.5	Influence of Reaction Mechanism.....	61
4.3.6	Influence of Turbulence Chemistry Interaction	62
4.4	Turbulent Flame at High Pressure.....	68

4.4.1	Experimental Data.....	68
4.4.2	Numerical Simulation.....	69
4.4.3	Simulation with Detailed Chemistry.....	70
4.4.4	Influence of Reaction Mechanism.....	72
4.4.5	Influence of Turbulence-Chemistry Interaction.....	73
5	Preliminary Studies for the Simulation of Instabilities.....	77
5.1	The Hydrodynamic System.....	77
5.1.1	Experimental Data and Theoretical Background.....	77
5.1.2	Set-Up for Numerical Simulations.....	79
5.1.3	Results in ANSYS CFX.....	80
5.2	Heat Release and Pressure.....	82
5.2.1	Set-Up for Numerical Simulation.....	82
5.2.2	Results in ANSYS CFX.....	84
5.3	Methods for Simulation of Instabilities.....	87
5.3.1	Velocity Excitation.....	87
5.3.2	Velocity and Pressure Excitation.....	87
5.3.3	Pressure Excitation.....	90
6	Simulation of Instabilities on a Rocket Engine Flame.....	93
6.1	Experimental Data.....	93
6.2	Basic Numerical Setup.....	94
6.3	Simulation without Excitation.....	95
6.4	Velocity Excitation.....	100
6.5	Pressure Excitation.....	103
6.5.1	Mass Source and Sink Terms on Boundaries.....	103
6.5.2	Moving Wall.....	107
6.5.3	Fluctuating Pressure as Input to Chemical Kinetics.....	109
6.5.4	Conclusion for Pressure Excitation.....	111
6.6	Extension to Fluctuating Inlet Mass Flow Rates.....	112
7	Evaluation of Combustion Instabilities.....	117
7.1	Mean Flow Properties.....	118

7.2	Acoustics Analysis without Combustion	119
7.3	Thermoacoustic Analysis with Heat Release	121
7.3.1	Flame Transfer Function	121
7.3.2	Shape Function	122
7.3.3	Simulation and Results	122
8	Summary and Conclusions	127
	References	131
A	Appendix	141
A.1	Material Properties	141
A.2	Reaction Mechanisms	142

List of Tables

Table 1.1:	Classification of combustion instabilities	3
Table 2.1:	Overview of transport phenomena	12
Table 2.2:	Coefficients from Neufeld et al. [67] for calculating $\Omega^{(l,s)*}$	13
Table 4.1:	Flame and flow conditions [14]	54
Table 4.2:	Dimensions (axial×radial) of grids used for grid convergence	56
Table 4.3:	Operating conditions of RCM-3 test case [37]	68
Table 4.4:	Dimensions of the Mascotte single injector illustrated in Figure 4.26.....	69
Table 6.1:	Operating conditions for combustion chamber BKD with injector head L42 [35]	93
Table 7.1:	Operating conditions for the simulation of the combustion chamber in CFX	118
Table 7.2:	Parameters for FTF from the simulation of a single flame in BKD L42	121
Table A.1:	Molar masses of the species involved in combustion	141
Table A.2:	Coefficients for the polynomials in equations (3.3), (3.4) and (3.5) in the lower temperature range (up to 1000 K)	141
Table A.3:	Coefficients for the polynomials in equations (3.3), (3.4) and (3.5) in the upper temperature range (above 1000 K).....	141
Table A.4:	Reaction mechanism from Jachimowski [47], modified by Wilson and MacCormack [105].	142
Table A.5:	Efficiency factors $\neq 1$ for the mechanism in Table A.4.	142
Table A.6:	Reaction mechanism from Ó Conaire et al. [69].	143
Table A.7:	Troe parameters for the mechanism in Table A.6.....	143
Table A.8:	Efficiency factors $\neq 1$ for the mechanism in Table A.6.	144

List of Figures

Figure 2.1:	Comparison of equations of state for oxygen at 154.18 K.....	10
Figure 2.2:	Illustration of terms and definitions in CFX (with modifications from [4])	19
Figure 2.3:	Simplified solution flow chart for inner iterations within ANSYS CFX [4]	21
Figure 2.4:	Illustration of finite volume methods: The cell-centered or volume-filled method (left) and the cell-vertex or element-filled method (right)	23
Figure 4.1:	Temperature curves for a constant volume reactor from CFX and SENKIN with the mechanism from Jachimowski [47] at 1 bar	46
Figure 4.2:	Total energy equation and thermal energy equation compared	47
Figure 4.3:	Reaction mechanisms compared based on the progress of a constant volume reactor in CFX at 1 bar	47
Figure 4.4:	Reaction mechanisms compared based on the progress of a constant volume reactor in CFX at 60 bar	48
Figure 4.5:	Ignition time plotted against pressure for a constant volume reactor starting at 1100 K and 60 bar	48
Figure 4.6:	Ignition time plotted against the equivalence ratio for a constant volume reactor starting at 1100 K and 60 bar.....	49
Figure 4.7:	Schematic illustration of the laminar burner.....	50
Figure 4.8:	OH mass fraction plot from simulation with detailed chemistry and diffusion.....	52
Figure 4.9:	Abel-transformed OH* image from experiment.....	52
Figure 4.10:	N ₂ mass fraction plot from simulation with detailed chemistry and diffusion.....	53

Figure 4.11: Schematic illustration of the vitiated coflow burner [14]	54
Figure 4.12: OH mass fraction plots from simulations of the flame from Cabra et al. [14] (grids from top: XS, S, M, L, XL)	55
Figure 4.13: Temperature plots from simulations of the flame from Cabra et al. [14] (grids from top: XS, S, M, L, XL)	56
Figure 4.14: OH mass fraction profiles for $z/d = 1, 8, 11, 14$ and 26 (from top left) from simulations of the flame from Cabra et al. [14]	57
Figure 4.15: Temperature profiles for $z/d = 1, 8, 11, 14$ and 26 (from top left) from simulations of the flame from Cabra et al. [14]	58
Figure 4.16: OH mass fraction plots from simulations of the flame from Cabra et al. [14]; top: 20 mf-steps, middle: 30 mf-steps, bottom: no tabulation	60
Figure 4.17: Temperature plots from simulations of the flame from Cabra et al. [14]; top: 20 mf-steps, middle: 30 mf-steps, bottom: no tabulation	60
Figure 4.18: OH mass fraction plots from simulations of the flame from Cabra et al. [14]; above: Jachimowski, below: Ó Conaire	61
Figure 4.19: Temperature plots from simulations of the flame from Cabra et al. [14]; above: Jachimowski [47], below: Ó Conaire et al. [69]	62
Figure 4.20: OH mass fraction plots from simulations of the flame from Cabra et al. [14]; from the top: 1. no PDF, 2. T-PDF, 3. Y-PDF, 4. T- and Y-PDF	63
Figure 4.21: Temperature plots from simulations of the flame from Cabra et al. [14]; from the top: 1. no PDF, 2. T-PDF, 3. Y-PDF, 4. T- and Y-PDF	64
Figure 4.22: I_T plot from the simulation of the flame from Cabra et al. [14] with T- and Y-PDF	65
Figure 4.23: σ_Y^2 plot from the simulation of the flame from Cabra et al. [14] with T- and Y-PDF	65
Figure 4.24: Influence of assumed PDF approaches on OH mass fraction profiles at $z/d = 1, 8, 11, 14$ and 26 (from top left) from simulations of the flame from Cabra et al. [14]	66

Figure 4.25: Influence of assumed PDF approaches on temperature profiles at $z/d = 1, 8, 11, 14$ and 26 (from top left) from simulations of the flame from Cabra et al. [14]	67
Figure 4.26: Mascotte single injector geometry [68].....	69
Figure 4.27: OH* contours from the Mascotte single injector test case [37] (top: average emission image, bottom: Abel-transformed emission image).....	71
Figure 4.28: OH mass fractions plot from the simulation of the Mascotte single injector test case [37]	71
Figure 4.29: Temperatures in the Mascotte single injector [37] in experiment and simulations.....	72
Figure 4.30: OH mass fraction plots from simulations of the Mascotte single injector test case [37]; above: Jachimowski [47], below: Ó Conaire et al. [69]	73
Figure 4.31: OH mass fraction plots from simulations of the Mascotte single injector test case [37]; above: no PDF, below: T-PDF.....	73
Figure 4.32: I_T plot from the simulation of the Mascotte single injector test case [37] with consideration of the assumed PDF of temperature only	74
Figure 4.33: σ_Y^2 plot from the simulation of the Mascotte single injector test case [37] with consideration of the assumed PDF of temperature only	75
Figure 5.1: The near wall velocity overshoot (Richardson's annular effect).....	79
Figure 5.2: Phase shift for $\omega^* = 1950$ and $p_{\max} = 10$ Pa at one Opening, with $\Delta t = 0.01$ s	80
Figure 5.3: Numerical simulation and analytical solution for $\omega^* = 1950$ and $p_{\max} = 10$ Pa at one Opening.....	81
Figure 5.4: Illustration of domain and grid in the Rijke tube at the position of the heater	83
Figure 5.5: Oscillating pressure in the Rijke tube at the position of the heater	84

Figure 5.6:	Oscillating pressure and velocity in the Rijke tube at the position of the heater	84
Figure 5.7:	Oscillating pressure and heat flux in the Rijke tube at the position of the heater	85
Figure 5.8:	Oscillating pressure and heat flux in the Rijke tube at the position of the heater at limit cycle	86
Figure 5.9:	FFT gain of the calculated heat release at the limit cycle in Figure 5.9.....	86
Figure 5.10:	Fluctuation of pressure and transverse velocity at $x = 0.20$ m and $y = -0.75$ m.....	88
Figure 5.11:	Distribution of pressure (above) and velocity (below) in the computational domain	89
Figure 5.12:	Cross section of a 3D computational domain with illustration of the translational periodic boundaries (left) and of the pressure excitation methods (right)	90
Figure 6.1:	OH mass fraction plots from simulations of OP7 of a single L42 flame on a 2D grid	96
Figure 6.2:	Temperature plots from simulations of OP7 of an L42 flame on a 2D grid	97
Figure 6.3:	OH mass fraction plots from simulations of OP3 and OP7	97
Figure 6.4:	Temperature plots from simulations of OP3 and OP7 with.....	98
Figure 6.5:	Plot of volumetric heat release from simulation of OP7 of the L42 flame	98
Figure 6.6:	Distribution of heat release along the axis from simulation of OP7 of the L42 flame	98
Figure 6.7:	O ₂ mass fraction plot from simulation of OP7 of an L42 flame on a quasi-2D grid.....	99
Figure 6.8:	Streamlines from simulation of OP7 of an L42 flame on a quasi-2D grid.....	99
Figure 6.9:	Pressure field for the first transverse mode in a cylindrical chamber	101

Figure 6.10: Distribution of temperature and OH mass fraction along the axis of an L42 flame with and without velocity excitation.....	102
Figure 6.11: Fluctuation of global heat release over time as response to velocity excitation	103
Figure 6.12: Outlet pressure and heat release from excitation with mass source terms on boundaries	105
Figure 6.13: Pressure amplitudes and phase offsets resulting from fluctuating mass source terms on boundaries.....	106
Figure 6.14: Outlet pressure and heat release from excitation with a moving wall at OP7	107
Figure 6.15: Rayleigh-Integral along the axis from simulation of OP7 resulting from excitation with moving wall (at 1 bar and 10000 Hz).....	108
Figure 6.16: Pressure amplitudes and phase offsets resulting from excitation with a moving wall	109
Figure 6.17: Fluctuating pressure and heat release from excitation in external routine.....	109
Figure 6.18: Rayleigh-Integral along the axis from simulation of OP7 with excitation (1 bar, 10000 Hz).....	110
Figure 6.19: Phase shift between pressure and heat release fluctuations for OP3 and OP7	111
Figure 6.20: Symbolic illustration of the domains used for a propellant feed system	112
Figure 6.21: Outlet pressure and corresponding mass flow rates at the outlet.....	113
Figure 6.22: Rayleigh-Integral along the axis from simulation of OP7 with fluctuating mass flow rates and pressure excitation (1 bar, 10000 Hz).....	114
Figure 7.1: Schematic illustration of the domain for the calculation of mean flow properties in CFX.....	118
Figure 7.2: Mach number plot from simulation of OP3 in CFX.....	119

List of Figures

Figure 7.3:	Temporal evolution of pressure at a virtual microphone in PIANO for OP3 without combustion being considered.....	120
Figure 7.4:	FFT gain of the pressure signal from Figure 7.3.....	120
Figure 7.5:	Shape function resembling the form of heat release distribution along the axis from the simulation of an L42 flame OP3.....	122
Figure 7.6:	Temporal evolution of pressure at a virtual microphone in PIANO for OP3 with combustion being considered after 1.0 ms	123
Figure 7.7:	FFT gain of the pressure signal from Figure 7.6.....	123
Figure 7.8:	Pressure distribution at inflow and combustion chamber wall for OP3	124
Figure 7.9:	Pressure distribution at the faceplate for OP3.....	124

Nomenclature

Symbols

a	$\text{m}^5/(\text{kg s}^2)$	parameter of the Redlich-Kwong equation
a		Troe parameter
a_0	$\text{m}^5/(\text{kg s}^2)$	gas constant for Redlich-Kwong equation
a_1, a_2, \dots, a_7	(various)	coefficients of fits to thermodynamic data
A	(various)	pre-exponential factor
A	m^2	area
A		area of clipped part of temperature PDF
A, B, \dots, H		coefficients of the collision integral
A, B, \dots, D		parameters of the shape function
b	m^3/kg	gas constant of Redlich-Kwong equation
B		representing an expression (see species PDF)
B		representing an expression (see Richardson's effect)
c	m^3/kg	correction coefficient for Redlich-Kwong equation
c	mol/m^3	molar concentration
c		shift parameter of the broadening factor
c	m/s	speed of sound
c_p	$\text{J}/(\text{kg K})$	specific heat capacity at constant pressure
C_p	$\text{J}/(\text{mol K})$	molar heat capacity at constant pressure
C_T		modeling constant of the σ_T transport equation
C_Y		modeling constant of the σ_Y transport equation
$C_{\varepsilon 1}, C_{\varepsilon 2}$		k- ε -model constants in the ε transport equation
C_μ		k- ε -model constant of turbulent viscosity
d		asymmetry parameter of the broadening factor
d, D	m	diameter
D	m^2/s	kinematic diffusivity (diffusion coefficient)
\mathcal{D}_{AB}	m^2/s	binary diffusion coefficient

Nomenclature

e		Euler's number
E	J/mol	activation energy in the rate constant
f		general function
f	Hz	frequency
F		general collision broadening factor
F_{cent}		broadening factor at the center of the fall-off curve
h	J/kg	specific enthalpy
H	J/mol K	molar enthalpy
i		imaginary unit: $i^2 = -1$
I_T		fluctuation intensity
J		Bessel function
k	m^2/s^2	turbulent kinetic energy
k	J/K	Boltzmann constant: $k = 1.380 \times 10^{-23}$ J/K
k	1/m	wave number
k_0	(various)	forward rate coefficient at the low-pressure limit
k_∞	(various)	forward rate coefficient at the high-pressure limit
k_b	(various)	backward rate constant
k_f	(various)	forward rate constant
K	m/s^2	constant for Richardson's annular effect
K		table coordinate
K_c	(various)	equilibrium constant based on molar concentration
K_p	(various)	equilibrium constant based on partial pressures
L	m	length
Le		Lewis number
m		sum of stoichiometric coefficient
\dot{m}	kg/s	mass flow rate
M	kg/mol	molar mass
Ma		Mach number
n		modified exponent of Redlich-Kwong equation
n		interaction parameter
N		width parameter of the broadening factor
N		number of elements in a set
O	m^2	control surface
p	Pa	pressure

P		probability density function
\mathcal{P}	$\text{kg}/(\text{m}^2 \text{ s})$	turbulence production
Pr		Prandtl number
q	$\text{mol}/(\text{m s})$	rate-of-progress variable
\dot{Q}	W	heat flux or heat release
r, R	m	radius
R	$\text{J}/(\text{kg K})$	specific gas constant
R_u	$\text{J}/(\text{mol K})$	universal gas constant: $R_u = 8.314 \text{ J}/(\text{mol K})$
sf		shape function
S	$\text{J}/(\text{mol K})$	molar entropy
S	mol/kg	summand
S_E	$\text{kg}/(\text{m s}^3)$	energy source term
\mathbf{S}_M	$\text{kg}/(\text{m}^2 \text{ s}^2)$	momentum source term (vector)
S_s	$\text{kg}/(\text{m}^3 \text{ s})$	species source term
t	s	time
T	K	temperature
T^*, T^{**}, T^{***}	K	Troe parameters
$\mathcal{T}_1, \mathcal{T}_2, \mathcal{T}_3, \mathcal{T}_4$	(various)	terms for calculation of mean chemical production rate
u	m/s	(axial) velocity; component of velocity vector
\mathbf{U}	m/s	velocity vector
V	m^3	control volume
v	m^3/kg	specific volume
v_m	m^3/mol	molar volume
x, X		Cartesian coordinate
X		mole fraction
\mathbf{y}	(various)	representing a vector of dependent variables
y, Y		Cartesian coordinate
Y		mass fraction
z		Cartesian coordinate

Greek Letters

α	m^2/s	thermal diffusivity
α		third-body efficiency factor
β		temperature exponent in the rate constant
β		parameter of species PDF
γ		heat capacity ratio or isentropic exponent
Γ	Pa s	molecular diffusion coefficient
Γ		gamma function
δ		Dirac delta function
δ		Kronecker delta
ε	J	Lennard-Jones potential well depth
ε	m^2/s^3	turbulent eddy dissipation
λ	$\text{W}/(\text{m K})$	thermal conductivity
μ	Pa s	dynamic viscosity
ν	m^2/s	kinematic viscosity
ν		stoichiometric coefficient, $\nu = \nu'' - \nu'$
ν'		reactant stoichiometric coefficient
ν''		product stoichiometric coefficient
ρ	kg/m^3	density
σ	\AA	Lennard-Jones collision diameter/hard sphere diameter
$\sigma_k, \sigma_\varepsilon$		model constants in the transport equation of k and ε
σ_T^2	K^2	temperature variance
σ_Y^2		species variance
τ	Pa	viscous stress tensor
τ	s	time lag
τ_t	s	turbulent time scale
ϕ	<i>(various)</i>	general scalar variable
ϕ		equivalence ratio
ω		acentric factor
ω	$1/\text{s}$	angular frequency
$\dot{\omega}$	$\text{mol}/(\text{m}^3 \text{s})$	chemical production rate
$\Omega^{(l,s)*}$		collision integral

Subscripts

0	initial values
<i>a</i>	variable at the baseline level
atm	corresponding to state at one standard atmosphere
<i>b</i>	variable at the elevated level
<i>c</i>	value at the critical point
<i>exc</i>	excitation
<i>i, j</i>	general indices
<i>ip</i>	integration point
<i>k</i>	species or component of multicomponent mixture
<i>m</i>	molar quantity
<i>r</i>	corresponding to reaction r
<i>red</i>	reduced (dimensionless) quantity
<i>ref</i>	reference value
<i>s</i>	species or component of multicomponent mixture
<i>t</i>	turbulent
<i>tot</i>	total
<i>v</i>	volumetric

Superscripts

0	Corresponding to standard state
o	representing values from the last time step
oo	representing values from the last but one time step
<i>T</i>	transpose of a matrix
^	representing sample space variables in turbulence-chemistry interaction
^	amplitude of a periodic variable
–	mean of a periodic variable
–	representing mean part of a Reynolds averaged quantity
~	representing mean part of a Favre averaged quantity
'	fluctuating part of a periodic variable
'	representing fluctuating part of a variable in Reynolds averaging
"	representing fluctuating part of a variable in Favre averaging
*	dimensionless variable

Acronyms

APE	Acoustic Perturbation Equation
BKD	BrennKammer D
CAA	Computational Aero Acoustics
CEL	CFX Expression Language
CFD	Computational Fluid Dynamics
CFL	Courant–Friedrichs–Lewy
DLR	Deutsches Zentrum für Luft- und Raumfahrt
EDM	Eddy Dissipation Model
ESA	European Space Agency
ESTEC	European Space Research and Technology Centre
FFT	Fast Fourier Transform
FTF	Flame Transfer Function
JBR	Junction Box Routine
LEE	Linearized Euler Equations
LOX	Liquid OXYgen
LPRE	Liquid Propellant Rocket Engine
MMH	MonoMethylHydrazine
MMS	Memory Management System
NASA	National Aeronautics and Space Administration
NIST	National Institute of Standards and Technology
NTO	Nitrogen TetrOxide
ODE	Ordinary Differential Equation
OP	Operating Point
PDF	Probability Density Function
PIANO	Perturbation Investigation of Aerodynamic NOise
PISO	Pressure Implicit with Split Operator
RANS	Reynolds Averaged Navier-Stokes
SIMPLE	Semi-Implicit Method for Pressure-Linked Equations
SIMPLEC	SIMPLE Consistent
UDMH	Unsymmetrical DiMethylHydrazine

1 Introduction

1.1 Space Flight Today

Over the past 100 years the presence of mankind in space has developed from mere dreams and ideas to a matter of course in our everyday lives and is almost indispensable in many scientific disciplines. Navigation and communication satellites help to improve terrestrial infrastructure and are available from even the remotest regions of our planet. Earth monitoring satellites are used e.g. for meteorology, oceanography or geodesy. The view from space back to our Earth offers the possibility to explore the environment we live in and to gain awareness for the steps necessary for its conservation. Space observatories offer the possibility to study distant regions of the universe without the obstructive effects of Earth's atmosphere. Space probe missions target astronomical objects in our solar system and help to further explore the extraterrestrial universe. The near-weightlessness on board of space laboratories or space stations allow for fundamental research e.g. in material sciences, physics, biology or medicine. For all these purposes there is a constant need for means of transport to bring freight and humans to space. Given the expensive payloads, not to mention invaluable human lives, it is apparent that a reliable means of transport is necessary.

Today and in the foreseeable future the most relevant option to enter space is to use chemical rockets. In launch vehicles usually liquid propellants are used for the main engine, while solid propellants are mostly employed in boosters to increase the payload capacity of the spacecraft. Among the liquid propellants the group called earth-storable is easiest to be handled, since these propellants are in liquid state at standard conditions. Typically employed combinations usually use N_2O_4 (nitrogen tetroxide, short: NTO) as an oxidizer and N_2H_2 (hydrazine) or one of its organic compounds (MMH, UDMH, Aerozin 50) as a fuel. The advantage of these propellants is that they are hypergolic, i.e. they react on contact, which makes them favorable for applications where multiple restarts are required. Cryogenic propellant combinations in contrast need an additional device

for ignition. A further disadvantage is the low temperature which is required to keep the propellants liquefied. The high specific impulse (highest among all propellants in practical use) on the other hand makes the cryogenic combination of hydrogen and liquid oxygen (LOX) very attractive. It has been successfully used for the propulsion of various rocket engines, among which Vulcain (main engine for Ariane 5) and the Space Shuttle Main Engine are probably most famous. It will also be employed in future engines, currently e.g. in Vinci, the new upper stage engine of Ariane 5. The work described in this thesis focuses on this cryogenic combination. For the sake of completeness a third group of liquid propellants referred to as cryogenic-storable is also worth mentioning, since it has been frequently applied in rocket engines. It is the combination of a cryogenic (usually LOX) and an earth-storable propellant (usually RP-1, a form of kerosene).

In a liquid propellant rocket engine (LPRE) usually a turbo-pump is used to bring propellants from their tanks to the combustion chamber. Pressure-fed systems are only employed for low thrust application and are mostly irrelevant in launch vehicles. In engines using the H_2/O_2 combination propellants are generally injected through coaxial injectors into the combustion chamber, with oxygen in the core and hydrogen in the annulus. In large engines usually several hundreds of these coaxial injectors are mounted on the faceplate, so that this injector head – due to its resemblance – is usually also referred to as shower head. Through the exothermic reaction of the propellants within the combustion chamber heat is released. Burnt gases exit the combustion chamber through the de Laval nozzle, which converts thermal energy to directed kinetic energy. For a detailed description of LPRE elements and rocket propulsion in general the book of Sutton and Biblarz [97] can be recommended, which served as a valuable source for the composition of this introductory chapter.

1.2 Combustion Instabilities in Rocket Engines

A major factor in the reliability of a LPRE is its design with respect to stability of combustion. Combustion instabilities have probably been an issue ever since the first rocket engines were developed. Over the decades they have caused several setbacks in engine development programs and even flight failures. In the beginning of the 1960s the development of the F-1 engine of the Saturn V rocket (e.g. flown in the Apollo program) was strongly delayed due to combustion instabilities. And it was combustion instabilities in one of the Viking engines that

resulted in a failure of the second flight of the Ariane 1 rocket (flight L02). The awareness of combustion instabilities started when amplitudes in test firings grew large enough so that they were detectable by the human ear – instrumentation at that time was only designed for steady state operation. With the cognition that combustion instabilities might possibly be responsible for engine failures, extensive investigation on the subject started. And most of the fundamental research on the matter was done in the 1950s and 1960s already. A first important step was the classification of instabilities (see Table 1.1) and the reasons responsible for their formation. The classification by frequency ranges has historical reasons. It would be much more decisive to do the classification e.g. by the mechanisms responsible for the instabilities. The frequency ranges given in the table are therefore rather intended as guidelines and vary depending on the size of engine components.

Table 1.1: *Classification of combustion instabilities*

Class	Frequency Range (Hz)	Manifestation
Low Frequency ("chugging")	10-400	wave motion in the feed system, negligible (or no) wave motion in the combustion chamber
Intermediate Frequency ("buzzing")	400-1000	wave motion in the feed system and in the combustion chamber, but without acoustical resonance in the chamber
High Frequency ("screaming")	>1000	wave motion in the combustion chamber, with phase and frequency corresponding to an acoustic mode in the chamber

Combustion instabilities at low and intermediate frequencies may cause vibrations of the engine and could possibly result in damage to parts of the rocket or the payload. Furthermore they can also trigger high frequency instabilities, which are considered to be the most destructive. At high frequency instabilities, especially at the prevalent tangential modes, heat transfer is quickly increased so considerably that it may cause a sudden melting of chamber walls and injectors. Thus it is evident that measures had to be taken in order to prevent the formation of combustion instabilities.

Therefore, to decrease the probability of their occurrence additional tests were introduced in the design process of LPREs. In the beginning these tests consisted of a large number of experiments. Operating conditions for the configurations to be considered were varied over a wide range. The configuration which showed combustion instabilities in the fewest cases was then considered to be the most stable. This design for statistical stability relied on the presence of some kind of natural trigger. However, it was not safe to assume that during flight there are no further triggers as those already present during testing. Therefore, instead of waiting for combustion instabilities to occur spontaneously, developers started to use various devices to trigger combustion instabilities artificially, e.g. gas injection, pulse guns or bombs. Transients imposed by either of these devices had to diminish when the source of the disturbance was removed. An engine was only considered to be dynamically stable if it was always able to return to stable operation after any kind of transients.

Once combustion instabilities were detected design changes had to be made in order to eliminate them. One approach was aiming at reducing the energy that is fed to the wave by making changes to e.g. the injector or the chamber geometry. Another approach was aiming at introducing damping devices, such as acoustic liners or baffles, to increase energy loss. With the experience gained over the years many suggestions and design criteria were formulated that have proven to be successful in the past.

In 1972 all findings on the subject of combustion instabilities in LPREs were collected by NASA in an extensive reference book [40], which is usually referred to as "SP-194". It is considered the standard work on the subject and up until today is cited in virtually all corresponding publications. From contributions to a course at the ESTEC site of ESA in 1993 on combustion instabilities in LPREs a text book was compiled [92]. It was intended to be a successor of NASA's SP-194 and aiming to summarize the state of the art on the subject at that time.

In the past more than 20 years since then research has continued, as combustion instability in LPREs has remained a complex phenomenon that is not fully mastered. Up until today only full-scale engine tests are able to detect acoustic instabilities securely. A reliable computational tool would help to reduce the amount of these costly experiments. At Lehrstuhl für Thermodynamik the CAA code called PIANO [18] has been chosen to be used for this purpose. Various activities have been focusing on extending PIANO's capabilities (see [65] and

[72]) and on applying the code for the evaluation of combustion chamber acoustics (see e.g. [48], [49] or [94]). PIANO requires a separate model for the heat release of the flame, which provides the thermoacoustic feedback when coupled to the acoustic field. The quality of this model is essential for the prediction capabilities of the code. Transient CFD simulations are used in order to calculate the parameters of such a model (see e.g. [91]). While in other activities ([91], [94]) EDM is used to account for combustion, in this thesis the computation of the dynamic heat release is carried out by using unsteady RANS simulations in combination with detailed chemistry.

1.3 This Thesis

Calculating chemical processes with a detailed reaction mechanism is very time consuming. In this thesis this is done in an external routine, while the flow itself is calculated in ANSYS CFX. In the external routine the assumed PDF approach is implemented and considered for turbulence-chemistry interaction. Tabulation methods which are able to reduce the required time for calculating the combustion process are also made available and their influence on the results is discussed. Comparison of a constant volume reactor in CFX with data generated by CHEMKIN [52] is used to show the proper implementation of reaction kinetics. Numerical results are compared with experimental data from Cabra et al. [14] and from the Mascotte test rig [36].

In a rocket combustion chamber hydrogen and oxygen are injected at temperatures below 100 K and pressures up to 200 bar. For oxygen these values are above its critical pressure and below its critical temperature. At high pressures and low temperatures the appearance of attractive forces between molecules (van der Waals forces) is the most significant effect. Two-parameter equations of state show good agreement with real gas behavior without increasing the computational effort significantly. Several of these equations are available in ANSYS CFX. In this thesis the equation of state introduced by Redlich and Kwong [85] has been selected to account for these forces when supercritical oxygen is present in simulations.

The identification of the source of combustion instabilities is always linked to the question of how heat release fluctuations couple with acoustic quantities like pressure or velocity. In order to produce self-excited thermoacoustic fluctuations in a rocket combustion chamber it would be necessary to model the entire

chamber geometry so that feedback mechanisms can emerge. However, the numerical simulation of combustion processes is very time consuming. Therefore it is not feasible to include an entire combustion chamber in the simulation. Alternatively the computational domain can be limited to a region around the flame from one injector only. In this case a forcing technique has to be developed that is able to excite the computational domain. One further advantage of this approach is that the influence of pressure and velocity fluctuations can be observed separately. In this work pressure and velocity excitation methods are considered and their applicability investigated. Results from numerical simulations were compared to data available from experiments of a model combustion chamber at DLR, which show self-excited thermoacoustic fluctuations [35]. Simulations with PIANO were conducted based on data available from experiments [35] and from numerical simulations.

The theoretical background required for the CFD simulations presented in this thesis is presented in chapter 2. An introduction to the theory of detailed chemistry that is required for the implementation in ANSYS CFX is given in chapter 3. Results from simulation of reactive flows without excitation are presented in chapter 4. In chapter 5 computations for the assessment of solver capabilities are presented and possible methods for excitation of a rocket engine flame are discussed. In chapter 6 one velocity excitation method and three pressure excitation methods are applied to the flame of the DLR model combustion chamber. In chapter 7 the stability of the same model combustion chamber is investigated with PIANO.

2 Computational Fluid Dynamics

In this chapter a brief introduction to the governing equations of computational fluid dynamics (CFD) is given. They follow the notation and terminology of the ANSYS CFX – Solver Theory Guide [4]. The scope is reduced to the equations relevant for this thesis. Further information on CFD and more detailed descriptions are available from various books on the topic (see e.g. Hirsch [44], Patankar [70], Pope [77] or White [104]).

2.1 Basic Equations of Fluid Dynamics

Three laws of conservation form the basis for fluid dynamics. These are the laws for the conservation of mass, momentum and energy. Here the corresponding equations are given in differential form. In the strict sense only the momentum conservation equations given in (2.2) are called "Navier-Stokes equations". However, it is common practice to use this term for the whole system of conservation equations as introduced in this section. For brevity they are given without the additional terms required for turbulent flows. The mass conservation equation, also referred to as the continuity equation, is:

$$\frac{\partial \rho}{\partial t} + \nabla \cdot (\rho \mathbf{U}) = 0 \quad (2.1)$$

The momentum equations are:

$$\frac{\partial(\rho \mathbf{U})}{\partial t} + \nabla \cdot (\rho \mathbf{U} \otimes \mathbf{U}) = -\nabla p + \nabla \cdot \boldsymbol{\tau} + \mathbf{S}_M \quad (2.2)$$

In this equation \mathbf{S}_M are the momentum source terms and $\boldsymbol{\tau}$ is the stress tensor:

$$\boldsymbol{\tau} = \mu \left(\nabla \mathbf{U} + (\nabla \mathbf{U})^T - \frac{2}{3} \delta \nabla \cdot \mathbf{U} \right) \quad (2.3)$$

The total energy equation is:

$$\frac{\partial(\rho h_{tot})}{\partial t} - \frac{\partial p}{\partial t} + \nabla \cdot (\rho \mathbf{U} h_{tot}) = \nabla \cdot (\lambda \nabla T) + \nabla \cdot (\mathbf{U} \cdot \boldsymbol{\tau}) + S_E \quad (2.4)$$

Total enthalpy h_{tot} is related to static enthalpy h by:

$$h_{tot} = h + \frac{1}{2} \mathbf{U}^2 \quad (2.5)$$

The thermal energy equation is an alternative formulation in which high-speed energy effects are neglected:

$$\frac{\partial(\rho h)}{\partial t} - \frac{\partial p}{\partial t} + \nabla \cdot (\rho \mathbf{U} h) = \nabla \cdot (\lambda \nabla T) + \mathbf{U} \cdot \nabla p + \boldsymbol{\tau} : \nabla \mathbf{U} + S_E \quad (2.6)$$

S_E is the energy source term and $\boldsymbol{\tau} : \nabla \mathbf{U}$ is called the viscous dissipation term. The thermal energy equation can help to avoid stability issues and is e.g. often preferred in transient liquid simulations [4]. This equation is particularly important to attain a solution in transient simulations of combustion at high pressure, in which oxygen is present as a real gas (see section 4.4 and chapter 6).

Transport properties such as dynamic viscosity μ or thermal conductivity λ can be related to thermodynamic properties (see section 2.3). Thus remain seven unknowns: density ρ , three components of the velocity vector \mathbf{U} , pressure p , temperature T and specific enthalpy h . The continuity equation, the three momentum equations and the energy equation provide a total of five conservation equations. Therefore two further equations are required to relate these quantities to each other (see section 2.2).

2.2 Closing the System of Equations

Two equations are needed to close the system of equations, one for density and one for enthalpy.

2.2.1 Ideal Gases

For ideal gases the ideal gas law applies:

$$p = \rho R T = \frac{R T}{v} \quad (2.7)$$

The equation used for enthalpy is:

$$h - h_{ref} = \int_{T_{ref}}^T c_p(T) dT \quad (2.8)$$

For ideal gases in CFX by default a 4th order polynomial is used for the specific heat capacity c_p as shown in equation (2.15). For ideal gases in CFX a table is

generated for enthalpy $h(T)$ according to equation (2.8). In case the thermal energy equation is selected the value of static enthalpy is known from solving the flow. With the reference values of enthalpy and temperature used for table generation static temperature T is extracted by table inversion. The same applies for the total energy equation with the only difference that instead of static values of enthalpy and temperature total values are used.

2.2.2 Real Gases

For ideal gases intermolecular forces can be neglected. For real gases in contrast they are important and have to be accounted for [1]. At high pressures and low temperatures the appearance of attractive forces between molecules (Van der Waals forces) is the most significant effect. Further real gas effects like dissociation, recombination, ionization and vibration of molecules are only relevant in the region of very high temperatures [90]. Within the flow solver they remain unconsidered in this thesis. Some of the effects are included through the use of detailed chemistry as introduced in chapter 3.

In LPRE hydrogen and oxygen are injected to the combustion chamber at temperatures lower than 100 K and pressures up to 200 bar. While for hydrogen with its critical point at $T_{c,H_2} = 33.18$ K and $p_{c,H_2} = 13.00$ bar it is appropriate to use ideal gas law, this is not the case for oxygen ($T_{c,H_2} = 154.18$ K and $p_{c,O_2} = 50.43$ bar). For oxygen in this region the ideal gas law cannot describe the relationship between pressure, temperature and density correctly (see Figure 2.1). Two-parameter equations of state show good agreement with real gas behavior without increasing the computational effort significantly. This makes them the most favored real gas equation of state in engineering applications. Generally the equation introduced by Redlich und Kwong [85] is regarded as one of the most accurate two-parameter equation of state. By default CFX uses a modified version (by Aungier [6]) of the Redlich-Kwong equation, which offers improved accuracy close to the critical point:

$$p = \frac{RT}{v - b + c} - \frac{a(T)}{v(v + b)} \quad (2.9)$$

The parameters a , b and c in this equation are gas specific constants and related to the critical values of temperature, pressure and specific volume of a given material as follows:

$$a(T) = a_0 T_{red}^{-n} \quad (2.10)$$

where $T_{red} = T/T_c$ is the reduced temperature (normalized by its value at the critical point) and:

$$a_0 = \frac{0.42747 R^2 T_c^2}{p_c} \quad (2.11)$$

$$b = \frac{0.08664 R T_c}{p_c} \quad (2.12)$$

$$c = \frac{R T_c}{p_c + \frac{a_0}{v_c(v_c + b)}} + b - v_c \quad (2.13)$$

The exponent n in equation (2.10) can be obtained by using the acentric factor ω as follows:

$$n = 0.4986 + 1.2735\omega + 0.4754\omega^2 \quad (2.14)$$

Substituting $n = 0.5$ and $c = 0$ in equation (2.9) yields the original form of the Redlich-Kwong equation. For many materials critical temperature, pressure, volume and acentric factor are stored in the materials database of CFX (from Poling et al. [75]). Data for other substances are for example available from the NIST database [55].

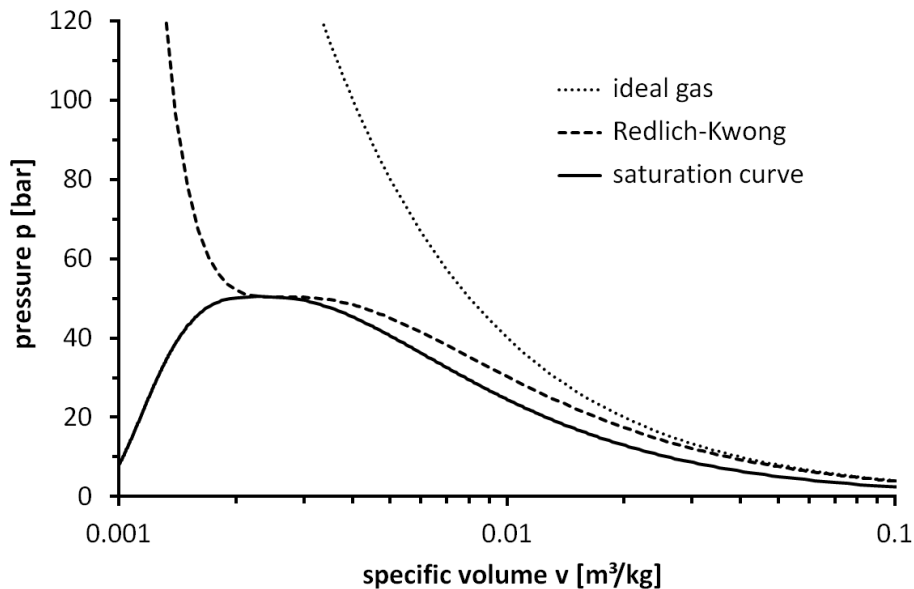


Figure 2.1: Comparison of equations of state for oxygen at 154.18 K

Figure 2.1 shows for oxygen at its critical temperature (154.18 K) a comparison between ideal gas law and the modified Redlich-Kwong equation of state. The saturation curve was generated with data from NIST [55].

For the evaluation of density CFX uses a property table $\rho(T, p)$, which is generated in a pre-processing step before the simulation is started. For this purpose ranges of temperature and pressure have to be specified in CFX Pre. Also a number has to be entered to state in how many equally spaced intervals the ranges are divided. With CFX-Post it is possible to visualize this table in order to detect regions where the discretization is not adequate.

When a material with the Redlich-Kwong equation of state is involved in the simulation, specific heat capacity is a function of temperature and pressure – see section 2.3. CFX thus generates a table for enthalpy $h(T, p)$ during pre-processing. When the thermal energy model is selected, static pressure p and static enthalpy h are known from solving the flow. During simulation static temperature T is then extracted from this table. In case the total energy equation is selected, the table is generated for total enthalpy instead. Finding temperature from enthalpy is more complicated then. Details of the procedure are described in the CFX documentation [4].

In simulations of combustion, where for oxygen the Redlich-Kwong equation of state is used (see section 4.4 and chapter 6), large ranges of temperature and pressure have to be covered. Despite the large number of table entries (up to 4 million per table) usually problems with these tables caused the crash of the simulations. A solution could only be obtained with the thermal energy model.

2.3 Transport Properties

A quite detailed description of all transport phenomena can be found in Bird et al. [10]. For the evaluation of transport properties in numerical simulation sometimes the work of Kee et al. [54] is referenced (e.g. by Smooke et al. [96]). This report is not available anymore, but the follow-up document (Kee et al. [50]) gives a very good description for the calculation of transport properties. An overview of the most important transport phenomena is given in Table 2.1. It is also known that mass can be transported through temperature gradients (Soret effect) and that energy can be transported through concentrations gradients. However, these effects are relatively small. Therefore they are usually not included in the simulation of combustion [103].

Table 2.1: Overview of transport phenomena

process	transport of	caused by gradients of	corresponding fluid property
heat conduction	energy	temperature	thermal diffusivity $\alpha = \lambda / \rho c_p$
viscosity	momentum	velocity	momentum diffusivity (kinematic viscosity) $\nu = \mu / \rho$
mass diffusion	mass	concentration	mass diffusivity (diffusion coefficient) \mathcal{D}_{AB}

For the specific heat capacity at constant pressure c_p it is possible to use a constant value. By default CFX uses the NASA format polynomials for ideal gases. With these polynomials c_p is a function of temperature:

$$\frac{c_p}{R} = a_{1s} + a_{2s}T + a_{3s}T^2 + a_{4s}T^3 + a_{5s}T^4 \quad (2.15)$$

Values for the coefficients are stored in the CFX materials database. Usually two sets of coefficients are supplied, one for temperatures up to 1000 K and one for temperatures above 1000 K.

In case a material with Redlich-Kwong equation of state (2.9) is employed in the simulation by default the "Zero Pressure Polynomial" option is used to model specific heat capacity. Coefficients for this 4th order polynomial are also supplied in the CFX materials database. This polynomial resembles the form of equation (2.15) but is only valid for the theoretical case that the gas is at an ideal state at zero pressure. Based on this polynomial and the equation of state CFX calculates a property table such that specific heat is a function of temperature and pressure $c_p(T, p)$.

For ideal gases in the CFX materials database constant values are specified for dynamic viscosity μ and thermal conductivity λ . Sutherland's formula is also available to specify these properties as a function of temperature. In this case further information has to be entered manually.

For real gases other options are selected by default [3]. Dynamic viscosity is evaluated from the simple formula:

$$\mu = 26.69 \cdot 10^{-6} \frac{\sqrt{MT}}{\Omega^{(2,2)*} \sigma^2} \quad (2.16)$$

This is based on kinetic gas theory (see [45]) and the hard sphere diameter σ in CFX is determined from the critical molar volume:

$$\sigma = 0.809 \sqrt[3]{v_{m,c}} \quad (2.17)$$

When the Rigid Non Interacting Sphere model is used, the collision integral $\Omega^{(2,2)*}$ is simply unity. For the Interacting Sphere model the value of the collision integral $\Omega^{(2,2)*}$ is evaluated from:

$$\Omega^{(l,s)*} = \frac{A}{(T_{red})^B} + \frac{C}{\exp(DT_{red})} + \frac{E}{\exp(FT_{red})} + \frac{G}{\exp(HT_{red})} \quad (2.18)$$

Coefficients for this accurate empirical equation are given by Neufeld et al. [67] as listed in Table 2.2.

Table 2.2: Coefficients from Neufeld et al. [67] for calculating $\Omega^{(l,s)*}$

(l,s)	A	B	C	D	E	F	G	H
(1,1)	1.06036	0.15610	0.19300	0.47635	1.03587	1.52996	1.76474	3.89411
(2,2)	1.6145	0.14874	0.52487	0.77320	2.16178	2.43787	-	-

The reduced temperature required for equation (2.18) is in this case calculated from the critical temperature T_c :

$$T_{red} = 1.2593 \frac{T}{T_c} \quad (2.19)$$

For thermal conductivity of real gases the modified Eucken-Model can be used in the form:

$$\frac{\lambda}{\mu c_v} = 1.32 + \frac{1.77R}{c_v} \quad (2.20)$$

This has also been derived from kinetic gas theory [75].

Information on the binary diffusion coefficient \mathcal{D}_{AB} (for diffusion between two species/components A and B) is given in section 2.5, along with further information on mass diffusion in general.

The fluid properties in the last column of Table 2.1 can be related to each other by dimensionless numbers (Prandtl, Schmidt and Lewis number):

$$\text{Pr} = \frac{\nu}{\alpha} \quad (2.21)$$

$$\text{Sc} = \frac{\nu}{\mathcal{D}_{AB}} \quad (2.22)$$

$$\text{Le} = \frac{\alpha}{\mathcal{D}_{AB}} \quad (2.23)$$

In numerical simulations it can be adequate to use a constant (mostly close to unity) for one of these dimensionless numbers, instead of having to evaluate all three fluid properties separately.

2.4 Multicomponent Flow

For a multicomponent fluid in CFX the conservation equation presented in section 2.1 are solved for the bulk motion of the fluid. All components share the same mean pressure, temperature and velocity [3]. The fluid properties depend on the composition of the multicomponent mixture. They are calculated based on the local mass fraction weighted average of the components' properties. For instance bulk viscosity is calculated as:

$$\mu = \sum_s^{N_s} Y_s \mu_s \quad (2.24)$$

Other fluid properties like specific heat at constant pressure, specific heat at constant volume and thermal conductivity are calculated accordingly.

For the transport of the components within the fluid additional equations are necessary. When a multi-component flow with N_s involved species is simulated in CFX, one component has to be chosen for which a constraint equation is solved. This makes sure that the sum of all mass fractions is equal to one. For each of the remaining $N_s - 1$ species one transport equation is solved. The transport equation of each species s has the form [4]:

$$\frac{\partial(\rho Y_s)}{\partial t} + \frac{\partial(\rho u_j Y_s)}{\partial x_j} = \frac{\partial}{\partial x_j} \left(\Gamma_{s_{eff}} \frac{\partial Y_s}{\partial x_j} \right) + S_s \quad (2.25)$$

where $\Gamma_{s_{eff}}$ is the effective molecular diffusion coefficient and S_s a source term.

In a turbulent flow density and mass fractions are averaged values (see section 2.6). The effective diffusion coefficient in equation (2.25) is calculated from the sum of molecular and turbulent diffusion:

$$\Gamma_{s_{eff}} = \Gamma_s + \frac{\mu_t}{Sc_t} \quad (2.26)$$

In turbulent (reactive) flow molecular transport is usually less important than turbulent transport [71]. Turbulent diffusion is dependent on the choice of the turbulent Schmidt number Sc_t and the model constants of the turbulence model (see section 2.6) which define turbulent viscosity μ_t . In this thesis the default values are used. The molecular diffusion coefficient in CFX is assumed to be:

$$\Gamma_s = \rho D_s \quad (2.27)$$

The kinematic diffusivity D_s of a component s can be set (e.g. according to equation (2.47) in section 2.5) in “Component Models” on the “Fluid Models” tab of the domain in CFX Pre for all component for which a transport equation is solved. If no value is specified, CFX uses bulk viscosity for all components of the fluid. This way all species have the same diffusivity:

$$\Gamma_s = \Gamma = \mu \quad (2.28)$$

This means that the Schmidt number is unity for all components:

$$Sc_s = \mu/\Gamma_s = 1 \quad (2.29)$$

This simplification has usually no large effect on the results, when the flow is turbulent. In a laminar flow, especially where the material properties of the components differ considerably, this simplification is not adequate. The available possibilities in CFX for that case are discussed in section 2.5.

For multicomponent fluids on the right hand side of the energy equation (see section 2.1) an additional term is employed:

$$\frac{\partial}{\partial x_j} \sum_s^{N_s} \Gamma_s h_s \frac{\partial Y_s}{\partial x_j} \quad (2.30)$$

The evaluation of this term is considerably simplified, when the species diffusivities are assumed to be:

$$\Gamma_s = \Gamma = \lambda/c_p \quad (2.31)$$

This corresponds to the Lewis number being one for each component:

$$Le_s = \lambda/(c_p \Gamma_i) = 1 \quad (2.32)$$

This simplification results in term (2.30) being simplified to:

$$\frac{\partial}{\partial x_j} \left(\frac{\lambda}{c_p} \frac{\partial h}{\partial x_j} \right) \quad (2.33)$$

For turbulent flow the assumption $Le_s = 1$ is usually as good as the common practice of using $Sc_s = 1$ for all components [4]. For fluids consisting of many components this simplification can significantly reduce numerical cost, as only one diffusion term has to be assembled [4]. Especially for laminar flow component dependant diffusivities have to be set. Section 2.5 provides more information on the topic.

Rules for mixing at high pressures and low temperatures are different from ideal mixing. For the calculation with gas mixtures Redlich and Kwong [85] suggested to determine the parameters a and b for their equation from:

$$b = \sum_s^{N_s} X_s b_s \quad (2.34)$$

$$a = a_1 X_1 + a_2 X_2 + \dots + 2a_{12} X_1 X_2 + \dots \text{ with } a_{12} = (a_1 a_2)^{1/2} \quad (2.35)$$

where X denotes mole fraction. Aungier [6] suggested using the following correlations for the modified equation:

$$T_c^{(1+n)} = \frac{\left[\sum_s^{N_s} X_s \sqrt{T_{c,s}^{(2+n)} / p_{c,s}} \right]^2}{\sum_s^{N_s} \frac{X_s T_{c,s}}{p_{c,s}}} \quad (2.36)$$

$$p_c = \frac{T_c}{\sum_s^{N_s} \frac{X_s T_{c,s}}{p_{c,s}}} \quad (2.37)$$

$$\omega = \sum_s^{N_s} X_s \omega_s \quad (2.38)$$

In CFX 11.0 it was not possible to implement these mixing rules. In version 12.0 a beta feature has been added that allows users to define arbitrary mixing rules. However, this feature and its effect on the simulation have not been examined in this thesis. The effect of real mixing rules on the simulation of supercritical combustion with EDM is examined by Poschner and Pfitzner (see e.g. [78] or [79]).

2.5 Mass Diffusion

In this section a brief introduction to the theory of mass diffusion is given and the options that are available in ANSYS CFX to consider diffusion are presented. In a mixture consisting of two materials, say species s and component k , the mass flux (mass flow per unit area) of species s can be described as [10]:

$$j_{s,i} = -\rho \mathcal{D}_{sk} \frac{\partial Y_s}{\partial x_i} \quad (2.39)$$

In honor of Fick [26] this is called Fick's law with \mathcal{D}_{sk} as the binary diffusion coefficient and Y_s as the mass fraction of species (or component) s . Similarly for component k in this mixture one can state:

$$j_{k,i} = -\rho \mathcal{D}_{ks} \frac{\partial Y_k}{\partial x_i} \quad (2.40)$$

It is important to note, that:

$$\mathcal{D}_{sk} = \mathcal{D}_{ks} \quad (2.41)$$

The diffusion coefficient for a binary mixture of species s and k is usually given by an expression that is credited to Chapman and Enskog. Combining this expression with ideal gas law, the equation (as given in Poling et al. [75]):

$$\mathcal{D}_{sk} = \frac{0.00266 T^{3/2}}{p M_{sk}^{1/2} \sigma_{sk}^2 \Omega^{(1,1)*}} \quad (2.42)$$

gives the diffusion coefficient \mathcal{D}_{sk} in cm^2/s , where temperature T is in K, pressure p in bar and the characteristic length σ_{sk} in \AA . For equation (2.42) the reduced molar mass M_{sk} has to be given in g/mol and is calculated from the molar masses of the two species as:

$$M_{sk} = \frac{2M_s M_k}{M_s + M_k} \quad (2.43)$$

The characteristic length σ_{sk} is calculated from the Lennard-Jones collision diameters:

$$\sigma_{sk} = \frac{\sigma_s + \sigma_k}{2} \quad (2.44)$$

Collision diameter σ as well as well depth ε of the Lennard-Jones potential for various species are available from several sources e.g. from Svehla [98].

The diffusion collision integral $\Omega^{(1,1)*}$ is either tabulated or calculated from equation (2.18) with coefficients given in Table 2.2. The reduced temperature required for equation (2.18) is in this case considered as:

$$T_{red} = kT / \varepsilon_{sk} \quad (2.45)$$

with k as the Boltzmann constant. The interaction value ε_{sk} of the Lennard-Jones potential well depth is calculated from the individual values:

$$\varepsilon_{sk} = (\varepsilon_s \varepsilon_k)^{1/2} \quad (2.46)$$

For a mixture of more than two species, a mixture diffusion coefficient can be calculated from the binary diffusion coefficients. For the diffusion of a species s into a mixture the coefficient can be calculated as [51]:

$$D_s = \frac{1 - Y_s}{\sum_{k \neq s}^{N_s} X_k / \mathcal{D}_{sk}} \quad (2.47)$$

with X denoting mole fraction. Through the use of expressions in CEL (CFX Expression Language) this equation has been implemented in CFX in course of this thesis. However, this simplified approach is only an approximation and has an important disadvantage: Since the sum of all diffusion components is not zero, the difference is balanced by the constraint species. Therefore the results are affected by the choice of the constraint species.

Preuß and Spille-Kohoff [81] show results from several numerical simulations of diffusion processes in CFX. In two cases the results are independent of the choice of constraint species. In their work they implemented the additional term required for the method introduced by Ramshaw [83] and the diffusion fluxes from Stefan-Maxwell diffusion through the use of the source term in the species transport equation. Unfortunately they do not go into details for their implementation. To understand the difficulty in this task, it is important to point out how CFX handles this equation. Figure 2.2 illustrates required terms and definitions.

The differential form of the species transport equation (2.25) is rewritten in integral conservation form, with volume integrals involving gradient or divergence operators converted to surface integrals:

$$\frac{d}{dt} \int_V \rho Y_s dV + \int_O \rho u_j Y_s dn_j = \int_O \Gamma \left(\frac{\partial Y_s}{\partial x_j} \right) dn_j + \int_V S_s dV \quad (2.48)$$

Here V is representing a control volume, O the surrounding control surface and dn_j the differential Cartesian components of outward normal surface vector.

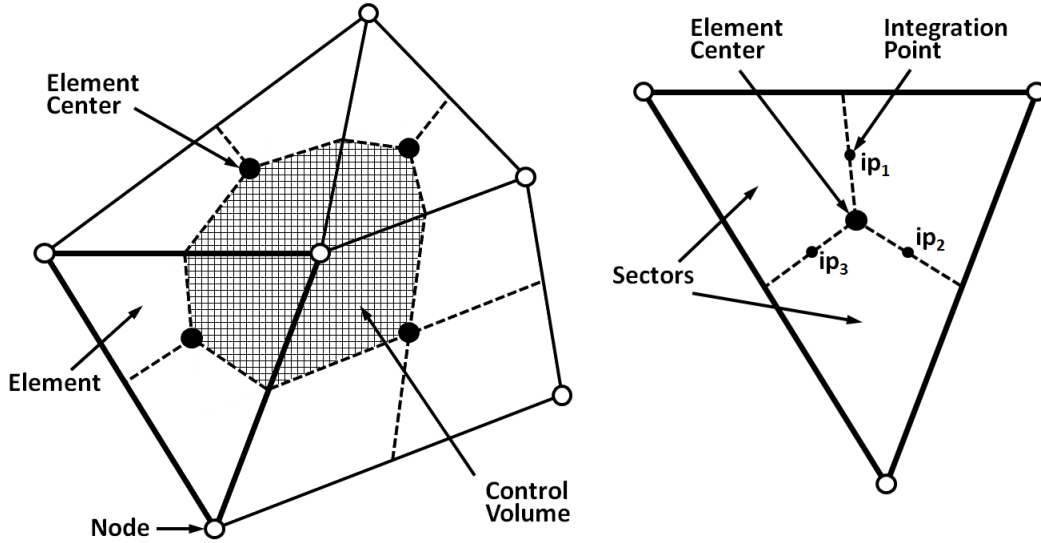


Figure 2.2: Illustration of terms and definitions in CFX (with modifications from [4])

For the first order backward Euler scheme equation (2.48) is discretized as:

$$\frac{V}{\Delta t} (\rho Y_s - \rho^o Y_s^o) + \sum_{ip} (\rho u_j \Delta n_j) Y_{s,ip} = \sum_{ip} \left(\Gamma \frac{\partial Y_s}{\partial x_j} \Delta n_j \right)_{ip} + V S_s \quad (2.49)$$

Superscript o is denoting values from the previous time step. The diffusion term is handled as a surface integral and discretized at the integration points (ip_n). This ensures species conservation since surface integrals in control volumes adjacent to integrations are equal and opposite in sign. The source term on the other hand is treated as a volume integral.

A proper implementation of multi-component diffusion thus requires treating the source term analogously as a surface integral to be locally conservative. Therefore a user routine needs to have access to the integration points. Due to the limitations the user has to intervene with the code, this task is very difficult to achieve.

Simulations of a laminar non-premixed flame, where kinematic diffusivities are set, show – dependent on the choice of the constraint species – satisfactory results (see section 4.2). For more accurate simulations it is advisable to resort to an alternative CFD package, which is able to account for multicomponent diffusion correctly. For instance in FLUENT [5] full multi-component diffusion, referred to as the Stefan-Maxwell equations [10], is implemented already.

2.6 Turbulence

In a turbulent flow variables (density, mass fractions, velocity, etc.) seem to show irregular or random fluctuations. The chaotic seeming procedures are very complex and it is difficult to simulate them numerically. Several ways exist how to deal with turbulence in CFD. One possible way is to decompose a fluctuating quantity into an averaged and a varying component according to:

$$\phi = \bar{\phi} + \phi' \quad (2.50)$$

For compressible flows the averaging is density-weighted (Favre averaging):

$$\phi = \tilde{\phi} + \phi'' \quad \text{with} \quad \tilde{\phi} = \frac{\overline{\rho\phi}}{\bar{\rho}} \quad (2.51)$$

For transient simulations the equations in CFX are actually ensemble-averaged. When the decomposition of the fluctuating flow variables is carried out in the Navier-Stokes equations (as introduced in section 2.1) the Reynolds averaged Navier Stokes (RANS) equations are obtained which are also referred to as Reynolds equations. Unfortunately these equations cannot be solved because turbulent stresses and heat-flux quantities appear which have to be regarded as new unknowns. Equations are required that relate these unknowns to the mean flow variables. This closure problem is handled through turbulence modeling.

Turbulent-viscosity models assume that Reynolds stresses can be determined by mean velocity gradients. For negligible density fluctuations this relationship can be written as:

$$-\overline{\rho u'_i u'_j} = \mu_t \left(\frac{\partial \bar{u}_i}{\partial x_j} + \frac{\partial \bar{u}_j}{\partial x_i} \right) - \frac{2}{3} \delta_{ij} \left(\mu_t \frac{\partial \bar{u}_k}{\partial x_k} + \rho k \right) \quad (2.52)$$

The turbulent viscosity (or eddy viscosity) μ_t has to be modeled. In this thesis for turbulent flow the k- ϵ turbulence model is employed, which is one of the most widely used turbulence models. In this case μ_t is expressed as:

$$\mu_t = C_\mu \rho \frac{k^2}{\epsilon} \quad (2.53)$$

One additional transport equation is solved for turbulent kinetic energy k :

$$\frac{\partial(\rho k)}{\partial t} + \frac{\partial}{\partial x_j} (\rho \bar{u}_j k) = \frac{\partial}{\partial x_j} \left[\left(\mu + \frac{\mu_t}{\sigma_k} \right) \frac{\partial k}{\partial x_j} \right] + \mathcal{P} - \rho \epsilon \quad (2.54)$$

The second additional equation is solved for turbulent eddy dissipation ε :

$$\frac{\partial(\rho\varepsilon)}{\partial t} + \frac{\partial}{\partial x_j}(\rho\bar{u}_j\varepsilon) = \frac{\partial}{\partial x_j} \left[\left(\mu + \frac{\mu_t}{\sigma_\varepsilon} \right) \frac{\partial \varepsilon}{\partial x_j} \right] + \frac{\varepsilon}{k} (C_{\varepsilon 1} \mathcal{P} - C_{\varepsilon 2} \rho \varepsilon) \quad (2.55)$$

The standard values of the five model constants are:

$$C_\mu = 0.09, C_{\varepsilon 1} = 1.44, C_{\varepsilon 2} = 1.92, \sigma_k = 1.0, \sigma_\varepsilon = 1.3 \quad (2.56)$$

The quantity \mathcal{P} is the turbulence production and modeled as:

$$\mathcal{P} = \mu_t \left(\frac{\partial \bar{u}_i}{\partial x_j} + \frac{\partial \bar{u}_j}{\partial x_i} \right) \frac{\partial \bar{u}_i}{\partial x_j} - \frac{2}{3} \frac{\partial \bar{u}_k}{\partial x_k} \left(3\mu_t \frac{\partial \bar{u}_k}{\partial x_k} + \rho k \right) \quad (2.57)$$

In CFX the k- ε turbulence model by default is used with the scalable wall-function, which allows using arbitrarily fine near wall grids [3]. Details on the scalable wall function can be found in the CFX solver theory guide [4].

2.7 Solver Theory in ANSYS CFX

For the simulation of combustion instabilities it is important to know how pressure, velocity and heat release are treated within the solver. Figure 2.3 shows the sets of equations that are handled within ANSYS CFX during the solution process. These are only the equations relevant to this work. A more detailed flow chart is shown in [4].

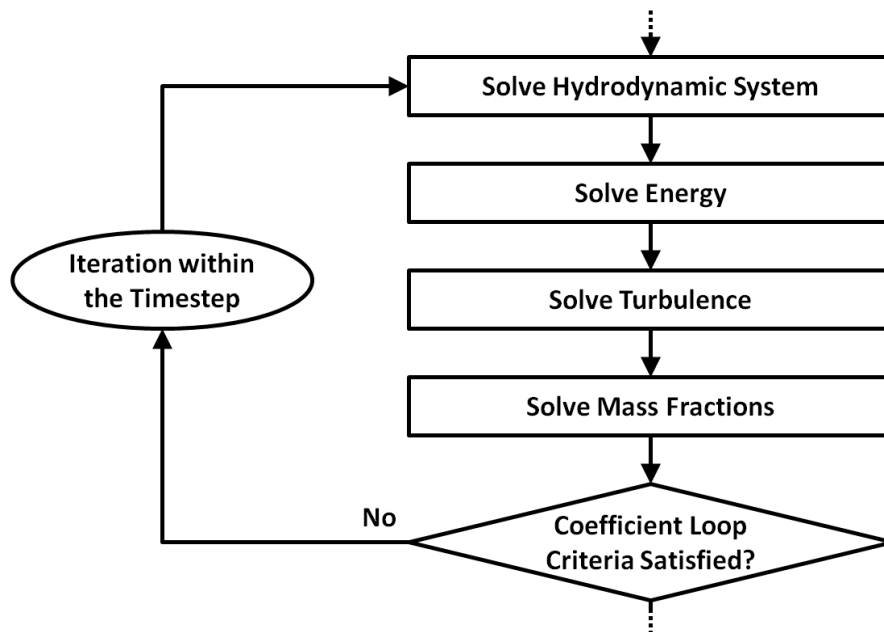


Figure 2.3: Simplified solution flow chart for inner iterations within ANSYS CFX [4]

It is important to note that there is just one box for the hydrodynamic system. This is because CFX is a coupled solver, i.e. the equations for pressure and velocity (mass and momentum) are solved together. Therefore there is no need for pressure correction algorithms such as SIMPLEC [102] or PISO [46] that are employed in segregated solvers. A problem arising from discretization is the odd-even decoupling of the pressure field (for details see e.g. Hirsch [44] or Patankar [70]). This problem can be best resolved by using staggered grids [39], i.e. different grids for pressure and velocity fields. In CFX a collocated grid is employed and the approach to avoid decoupling is a different. The strategy is similar to the approach introduced by Rhie and Chow [87] and its modification by Majumdar [62]. A detailed description of the adopted method is given in the CFX solver theory guide [4].

Important for the implementation of combustion are also the next steps in the iteration. The energy equation is solved right after the mass and momentum equations (see Figure 2.3). Therefore the influence of heat release on the hydrodynamic system becomes effective in the next inner iteration loop. The "Solve Mass Fractions" step is the last task within the inner loop of a time step. Manipulations on the species transport equations will affect the hydrodynamic system and the energy equation only in the next inner iteration loop.

CFX uses an element-based finite volume method for discretization. For the advection term it is possible to either use the first-order accurate "Upwind" scheme or to specify a factor for blending first and second order differencing or to use the "High Resolution" scheme, which is based on the boundedness principles used by Barth and Jespersen [7]. Usually by default the "High Resolution" scheme is chosen, except for turbulence equations, which use the first order upwind scheme. Available options for the transient scheme are the first and the second order backward Euler scheme. In addition it is also possible to choose the "High Resolution" option which is second order scheme but reverts to the first order scheme to maintain a bounded solution [3].

Whether a simulation in CFX is compressible or incompressible is determined by the choice of the equation of state. If a constant density is specified the simulation is incompressible. When materials with the ideal gas equation of state or the Redlich-Kwong equation of state are selected the simulation is compressible. Simulations using materials with variable density, as well as multi-component fluids composed of these materials, are able to calculate the speed of sound correctly.

2.8 Non-Reflecting Boundary Conditions in CFX

A key issue when dealing with forced or self-excited fluctuations in simulations is the correct choice of boundary conditions, as reflections on the boundaries may cause inappropriate behavior of variables. Zwart and Abshoff [108] discuss reasons for reflections and explain how they are handled in CFX. They distinguish between two types of boundary conditions: physical and numerical. Physical boundary conditions refer to dependent variables which are specified on the boundary. Numerical (or soft) boundary conditions refer to those dependent variables which are not specified on the boundary. For instance: pressure may be specified on a subsonic outlet boundary, while velocity and temperature remain unspecified and thus need to be evaluated during the solving process.

As for reflections at numerical boundary conditions it is important to know which of the two finite volume methods that are illustrated in Figure 2.4 the solver applies. In the cell-centered (or volume-filled) method the elements (or cells) are used as control volumes. Solution values from the conservation equations are stored at the element center. The cell-vertex (or element-filled) method solves the conservation equations for control volumes which are constructed around each node. This is the method that is used by ANSYS CFX. This method has the advantage that solution values are stored at the nodes and thus at the boundaries are available on their correct physical location.

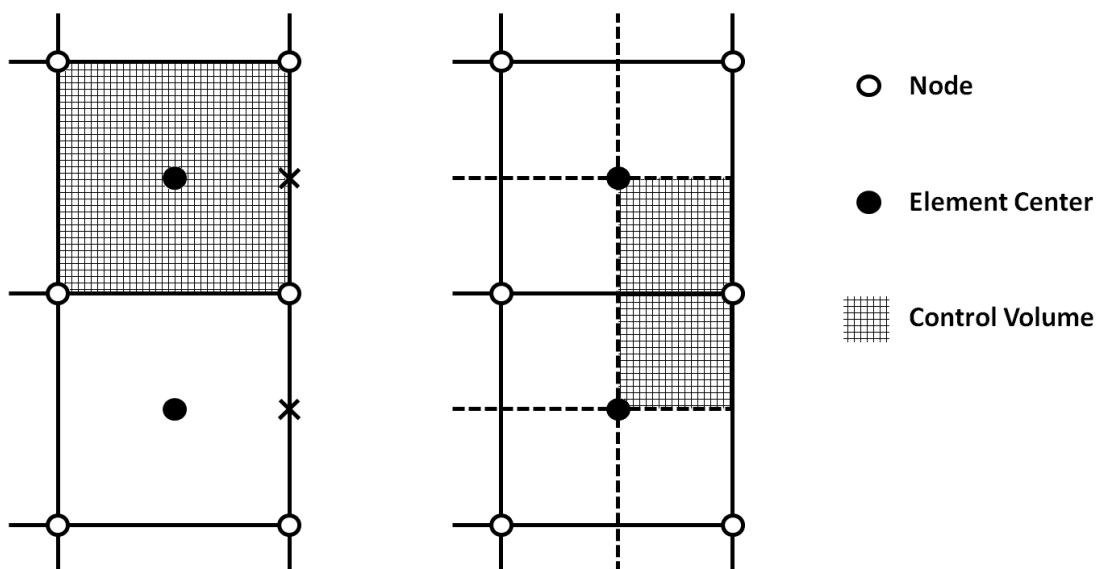


Figure 2.4: Illustration of finite volume methods: The cell-centered or volume-filled method (left) and the cell-vertex or element-filled method (right)

With the cell-centered method additional procedures are required to evaluate numerical boundary conditions. A simple extrapolation can result in an incompatibility with physical boundary conditions, so that boundary conditions become over-specified [73]. This over-specification of the boundary conditions introduces spurious waves in the domain. To avoid these numerically reflective boundary conditions a more sophisticated procedure has to be implemented, such as the methodology introduced by Poinso and Lele [73]. However, as mentioned above: ANSYS CFX does not require any additional procedures since all conservation equations are solved also on the boundary nodes. Therefore, numerical boundary conditions in ANSYS CFX are inherently non-reflective [108].

Reflections at physical boundary conditions usually can arise from specifications which are inconsistent with the physical nature of the flow. An outlet with uniform static pressure for example has to be placed in a sufficient distance downstream from the last obstacle. If in a given case this is not possible ANSYS CFX offers some alternative options for the boundary specifications which are less reflective. Advice for setting boundary conditions correctly is available from the ANSYS CFX – Solver Modeling Guide [3] and the validation report of Zwart and Abshoff [108].

In transient simulations reflections at physical boundary conditions in some cases are physically reasonable. In some simulations it might still be desirable to allow an acoustic wave to exit the domain. With a beta feature that is implemented in ANSYS CFX it is possible to have such physically non-reflective boundary conditions. The methodology is based on characteristic analysis that has been introduced by Poinso and Lele [73]. Zwart and Abshoff [108] show results from simulations of different representative test-cases to illustrate the proper implementation of this feature in ANSYS CFX. Furthermore this feature also offers a good possibility to excite the domain (see section 5.3.2).

3 Combustion

3.1 Chemical Kinetics

In this section all equations are listed that are necessary for the implementation of chemical kinetics as far as done in this work. They can also be found in similar form in either Kee et al. [53] or Turns [101], which served as the two main sources for this section.

3.1.1 System of Equations

The combustion process is defined by the change in temperature $T(t)$ and molar concentrations $c_s(t)$ over time. In a general form, the system of equations that has to be solved is therefore:

$$\begin{aligned}\frac{dT}{dt} &= f(T, c_1, \dots, c_{N_s}) \\ \frac{dc_s}{dt} &= f(T, c_1, \dots, c_{N_s})\end{aligned}\tag{3.1}$$

This is one equation for temperature and N_s equations for composition, one for each of the involved species s . Each cell of the domain that is used by the CFD solver to calculate the flow can be treated as one constant volume reactor. For ideal gases in an adiabatic system the equations can be written as [101]:

$$\begin{aligned}\frac{dT}{dt} &= \frac{R_u T \sum_s^{N_s} \dot{\omega}_s - \sum_s^{N_s} (H_s \dot{\omega}_s)}{\sum_s^{N_s} [c_s (C_{p_s} - R_u)]} \\ \frac{dc_s}{dt} &= \dot{\omega}_s\end{aligned}\tag{3.2}$$

Thermodynamic properties and chemical rate expressions that are required for equations (3.2) are specified below.

3.1.2 Thermodynamic Data

Thermodynamic properties of each reacting species are obtained from polynomials. The form of these polynomials is taken from Gordon and McBride [34]:

$$\frac{C_{p_s}^0}{R_u} = a_{1s} + a_{2s}T + a_{3s}T^2 + a_{4s}T^3 + a_{5s}T^4 \quad (3.3)$$

$$\frac{H_s^0}{R_u T} = a_{1s} + \frac{a_{2s}}{2}T + \frac{a_{3s}}{3}T^2 + \frac{a_{4s}}{4}T^3 + \frac{a_{5s}}{5}T^4 + \frac{a_{6s}}{T} \quad (3.4)$$

$$\frac{S_s^0}{R_u} = a_{1s} \ln T + a_{2s}T + \frac{a_{3s}}{2}T^2 + \frac{a_{4s}}{3}T^3 + \frac{a_{5s}}{4}T^4 + a_{7s} \quad (3.5)$$

The superscript ⁰ is corresponding to standard pressure p^0 . For perfect gases these properties are independent of pressure, therefore their values are as well the actual values. In order to improve accuracy two different polynomials are used – one for low (up to 1000 K) and one for high temperatures (above 1000 K). In this case seven coefficients are needed for each of the two temperature ranges. In this thesis the values of the coefficients for equations (3.3), (3.4) and (3.5) are taken from the CFX materials database. They are listed in Table A.2 for the low and Table A.3 for the high temperature range.

3.1.3 Chemical Rate Expressions

The chemical production rate $\dot{\omega}_s$ of the s th species is given by:

$$\dot{\omega}_s = \sum_{r=1}^{N_r} \nu_{sr} q_r \quad (s = 1, \dots, N_s) \quad (3.6)$$

where ν_{sr} is the difference of product and reactant stoichiometric coefficient:

$$\nu_{sr} = \nu''_{sr} - \nu'_{sr} \quad (3.7)$$

and q_r is the rate-of-progress variable for the r th reaction. Its value can be calculated from:

$$q_r = k_{fr} \prod_{s=1}^{N_s} c_s^{\nu'_{sr}} - k_{br} \prod_{s=1}^{N_s} c_s^{\nu''_{sr}} \quad (3.8)$$

where k_{fr} and k_{br} are the forward and backward rate constants of the r th reaction. The molar concentration c_s of each species s is obtained from:

$$c_s = \frac{\rho Y_s}{M_s} \quad (3.9)$$

with Y_s denoting its mass fraction, M_s its molar mass and ρ density. The forward rate constants of the N_r reactions strongly depend on temperature. This temperature dependence is specified by (modified) Arrhenius law:

$$k_{fr} = A_r T^{\beta_r} \exp\left(\frac{-E_r}{R_u T}\right) \quad (3.10)$$

The pre-exponential factor A_r , the temperature exponent β_r and the activation energy E_r are specified (see Table A.4 and Table A.6) for each reaction. The backward rate constants k_{br} can then be obtained from the forward rate constants by using equilibrium constants:

$$k_{br} = \frac{k_{fr}}{K_{cr}} \quad (3.11)$$

The equilibrium constants based on molar concentrations K_{cr} can be determined from the equilibrium constants based on partial pressure K_{pr} . The two constants are related by:

$$K_{cr} = K_{pr} \left(\frac{p_{atm}}{R_u T}\right)^{\sum_{s=1}^{N_s} \nu_{sr}} \quad (3.12)$$

The equilibrium constants K_{pr} are obtained with the relationship:

$$K_{pr} = \exp\left(\frac{\Delta S_r^0}{R_u} - \frac{\Delta H_r^0}{R_u T}\right) \quad (3.13)$$

The Δ in this case expresses the change that occurs when a reaction is complete, i.e. all reactants have turned into products. Following equations apply:

$$\frac{\Delta S_r^0}{R_u} = \sum_{s=1}^{N_s} \nu_{sr} \frac{S_s^0}{R_u} \quad (3.14)$$

$$\frac{\Delta H_r^0}{R_u T} = \sum_{s=1}^{N_s} \nu_{sr} \frac{H_s^0}{R_u T} \quad (3.15)$$

3.1.4 Third Body Reactions

In some reactions a “third body” appears that does not participate in the reaction but is required as a collision partner. In a dissociation reaction this third body adds the energy that is needed in order to break the bond of a molecule. In a recombination reaction its kinetic energy increases when the liberated energy from

the newly formed molecule is transferred. The expression for the rate-of-progress variable for these reactions is:

$$q_r = \left(\sum_{s=1}^{N_s} \alpha_{sr} c_s \right) \left(k_{fr} \prod_{s=1}^{N_s} c_s^{v'_{sr}} - k_{br} \prod_{s=1}^{N_s} c_s^{v''_{sr}} \right) \quad (3.16)$$

When compared to equation (3.8) an additional factor appears here:

$$c_{N_s+1} = \sum_{s=1}^{N_s} \alpha_{sr} c_s \quad (3.17)$$

In this factor the concentration of all involved species are included along with their respective efficiencies as third bodies α_{sr} . This factor can be regarded as the concentration of the third body, so that equation (3.16) can be written as:

$$q_r = k_{fr} \prod_{s=1}^{N_s+1} c_s^{v'_{sr}} - k_{br} \prod_{s=1}^{N_s+1} c_s^{v''_{sr}} \quad (3.18)$$

If $\alpha_{sr} = 1$ for all species, the first factor in equation (3.16) is the total concentration of the mixture. Third body efficiencies that differ from 1 are specified along with the reaction mechanism (see Table A.5 and Table A.8).

3.1.5 Pressure-Dependent Rate Constant

The chemical rate constant of certain dissociation and recombination reactions does not only depend on temperature but apparently also on pressure. This pressure-dependency can be explained by the fact that the reaction at hand is not elementary, but rather a sequence of reactions [103]. To handle this pressure-dependency, the forward rate coefficients of a reaction are given for the low- (k_0) and the high-pressure limit (k_∞). In order to facilitate reading, subscripts r and f are omitted:

$$k_0 = A_0 T^{\beta_0} \exp\left(\frac{-E_0}{R_u T}\right) \quad (3.19)$$

$$k_\infty = A_\infty T^{\beta_\infty} \exp\left(\frac{-E_\infty}{R_u T}\right) \quad (3.20)$$

A reduced pressure can be calculated by:

$$p_{red} = \frac{k_0}{k_\infty} \left(\sum_{s=1}^{N_s} \alpha_s c_s \right) \quad (3.21)$$

with which the rate constant can be defined to be:

$$k = k_{\infty} \left(\frac{p_{red}}{1 + p_{red}} \right) F \quad (3.22)$$

In the simplest case $F = 1$, which is the approach suggested by Lindemann [58]. In reactions (9) and (15) of the Ó Conaire mechanism [69] (see Table A.6) the concept of Troe (see [32] and [100]) is followed. F has to be calculated in a more complicated way from:

$$\log F = \left[1 + \left[\frac{\log p_{red} + c}{N - d(\log p_{red} + c)} \right]^2 \right]^{-1} \log F_{cent} \quad (3.23)$$

with the constants¹ given by:

$$c = -0.4 - 0.67 \log F_{cent} \quad (3.24)$$

$$N = 0.75 - 1.27 \log F_{cent} \quad (3.25)$$

$$d = 0.14 \quad (3.26)$$

$$F_{cent} = (1 - a) \exp\left(-\frac{T}{T^{***}}\right) + a \exp\left(-\frac{T}{T^*}\right) + \exp\left(-\frac{T^{**}}{T}\right) \quad (3.27)$$

The parameters a , T^{***} , T^* and T^{**} are specified along with the reaction mechanism (see Table A.7). In cases where T^{**} is not given, the last summand of equation (3.27) has to be omitted. Having determined the forward rate coefficient from equation (3.22), the backward rate constant and the rate-of-progress variable can be calculated by using the equations given in 3.1.3.

3.1.6 Intermediate Complex-Forming Bimolecular Reactions

There are certain reactions that show anomalous temperature dependence – with rate constant minima [43] or a sharp up-turn [42] of the rate constant at moderate and high temperatures. The explanation for this occurrence is that an intermediate complex formation is involved in the reaction [42]. In order to handle this behavior, the rate constant is calculated as the sum of two (or more) rate expressions (see reactions 14 and 19 in Table A.5).

¹ Definitions for constants are taken from [32]. They are incorrectly quoted in [52] and [103].

3.1.7 Stiff System of ODEs

When in a system of ordinary differential equations (ODEs) the scales of the independent variable are very diverse, stiffness occurs. In combustion processes, the reaction rates (time scales) of elementary reactions usually differ considerably. The system that describes the combustion process in equations (3.1) can be written as:

$$\mathbf{y}' = \mathbf{f}(\mathbf{y}) \quad (3.28)$$

For the adiabatic constant volume reactor the components of:

$$\mathbf{f}(\mathbf{y}) = \left[\begin{array}{cccc} \frac{dT}{dt} & \frac{dc_1}{dt} & \frac{dc_2}{dt} & \dots & \frac{dc_{N_s}}{dt} \end{array} \right] \quad (3.29)$$

are described by equations (3.2). The vector \mathbf{y} contains the dependent variables:

$$\mathbf{y} = \left[T \quad c_1 \quad c_2 \quad \dots \quad c_{N_s} \right] \quad (3.30)$$

Equation (3.28) is a stiff system of ODEs. Implicit differencing methods prevent the numerical solution of the system to become unstable [103]. Implicit differencing of equation (3.28) gives:

$$\mathbf{y}_{n+1} = \mathbf{y}_n + \Delta t_n \mathbf{f}(\mathbf{y}_{n+1}) \quad (3.31)$$

A glance at equations (3.2) reveals that this is a set of non-linear equations. Therefore they are linearized as:

$$\mathbf{y}_{n+1} = \mathbf{y}_n + \Delta t_n \left[\mathbf{f}(\mathbf{y}_{n+1}) + \mathbf{f}' \cdot (\mathbf{y}_{n+1} - \mathbf{y}_n) \right] \quad (3.32)$$

Herein \mathbf{f}' represents the Jacobian matrix:

$$\mathbf{f}' = \left[\begin{array}{cccc} \frac{d\left(\frac{dT}{dt}\right)}{dT} & \frac{d\left(\frac{dT}{dt}\right)}{dc_1} & \frac{d\left(\frac{dT}{dt}\right)}{dc_2} & \dots & \frac{d\left(\frac{dT}{dt}\right)}{dc_{N_s}} \\ \frac{d\left(\frac{dc_1}{dt}\right)}{dT} & \frac{d\left(\frac{dc_1}{dt}\right)}{dc_1} & \frac{d\left(\frac{dc_1}{dt}\right)}{dc_2} & \dots & \frac{d\left(\frac{dc_1}{dt}\right)}{dc_{N_s}} \\ \frac{d\left(\frac{dc_2}{dt}\right)}{dT} & \frac{d\left(\frac{dc_2}{dt}\right)}{dc_1} & \frac{d\left(\frac{dc_2}{dt}\right)}{dc_2} & \dots & \frac{d\left(\frac{dc_2}{dt}\right)}{dc_{N_s}} \\ \vdots & \vdots & \vdots & \ddots & \vdots \\ \frac{d\left(\frac{dc_{N_s}}{dt}\right)}{dT} & \frac{d\left(\frac{dc_{N_s}}{dt}\right)}{dc_1} & \frac{d\left(\frac{dc_{N_s}}{dt}\right)}{dc_2} & \dots & \frac{d\left(\frac{dc_{N_s}}{dt}\right)}{dc_{N_s}} \end{array} \right] \quad (3.33)$$

This is evaluated at the old values \mathbf{y}_n . Rearranging of equation (3.32) gives:

$$\mathbf{y}_{n+1} = \mathbf{y}_n + \Delta t_n [\mathbf{1} - \Delta t_n \mathbf{f}']^{-1} \cdot \mathbf{f}(\mathbf{y}_n) \quad (3.34)$$

and shows that the main task for finding \mathbf{y}_{n+1} is matrix inversion. Through linearization the implicit differencing scheme has become semi-implicit. It is not guaranteed to be stable but gives a better stability than explicit methods [80]. The time step size Δt_n has to be small enough so that the linear approximation is justified. Therefore it is indispensable to apply an algorithm with step size adjustment.

There are different groups of higher-order methods to implicitly solve a stiff system of ODEs. One of these groups is the Rosenbrock methods which are also known as Kaps-Rentrop methods and which represent the most useful generalization of the Runge-Kutta method [80]. For a system of up to about ten independent variables these methods are similarly effective as more complicated algorithms [80] and are therefore appropriate for the 8 species in H₂-O₂-combustion or the 9 species in H₂-Air-combustion.

A general purpose implementation of a Kaps-Rentrop scheme in C is available from Press et al. [80]. This implementation has an embedded step size adjustment algorithm. The initial step size Δt_0 has to be delivered by the calling routine; the size for the next step is then calculated (either increased or decreased within certain limits) upon the error that was determined. When the tabulation method described in section 3.3.1 is not applied, the relevant step size can be saved as an initial step size for the next time the same cell in the domain needs to be calculated.

Together with the parameters that control the integration additional routines need to be provided that supply the required data. The CFD time step size Δt and the starting values of dependant variables \mathbf{y}_0 are available from CFX. One subroutine gives $\mathbf{f}(\mathbf{y})$, the derivative of temperature and concentrations with respect to time by calculating equations (3.2). The Jacobian matrix is computed in another subroutine. Differentiation is carried out by numerical differencing [12], where a five-point midpoint formula is used for differentiation with respect to temperature T and a three-point endpoint formula for differentiation with respect to molar concentrations c_s . For turbulent flow, of course the averaged values of variables are used as given in section 3.2.

3.1.8 Choice of Reaction Mechanism

A large number of authors have proposed mechanisms describing the detailed chemical kinetics of hydrogen oxidation. All of these mechanisms are validated and suitable for a certain range of temperature and pressure. An overview of available mechanisms and underlying shock tube data is given e.g. by Schultz and Shepherd [93].

The external routine that is used in this work for calculating combustion was originally intended to be used for modeling of supersonic combustion. Therefore a hydrogen-air reaction mechanism was implemented that was designed to be applied for scramjet combustion. Jachimowski [47] compared the kinetic behavior predicted by the reaction mechanism he assembled with shock-tube data in the range from 0.5 to 2.0 atm. His mechanism was slightly altered by Wilson and MacCormack [105]. Most of the reactions remained unchanged, but the reaction rates were refined to improve agreement with experiments in the range over 17 atm and 2300 K. When NO-formation is neglected this reaction scheme (Table A.4) consists of 19 elementary reactions and 8 species: H₂, O₂, H₂O, H, O, OH, HO₂ and H₂O₂; if N₂ is also present in a simulation it is only considered as a third body. This mechanism is perfectly tailored for combustion in scramjets, but is not validated for pressures (60 bar and more) that might appear in rocket engines.

Two more recent detailed kinetic mechanisms for H₂/O₂ mixtures were suggested by Li et al. [56] and by Ó Conaire et al. [69]. They are both based on the mechanism by Mueller et al. [66] and aiming to be used for a wide range of applications. Experiments used for comparison cover a wide range of conditions (Li et al.: 298-3000 K, 0.3-87 atm, $\phi = 0.25-5.0$; Ó Conaire et al.: 298-2700 K, 0.05-87 atm, $\phi = 0.2-6.0$). Both mechanisms seeming to be equally suitable, the one of Ó Conaire et al. (Table A.6) was chosen in this work to be used for comparison with the altered Jachimowski mechanism described above. It also contains 19 reactions and the same 8 species (further species that might be present in a simulation are only considered as third bodies). Two reactions (9 and 15) in this mechanism have pressure-dependent rate constants. For two other reactions (14 and 19) the rate constants have to be calculated as the sum of two rate expressions.

3.2 Turbulence-Chemistry Interaction

In section 3.1 each cell of the domain has been treated as one constant volume reactor. This treatment is only valid when the properties of the reacting mixture are homogeneous in the whole cell. In a turbulent flow, however, these properties fluctuate in time and space (see section 2.6). The system of equations that needs to be solved for combustion remains the same as given in equations (3.1) and (3.2) except that now averaged values are used for calculation.

A way to account for the influence of turbulence on chemistry is to use Probability Density Functions (PDF). The following brief description goes along with the explanation of Gerlinger et al. [31]. With P as the joint PDF of temperature and composition, the mean rate-of-progress variable can be determined from:

$$\bar{q}_r = \int q_r(\hat{T}, \hat{c}_1, \dots, \hat{c}_{N_s}) P(\hat{T}, \hat{c}_1, \dots, \hat{c}_{N_s}) d\hat{T} d\hat{c}_1 \dots d\hat{c}_{N_s} \quad (3.35)$$

where \hat{T} and \hat{c}_s represent sample space variables and q_r is the rate-of-progress variable from equation (3.18). When statistical independence of temperature and composition is assumed, the PDF can be written as:

$$P(\hat{T}, \hat{c}_1, \dots, \hat{c}_{N_s}) = P_T(\hat{T}) P_Y(\hat{Y}_1, \dots, \hat{Y}_{N_s}) \delta(\hat{\rho} - \bar{\rho}) \quad (3.36)$$

This simplifies the integration of equation (3.35) which now can be done in consecutive steps:

$$\bar{q}_r = \overline{k_{fr} \prod_{s=1}^{N_s+1} c_s^{v'_{sr}}} - \overline{k_{br} \prod_{s=1}^{N_s+1} c_s^{v''_{sr}}} \quad (3.37)$$

3.2.1 Assumed PDF of Temperature

The PDF of temperature used in this work is assumed to be a Gaussian (normal) distribution:

$$P_T(\hat{T}) = \frac{1}{\sqrt{2\pi\sigma_T^2}} \exp\left[-\frac{(\hat{T} - \tilde{T})^2}{2\sigma_T^2}\right] \quad (3.38)$$

where:

$$\sigma_T^2 = T^{n2} \quad (3.39)$$

is the variance² of temperature for which an additional transport equation is solved (see section 3.2.4). For each forward and each backward reaction the time averaged reaction constants are calculated from:

$$\bar{k}_r = \int_{\hat{T}} k_r(\hat{T}) P_T(\hat{T}) d\hat{T} \quad (3.40)$$

The normal distribution is defined from $-\infty$ to $+\infty$, which is outside of any physical temperatures and cannot be integrated numerically. Therefore limits are introduced which correspond to the relevant temperature range. The resulting clipped normal distribution is:

$$P_T(\hat{T}) = \frac{1}{\sqrt{2\pi\sigma_0^2}} \exp\left[-\frac{(\hat{T}-T_0)^2}{2\sigma_0^2}\right] \left[H(\hat{T}-T_{\min}) - H(\hat{T}-T_{\max}) \right] + A_1 \delta(\hat{T}-T_{\min}) + A_2 \delta(\hat{T}-T_{\max}) \quad (3.41)$$

Clipping is carried out by the introduction of a Heaviside function. The clipped parts of the distribution are added through Dirac delta functions at the place where clipping takes place [59], with A_1 and A_2 representing the areas of the clipped parts. The parameters of the clipped distribution T_0 and σ_0 are different from given moments \tilde{T} and σ_T . With equations:

$$f_1 = \int_{\hat{T}} \hat{T} P_T(\hat{T}; \tilde{T}, \sigma_T) d\hat{T} - \tilde{T} = 0 \quad (3.42)$$

$$f_2 = \int_{\hat{T}} (\hat{T} - \tilde{T})^2 P_T(\hat{T}; \tilde{T}, \sigma_T) d\hat{T} - \sigma_T^2 = 0 \quad (3.43)$$

these two parameters can be found using a Newton algorithm, where the i^{th} iteration provides the $(i+1)^{\text{th}}$ approximate solution [19]:

$$\begin{bmatrix} T_0 \\ \sigma_0^2 \end{bmatrix}^{(i+1)} = \begin{bmatrix} T_0 \\ \sigma_0^2 \end{bmatrix}^{(i)} - \begin{bmatrix} \frac{\partial f_1^{(i)}}{\partial T_0} & \frac{\partial f_1^{(i)}}{\partial \sigma_0^2} \\ \frac{\partial f_2^{(i)}}{\partial T_0} & \frac{\partial f_2^{(i)}}{\partial \sigma_0^2} \end{bmatrix}^{-1} \begin{bmatrix} f_1 \\ f_2 \end{bmatrix}^{(i)} \quad (3.44)$$

Clipping can only be successfully performed when the mean temperature is well within the specified range, otherwise the Newton method will fail. As soon as the parameters T_0 and σ_0 are known, numerical integration is used to calculate

² In this thesis σ denotes standard deviation. This is also the case in Girimaji [33] and Lockwood and Naguib [59], but is in contrast to Gerlinger (e.g. in [30]), Di Domenico [19] and Förster [28], who use the letter σ to denote variance.

the averaged reaction constants according to equation (3.40). Simpson's method on the one hand and Romberg's method on the other (both taken from Press et al. [80]) have been implemented for this purpose. While both algorithms show similar performance, it is Simpson's rule that has been used for all simulations. The required computational effort for using equation (3.40) is considerably higher than that necessary for calculating the rate constants with Arrhenius law only.

3.2.2 Assumed PDF of Composition

The PDF of composition used in this work is the multivariate β -distribution that has been suggested by Girimaji [33]:

$$P_Y(\hat{Y}_1, \dots, \hat{Y}_{N_s}) = \frac{\Gamma\left(\sum_{s=1}^{N_s} \beta_s\right)}{\prod_{s=1}^{N_s} \Gamma(\beta_s)} \prod_{s=1}^{N_s} \hat{Y}_s^{\beta_s-1} \delta\left(1 - \sum_{s=1}^{N_s} \hat{Y}_s\right) \quad (3.45)$$

where the Dirac delta function is required for normalization. The parameters β_s are specified as:

$$\beta_s = \tilde{Y}_s \underbrace{\left[\frac{\sum_{k=1}^{N_s} \tilde{Y}_k (1 - \tilde{Y}_k)}{\sigma_Y^2} - 1 \right]}_B \quad (3.46)$$

The sum of species mass fraction variances is:

$$\sigma_Y^2 = \sum_{s=1}^{N_s} Y_s'^2 \quad (3.47)$$

Only one additional transport equation has to be solved for σ_Y^2 (see section 3.2.4). The advantage of equation (3.45) is that integration can be performed analytically. The respective term in equation (3.37) can then be expressed as:

$$\overline{\prod_{i=1}^{N_s+1} c_s^{v_{sr}}} = \bar{\rho}^{m_r} \prod_{s=1}^{N_s} \left(\frac{1}{M_s}\right)^{v_{sr}} \frac{\prod_{s=1}^{N_s} \prod_{j=1}^{v_{sr}} (\beta_s + v_{sr} - j)}{\prod_{j=1}^{m_r} (B + m_r - j)} \underbrace{\sum_{s=1}^{N_s} \frac{\alpha_{sr}}{M_s} (v_{sr} + \beta_s)}_{\text{only for third body reactions } \neq 1} \quad (3.48)$$

with:

$$m_{fr} = \sum_{s=1}^{N_s+1} v'_{sr} \quad \text{and} \quad m_{fr} = \sum_{s=1}^{N_s+1} v'_{sr} \quad (3.49)$$

Since the transport equation (equation (3.59) in section 3.2.4) is to loosely coupled with the species mass fractions, it is important to make sure that:

$$0 \leq \sigma_Y^2 \leq \sum_s^{N_s} \tilde{Y}_s (1 - \tilde{Y}_s) \quad (3.50)$$

when equation (3.48) is calculated. Even though equation (3.48) looks quite complicated, the numerical effort for its calculation is only slightly larger than that for the corresponding term in equation (3.18).

3.2.3 Mean Chemical Production Rates

Without turbulence-chemistry interaction the chemical production rates are calculated according to equation (3.6). With the equations in sections 3.2.1 and 3.2.2 the mean chemical production rates can now be calculated as [31]:

$$\bar{\dot{\omega}}_s = \sum_{r=1}^{N_r} \nu_{sr} \bar{q}_r = \sum_{r=1}^{N_r} \nu_{sr} (\mathcal{T}_{1f} \mathcal{T}_{2f} \mathcal{T}_{3f} \mathcal{T}_{4f} - \mathcal{T}_{1b} \mathcal{T}_{2b} \mathcal{T}_{3b} \mathcal{T}_{4b})_r \quad (3.51)$$

where the set of terms \mathcal{T}_1 to \mathcal{T}_4 for each forward and backward reaction is available as:

$$\mathcal{T}_{1r} = \bar{k}_r \quad (3.52)$$

$$\mathcal{T}_{2r} = \bar{\rho}^{m_r} \prod_{s=1}^{N_s} \left(\frac{1}{M_s} \right)^{\nu_{sr}} \quad (3.53)$$

$$\mathcal{T}_{3r} = \frac{\prod_{s=1}^{N_s} \prod_{n=1}^{\nu_{sr}} (\beta_s + \nu_{sr} - n)}{\prod_{n=1}^{m_r} (B + m_r - n)} \quad (3.54)$$

$$\mathcal{T}_{4r} = \sum_{s=1}^{N_s} \frac{\alpha_{sr}}{M_s} (\nu_{sr} + \beta_s) = \mathcal{S}_{4r} + B \sum_{s=1}^{N_s} \frac{\alpha_{sr} Y_s}{M_s} \quad (3.55)$$

The first summand of equation (3.55):

$$\mathcal{S}_{4r} = \sum_{s=1}^{N_s} \frac{\alpha_{sr} \nu_{sr}}{M_s} \quad (3.56)$$

together with the terms in equation (3.49) only need to be calculated at the beginning of the calculation as they only depend on the applied reaction mechanism.

3.2.4 Additional Equations in the Flow Solver

Several possibilities exist on how to obtain σ_T and σ_Y . In this thesis two additional transport equations have been included in the solver: one for variance of temperature and one for variance of composition. They are both chosen to be specific (solved on a per-unit-mass basis) scalars without any units. In order to model the two additional variables, for each of them the corresponding check box in the domain settings is ticked and the transport equation option selected. By selecting the kinematic diffusivity check box and setting the kinematic diffusivity to zero, the turbulent diffusion term is included only.

The equation for the transport of temperature variance is derived from the equation for thermal enthalpy [30] and has the form:

$$\frac{\partial}{\partial t}(\bar{\rho}\sigma_T^2) + \frac{\partial}{\partial x_j}(\bar{\rho}\tilde{u}_j\sigma_T^2) - \frac{\partial}{\partial x_j} \left[\left(\frac{\mu}{\text{Pr}} + \frac{\mu_t}{\text{Pr}_t} \right) \frac{\partial \sigma_T^2}{\partial x_j} \right] = 2 \frac{\mu_t}{\text{Pr}_t} \left(\frac{\partial \tilde{T}}{\partial x_j} \right)^2 - C_T \bar{\rho} \frac{\sigma_T^2}{\tau_t} \quad (3.57)$$

The first source term on the right represents production caused by temperature gradients. The second term accounts for dissipation caused by molecular diffusion where for the modeling constant usually $C_T = 2.0$ is applied. The turbulent timescale τ_t can be obtained from the turbulence model:

$$\tau_t = \frac{k}{\varepsilon} \quad (3.58)$$

A source term for the influence of compressibility is not included, as there is no adequate model available. It would be possible to include a source term that accounts for interaction of temperature fluctuations with chemical reactions. However, experience showed [29] that this term produces significant errors, when statistical independence of temperature and species fluctuations is assumed. Therefore this term is not considered either.

The other additional equation is for the transport of species variance:

$$\frac{\partial}{\partial t}(\bar{\rho}\sigma_Y^2) + \frac{\partial}{\partial x_j}(\bar{\rho}\tilde{u}_j\sigma_Y^2) - \frac{\partial}{\partial x_j} \left[\left(\frac{\mu}{\text{Pr}} + \frac{\mu_t}{\text{Pr}_t} \right) \frac{\partial \sigma_Y^2}{\partial x_j} \right] = 2 \bar{\rho} \frac{\mu_t}{\text{Pr}_t} \sum_{s=1}^{N_s} \left(\frac{\partial \tilde{Y}_s}{\partial x_j} \right)^2 - C_Y \bar{\rho} \frac{\sigma_Y^2}{\tau_t} \quad (3.59)$$

This equation is quite similar to equation (3.57). The first source term on the right hand side describes production through mass fraction gradients, while the second source term describes dissipation. The value of the constant is usually taken to be $C_Y = 2.0$. The turbulent timescale τ_t is the same as above. There is no source term representing production or dissipation caused by the interaction

of species fluctuations and chemical reactions, as it produces erroneous results [29]. Equations (3.57) and (3.59) act on the assumption that $Pr = Sc$ and $Pr_i = Sc_i$. In the present work the default values $Pr = 1.0$ and $Pr_i = 0.9$ were chosen. Detailed explanations of these transport equations as well as their variations and the assumptions for the underlying models are given by Gerlinger [30] along with available alternatives.

To include the sources on the right hand side of equations (3.57) and (3.59) in CFX a subdomain has to be defined. For the simulations presented in this thesis the subdomain extends over the entire domain. Similarly to the species transport equations, the sources for equations (3.57) and (3.59) are calculated in external routines. They remain constant for one solver time step and are recalculated at the end of each time step.

3.3 Tabulation

3.3.1 Tabulation of Chemical Kinetics

Solving the stiff system of equations (3.2) for combustion is very time consuming. There are several ways to reduce these costs. For example Liang et al. [57] developed an efficient semi-implicit solver that compared to CHEMKIN [52] is able to save up to 70 % CPU time. Another way is to use sensitivity analysis [103]. Very often tabulation methods are used. In this work an in-situ tabulation method is applied (see [27] and [28]) where the temperature and the molar concentrations are tabulated in the required region of interest. The required table needs one dimension for temperature and one for each involved species. The ranges of temperature and concentrations are divided in equidistant segments: ΔT , Δc_1 , ..., Δc_{N_s} . If the entire table was to be filled, the number of necessary points in the table would be enormously high. Since only a small fraction of all combinations of temperatures and molar concentrations will appear during the combustion process, only the required combinations are tabulated.

When a certain combination of temperature and concentrations (T, c_1, \dots, c_{N_s}) needs to be calculated, a check is performed whether the required entry in the table is already available. For this purpose the values are rounded down to the closest values in the table $(T_a, c_{1,a}, \dots, c_{N_s,a})$. If this point in the table is required for the first time, it is generated as follows.

First, with the methods described in section 3.1.7, the state is determined that the adiabatic constant volume reactor (defined by equations (3.2)) reaches in terms of temperature and concentrations after Δt , which is the solver time step from CFX. The result is an array with $N_s + 1$ components and can be written as:

$$\mathbf{f}(T_a, c_{1,a}, \dots, c_{N_s,a}) = \begin{bmatrix} T_{new} & c_{1,new} & c_{2,new} & \dots & c_{N_s,new} \end{bmatrix} \quad (3.60)$$

Then the parameters (temperature or concentration) are changed to an elevated level (b), one at a time, while the other parameters are held constant at their baseline level (a). At each combination of temperature and concentrations the system is evaluated, giving $\mathbf{f}(T_b, c_{1,a}, \dots, c_{N_s,a})$, $\mathbf{f}(T_a, c_{1,b}, \dots, c_{N_s,a})$, \dots

Finally all relevant data is stored in a table and is available to be used according to the formula:

$$\begin{aligned} \mathbf{f}(T, c_1, \dots, c_{N_s}) &= \mathbf{f}(T_a, c_{1,a}, \dots, c_{N_s,a}) + \\ &+ \frac{T - T_a}{T_b - T_a} \left(\mathbf{f}(T_b, c_{1,a}, \dots, c_{N_s,a}) - \mathbf{f}(T_a, c_{1,a}, \dots, c_{N_s,a}) \right) + \\ &+ \frac{c_1 - c_{1,a}}{c_{1,b} - c_{1,a}} \left(\mathbf{f}(T_a, c_{1,b}, \dots, c_{N_s,a}) - \mathbf{f}(T_a, c_{1,a}, \dots, c_{N_s,a}) \right) + \dots + \\ &+ \frac{c_{N_s} - c_{N_s,a}}{c_{N_s,b} - c_{N_s,a}} \left(\mathbf{f}(T_a, c_{1,a}, \dots, c_{N_s,b}) - \mathbf{f}(T_a, c_{1,a}, \dots, c_{N_s,a}) \right) \end{aligned} \quad (3.61)$$

The structure of the tables used in this thesis corresponds to the hybrid approach described by Förster [28], which is a compromise between using either an array or a list for data storage. While an array has the advantage that its entries can be accessed very quickly, it has the drawback that it requires too much memory already when it is initialized. A list in contrast only requires the memory necessary for its entries. Depending on the number of entries in the list, the search can be very time consuming. With the hybrid approach [28] the first three coordinates – say $K(T)$, $K(c_1)$ and $K(c_2)$ – determine the position of a list in a three-dimensional array. For each combination of the remaining coordinates – $K(c_3), \dots, K(c_{N_s})$ – that has been requested before there is one entry in the list. Each of these entries contains all relevant data to evaluate equation (3.61).

Instead of storing data in one point in the table, an alternative would be to save the results from all parameter combinations separately. Even though the number of entries in the lists would increase, the required memory size would decrease (per entry as well as overall). Also the time for table generation would be de-

creased. However, with the increased number of entries in the lists, the time required for searching the lists would be increased as well. Also for evaluating equation (3.61) not only one but $N_s + 1$ searches would be necessary. While this alternative was not implemented nor examined in this thesis, it appears sensible to assess its saving potentials with respect to memory requirements and computational time.

With the tabulation method described above one has to keep in mind, that the factors that influence the reaction process are only evaluated one at a time. The fact that two or more factors in combination might have a much larger influence on the reactor is not taken care of. In that respect it is to be expected that using equation (3.61) to obtain data from the table instead of solving the stiff system of ODEs would predict a slower progress of the reactions. To account for this fact intervals in the table ($\Delta T, \Delta c_1, \dots, \Delta c_{N_s}$) are much smaller than those used by Lyubar [61], who used all possible combinations of baseline and elevated level for evaluation.

One further drawback of this tabulation method is the fact that the ranges of temperature and concentrations have to be known before the simulation is started. The required region depends on many aspects of the flow, such as e.g. transport processes or boundary conditions. As a matter of fact it has turned out to be advisable to run a simulation without tabulations first, in order to have an appropriate number of segments for each dimension of the table. In this respect the in situ adaptive tabulation method introduced by Pope [76] is more convenient.

3.3.2 Tabulation of Turbulence-Chemistry Interaction

When turbulence chemistry interactions are evaluated, two additional parameters need to be tabulated as well: one for temperature variance and one for species variance. This means, that the dimension of the table is increasing by two, so that more points in the table are necessary. But also calculating the points in the table becomes more time consuming, since as mentioned before (see section 3.2.1), the numerical effort increases considerably, when equation (3.40) is used to calculate the rate constants. Consequently a tabulation method to obtain the rate constants is necessary. Table generation in this case is performed as a pre-processing step before the simulation, since the dimension of the table is relatively low.

Only two dependent variables need to be considered to tabulate the rate constant [8], since $\bar{k}_r = f(\tilde{T}, \sigma_T)$. Instead of temperature variance, however, fluctuation intensity is used:

$$I_T = \frac{\sigma_T}{\tilde{T}} \quad (3.62)$$

The rate constant for each reaction is thus tabulated as $\bar{k}_r = f(\tilde{T}, I_T)$.

Using tabulated data for the calculation of the rate constant accelerates the computation significantly. The drawback is, in addition to a loss in precision, that pressure dependence (see section 3.1.5) cannot be considered.

3.4 Approach for the Simulation of Combustion in this Thesis

ANSYS CFX has been chosen to simulate the rocket engine flame. Several possibilities are already implemented in CFX that allow the simulation of combustion processes. In addition CFX also offers multiple possibilities to define further functionalities in external routines. In this work a multi-component, variable composition mixture is used in CFX. While in this mixture all species of a detailed reaction mechanism are present, CFX only solves the equations for non-reacting flow. An external routine is used to calculate combustion.

For a multi-component flow in ANSYS CFX it is assumed [3] that the components are mixed at the molecular level. That means that they have the same pressure and temperature. A single velocity field is calculated for the multi-component fluid. A drift velocity arising from diffusion is superimposed for each component. Components can be selected from the materials library that is provided by CFX-Pre [2], where the material properties for many species are defined.

When a multi-component flow with N_s involved species is simulated in CFX, the equations of the hydrodynamic system are solved first, then the equations for energy and turbulence and finally one transport equation for $N_s - 1$ species, which recalling equation (2.25) has the form:

$$\frac{\partial(\rho Y_s)}{\partial t} + \frac{\partial(\rho u_j Y_s)}{\partial x_j} = \frac{\partial}{\partial x_j} \left(\Gamma^{s_{eff}} \frac{\partial Y_s}{\partial x_j} \right) + S_s \quad (3.63)$$

For the remaining component a constraint equation is solved, making sure the sum of all mass fractions is equal to one. At the end of each solver time step an

external routine (called Junction Box Routine – JBR – in CFX) is called, which accounts for reactions. JBRs have to be written in FORTRAN, since only then it is possible to access all values of the Memory Management System (MMS) of CFX. From this FORTRAN code however, subroutines can be called to process the data. For the implementation of combustion almost only subroutines in C were used. Material properties in external routines (see appendix A.1) are taken from the materials library in CFX.

Two different options have been investigated on how to link the external routine to the solver. In the first, mass fractions and temperatures were read from the MMS. Then, in the JBR, the values were recalculated and overwritten. Accessing all required variables from a JBR is only possible by using a subroutine (GETVAR) that is usually not available to users of CFX. In the second option the JBR was used to calculate the source terms S_s of the species transport equations (3.63) from the difference between old and new concentrations. The required effort for the implementation of this second method is somewhat larger, as within the solver additional CEL (CFX Expression Language) functions are necessary to read the source term values from the MMS. The computational effort is in both cases practically the same.

However, especially for a commercial solver, where the user does not have any insight in the code, it is difficult to assess the effect of overwriting variables. As this method directly interferes with the intended use of data fields within the solver, other variables could be affected in an unintended way. Therefore overwriting variables only appears to be unproblematic when it is used for initialization. In contrast the source terms in the species transport equations are meant to be used to include the effects of chemical reactions. This is also how the built-in combustion models in CFX account for change of composition. Therefore, as a user one should be able to rely on the fact that this feature is correctly implemented and validated. In conclusion the link through the source terms seems to be better suited for the implementation of chemistry through external routines. Thus in the following this is the approach that is pursued.

For each species s the source term for the transport equation (3.63) is calculated in the external routine from the values of mass fractions before (old) and after (new) combustion:

$$S_s = \frac{\rho}{\Delta t} (Y_{s,new} - Y_{s,old}) \quad (3.64)$$

With the first order backward Euler scheme, the discrete approximation of the transient term of the species conservation equation (3.63) in CFX is:

$$\frac{\partial}{\partial t} \int_V \rho Y_s dV = \frac{V}{\Delta t} (\rho Y_s - \rho^o Y_s^o) \quad (3.65)$$

Whereas for the second order backward Euler scheme, the resulting discretization is:

$$\frac{\partial}{\partial t} \int_V \rho Y_s dV = \frac{V}{\Delta t} \left(\frac{3}{2} (\rho Y_s) - 2 (\rho Y_s)^o + \frac{1}{2} (\rho Y_s)^{oo} \right) \quad (3.66)$$

with o representing the last and oo the last but one time step. From the comparison of equation (3.64) with (3.65) and (3.66), respectively, it is plausible that the first order backward Euler scheme has to be used. For the use with the second order backward Euler method, the calculation of the source term would need to be altered. This would make the external routine more complicated. Furthermore it is known [3] that the second order backward Euler scheme is inappropriate for quantities that must remain bounded. It is therefore advisable that for the described approach the first order backward Euler scheme is selected for the species transport equations in CFX.

When solving for the species conservation equation (3.63), CFX uses the so called "conservative mass fraction". Although the range of a mass fraction is physically limited to the range 0 to 1, the species conservation equation is not bounded. The combustion source term, which is calculated in the external routine, may cause the "conservative mass fraction" of a species to exceed either of these limits. This is not the case for the hybrid variable "mass fraction" (which CFX uses as output to CFD-Post). The value of "mass fraction" is calculated from the value of the "conservative mass fraction" taking into consideration the additional premise that all mass fraction values have to be in the range 0 to 1. Therefore it is preferable to use the "mass fraction" value of each species for the calculation of source terms in the external routine.

With the described approach one has to keep in mind that flow (within CFX) and combustion (in the external routine) are calculated separately. This method is referred to as operator splitting (see e.g. [16], [28] or [106]). The source terms in the species transport equation in CFX are calculated and updated only once per time step. The larger the time step is the larger is the error that is incorporated through operator splitting.

4 Simulation of Combustion in Reacting Flows

The purpose of the simulations presented in this chapter is to illustrate the capabilities of the approach that is chosen in this thesis to account for reacting flows. CHEMKIN [52], which can be regarded as a benchmark for chemical kinetics solvers, is used to show that combustion is correctly implemented in the external routine. Results from numerical simulations are compared to experimental data available from various steady state flames. On the basis of these flames it is also shown how the choice of different options within the flow solver and within the external routine affect the results.

4.1 Constant Volume Reactor

4.1.1 Validation of the implementation in CFX

For the simulation of combustion with external routines in CFX, each cell in the domain is regarded as one constant volume reactor. To show that reaction kinetics is correctly implemented, computations are carried out with a homogeneous constant volume reactor. In CFX a small mesh with only few nodes (an isochore, sealed off cube, without any flow) is used. At $t = 0$ ms with temperature $T = 1100$ K the composition is as follows:

$$Y_{H_2} = 0.02871, Y_{O_2} = 0.22775 \text{ and } Y_{N_2} = 1 - Y_{H_2} - Y_{O_2}$$

The first order backward Euler transient scheme is used for the simulation in CFX and the total energy equation is applied. Data obtained from this simulation is compared to data from calculations with the SENKIN [60] module of the CHEMKIN [52] package. This package uses the ODE solver VODE [11], while the external routine in CFX uses an ODE solver that has been adapted from Press et al. [80]. The thermodynamic database in CHEMKIN uses the same polynomials as in equations (3.3) to (3.5), but with different coefficients than in CFX. Therefore the coefficients in CHEMKIN were changed, so that their values agree with those used within CFX and the external routine.

In Figure 4.1 the comparison of temperature over time is shown. The curves are almost identical. The good agreement suggests that the combustion process, as described in section 3.1, is implemented correctly.

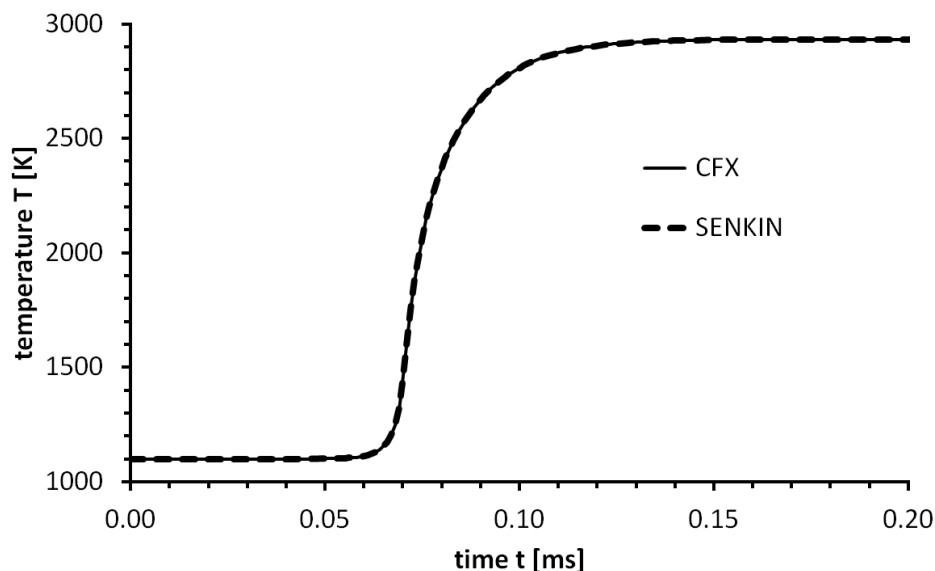


Figure 4.1: Temperature curves for a constant volume reactor from CFX and SENKIN with the mechanism from Jachimowski [47] at 1 bar

Another topic is addressed in the next figure. In ANSYS CFX there are two energy equations available: the total energy equation on the one hand and the thermal energy equation, which is suitable for liquids and low speed flows, on the other hand (see equations (2.4) and (2.6) in section 2.1). In simulations of flames as present in rocket engine flames (see sections 4.4 and 6.3) it was not possible to attain a converged solution with the total energy equation. Therefore in simulations where the Redlich-Kwong equation is applied for supercritical oxygen it has been proven to helpful to resort to the thermal energy equation.

The effect the two equations have on the simple test case described before is illustrated in Figure 4.2: The resulting temperature curves are different. When the thermal energy equation is chosen in CFX, the additional option “Include Pressure Transient Term” becomes available. Without this (in equation (2.6) the second term on the left hand side) the increase in temperature due to change in pressure is not included. The option is deactivated by default and needs to be ticked to make it available. The resulting curve is then identical with the curve obtained from the simulation with the total energy equation.

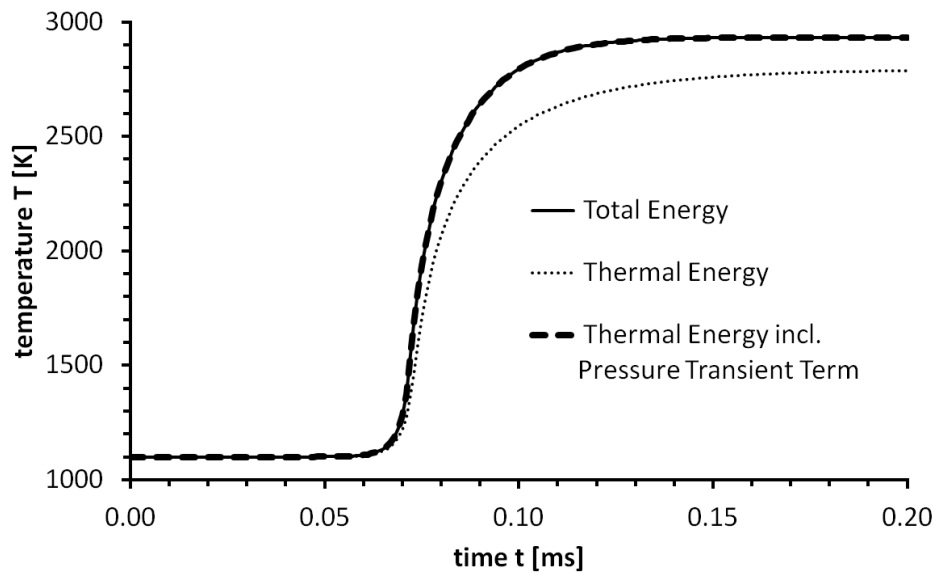


Figure 4.2: Total energy equation and thermal energy equation compared

4.1.2 Influence of the Reaction Mechanism

It is important to know that reaction mechanism might behave differently when applied to the same test case. For Figure 4.3 the same set-up as described in subsection 4.1.1 is calculated in CFX with the reaction mechanism of Ó Conaire et al. (see Table A.6) and is compared to results from the calculations with the modified Jachimowski scheme (see Table A.4) that were presented before. Both reaction mechanisms have the same temperature and the same OH mass fraction value at the final state. Only the progress is slightly different from case to case. With the reaction mechanism of Ó Conaire et al. [69] progress starts to show somewhat later, but the final state is still reached earlier.

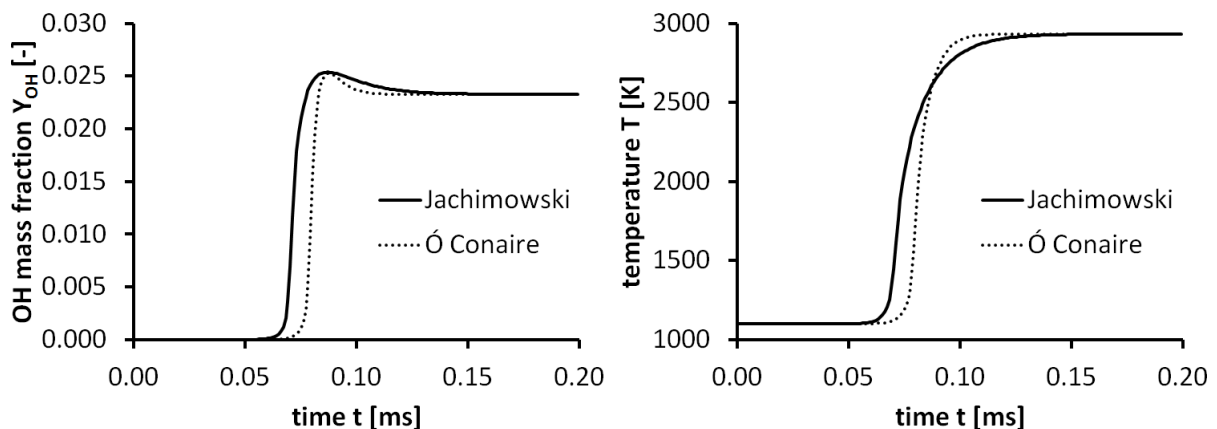


Figure 4.3: Reaction mechanisms compared based on the progress of a constant volume reactor in CFX at 1 bar

The set-up that is shown in Figure 4.4 is chosen to represent the conditions in the high pressure region. At $t = 0$ ms the simulation is initialized at $T = 1100$ K and $p = 60$ bar. In this case progress first starts to show with the mechanism of Ó Conaire et al. [69]. Once a certain state is reached progress is so fast that the curve becomes almost vertical and at final state seems to turn at right angles into a horizontal line.

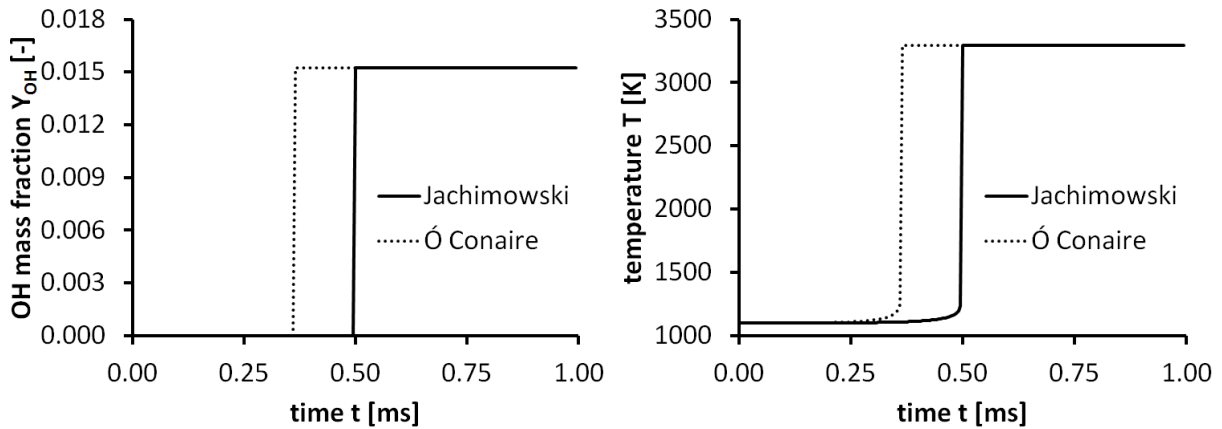


Figure 4.4: Reaction mechanisms compared based on the progress of a constant volume reactor in CFX at 60 bar

The ignition time (which in SENKIN is defined as the time when the temperature rises 400 K above the initial temperature) with the mechanism of Ó Conaire et al. is not only shorter for $p = 60$ bar. As shown in Figure 4.5 this is true for all pressures above 5 bar.

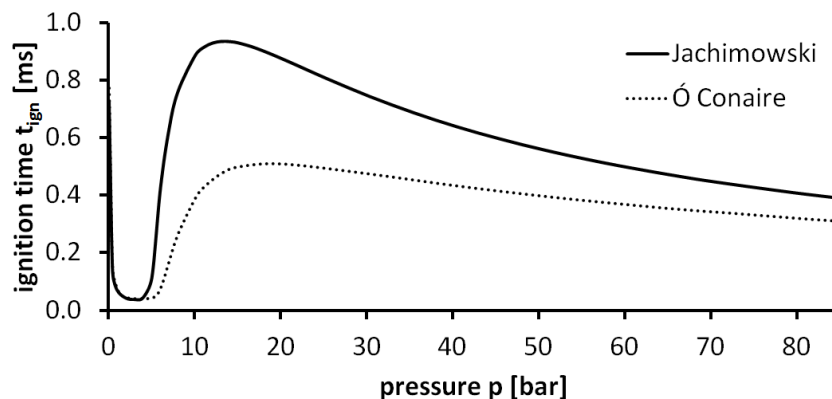


Figure 4.5: Ignition time plotted against pressure for a constant volume reactor starting at 1100 K and 60 bar

So far only stoichiometric compositions have been considered. In Figure 4.6 the two reaction mechanisms are compared based on the ignition time with various equivalence ratios. With the mechanism of Ó Conaire et al. ignition of the constant volume reactor initialized at 1100 K and 60 bar in most cases starts earlier. For very lean regimes the modified Jachimowski scheme is faster.

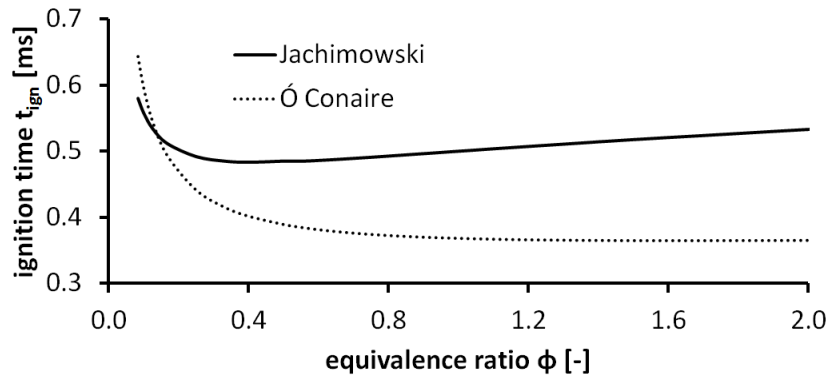


Figure 4.6: Ignition time plotted against the equivalence ratio for a constant volume reactor starting at 1100 K and 60 bar

4.2 Laminar Non-Premixed Flame

As diffusion is present in all type of flames, today it is more common to classify flames as either premixed or non-premixed. However, the expression diffusion flame is still frequently used and points out the importance of this transport phenomenon in laminar non-premixed flames. Smooke et al. [96] were probably the first ones who for the simulation of a flame considered both, detailed chemistry and fluid dynamical effects. Earlier works had to put an emphasis on either one of the two topics to keep the problem computationally feasible. With computational resources available today both problems can be handled at once. However, it is of course always important to know what effects can be neglected and which need to be modeled. While especially in laminar flames it is essential to consistently put a focus on mass diffusion (see e.g. [16]), even in a turbulent non-premixed flame the assumption of $Le=1$ can produce poor results (as shown e.g. in [19]).

In most combustion codes simplified diffusion laws like Fick's law are applied [74] to reduce the cost of numerical simulations. In CFX simplifications like $Sc=1$ or $Le=1$ can be used as discussed in section 2.4. The options for imple-

menting more complicated models for mass diffusion are rather limited in CFX (see section 2.5). In the simulations presented in this section for each species an individual mixture-averaged diffusion coefficient as introduced in equation (2.47) is used. The simulation of a laminar non-premixed flame allows assessing the effect of the implementation without the additional terms required for turbulence.

4.2.1 Experimental Data

A laminar non-premixed H_2 - O_2 flame at atmospheric pressure is studied in experiments at Lehrstuhl für Thermodynamik [24]. The laminar jet of hydrogen in the center is surrounded by the coaxial flow of oxygen. Both reactants are supplied at ambient temperature. A cylinder with an inner diameter of 62 mm is placed around the burner. The schematic view of the domain representing the geometry is shown in Figure 4.7. At the operation point examined and presented in this section the oxygen mass flow rate is 0.64 g/s, while the hydrogen mass flow rate is at 0.01 g/s.

4.2.2 Numerical Simulation

As there is no separate 2D solver in ANSYS CFX, a quasi-two-dimensional 2-degree wedge is generated in ICEM. Hexahedral elements are used throughout the domain. Experience from previous simulations in CFX (version 11.0) showed that the solver handled prisms along the axis as degenerated hexa elements and thus deteriorated the results. Therefore a small piece of the domain is removed at the edge of the wedge, so that proper hexahedral elements are employed at the axis as well. The emerging thin surface is an adiabatic wall with the “Free Slip” option. Two symmetry planes close the domain in both circumferential directions. A schematic illustration of the computational domain is given in Figure 4.7.

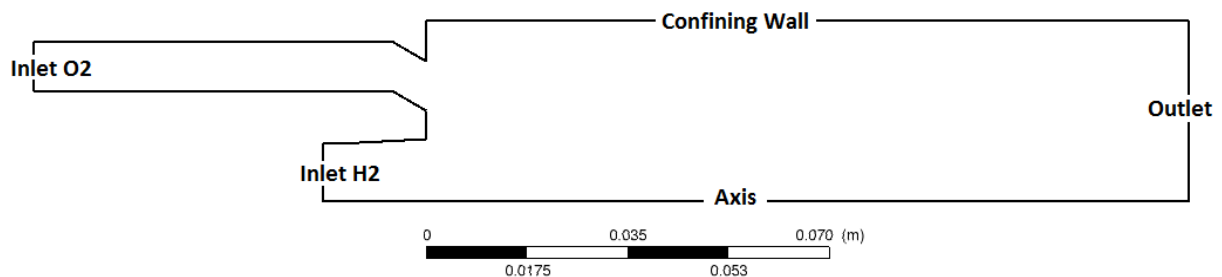


Figure 4.7: Schematic illustration of the laminar burner

The oxygen inlet ($Y_{O_2} = 1.0$) is assigned to have a constant velocity of 0.3926 m/s (calculated from mass flow rate in the experiment). The velocity profile at the hydrogen inlet ($Y_{H_2} = 1.0$) is assumed to be a fully developed channel flow (following Poiseuille's law), with a mean velocity of 0.3879 m/s (according to mass flow rate in the experiment). At both inlets temperature is assigned to be 293.15 K (20° C). The reference pressure for the entire domain is 1.013 bar. The outlet has a relative static pressure of 0 Pa. In radial direction the inner wall of the cylinder is confining the computational domain. This wall and all parts of the nozzle are assigned to be adiabatic no slip walls. Two symmetry planes close the domain in both circumferential directions. Calculations are conducted on a mesh with a spacing of about one cell/mm. The Thermal Energy Model is used to model heat transfer and no turbulence model is applied.

In a first step a cold steady state simulation was made to get the initial species distribution for H_2 and O_2 . Infinitely fast irreversible chemistry (initially derived by Burke and Schumann [13]) is applied in an external routine to ignite the flame and thus to obtain the initial solution for the simulation with detailed chemistry. The modified Jachimowski reaction mechanism given in Table A.4 is used to calculate combustion in a JBR as described in section 3.4. Kinematic diffusivities are calculated from binary diffusion coefficients in CEL expressions as described in section 2.5. The "High Resolution" advection scheme is used. The second order backward Euler transient scheme is applied, except for mass fraction equations which are first order. The time step size is 2×10^{-5} s.

4.2.3 Results

First the component O_2 of the multi-component fluid is selected as constraint, as it is present almost everywhere in the domain. The OH mass fraction plot from this simulation (see Figure 4.8) shows substantial similarity to the Abel transformed OH* image from the experiment (see Figure 4.9). Based on the assumption that the distribution of the excited hydroxyl radical OH* approximately agrees with the OH distribution (as can be seen in [25]) it is reasonable to conclude, that the implementation of diffusion is satisfactory.

However one has to bear in mind that using mixture diffusion coefficients does not guarantee species conservation. While the mass fraction plots look correct when O_2 is chosen as constraint species, this is not necessarily the case for all other species. The constraint species is largely affected and so are the results in general.

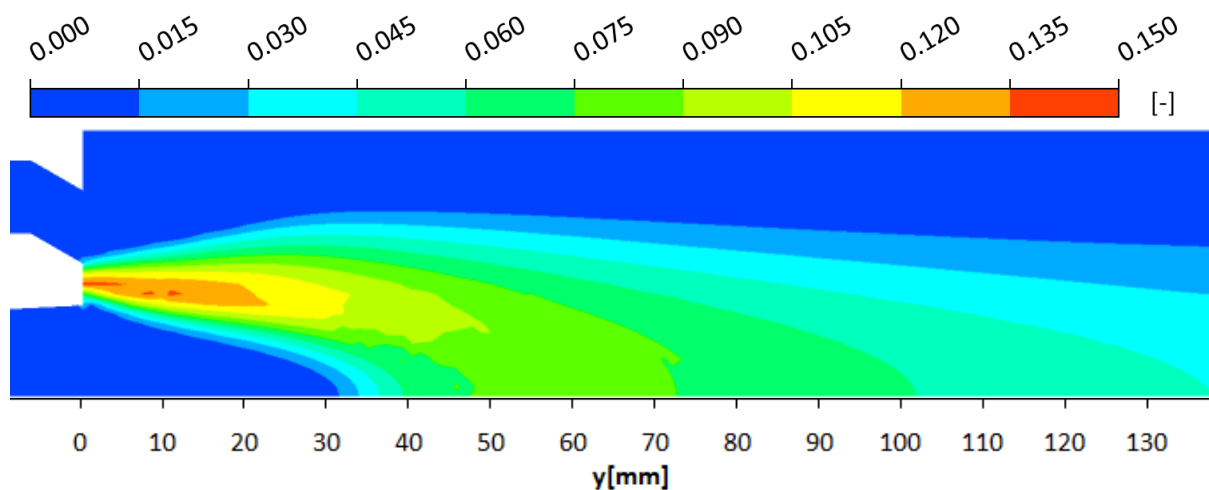


Figure 4.8: *OH mass fraction plot from simulation with detailed chemistry and diffusion*

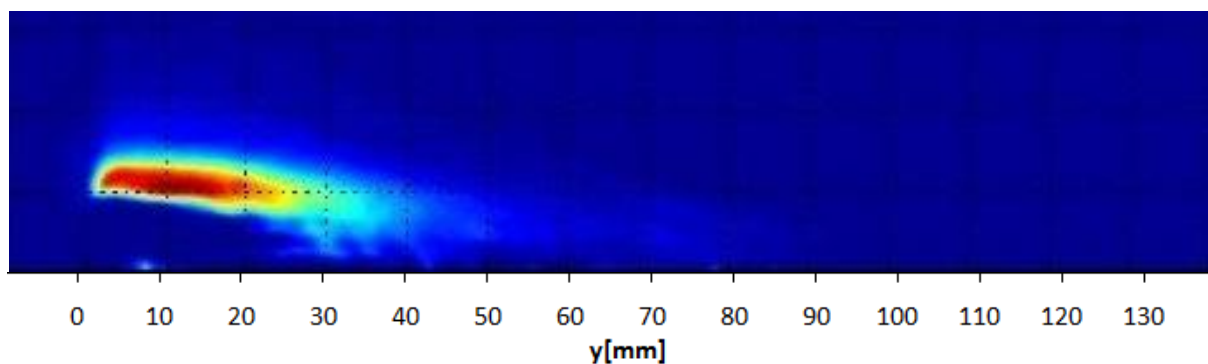


Figure 4.9: *Abel-transformed OH* image from experiment*

The dependence of the results on the choice of the constraint species can probably be best illustrated when a species which is actually not present in the simulation is chosen as constraint species. The result from using N_2 as a constraint species is shown in Figure 4.10. In this simulation N_2 is produced depending on how much the sum of all diffusion components differs from zero. The amount of N_2 in the domain in this case can be regarded as an error, which is growing from iteration to iteration. In the present simulation the largest N_2 mass fraction value occurs in the H_2 stream and reaches a steady value of almost 0.4. As a consequence the position of the flame changes considerably and also the calculation of heat release is strongly affected.

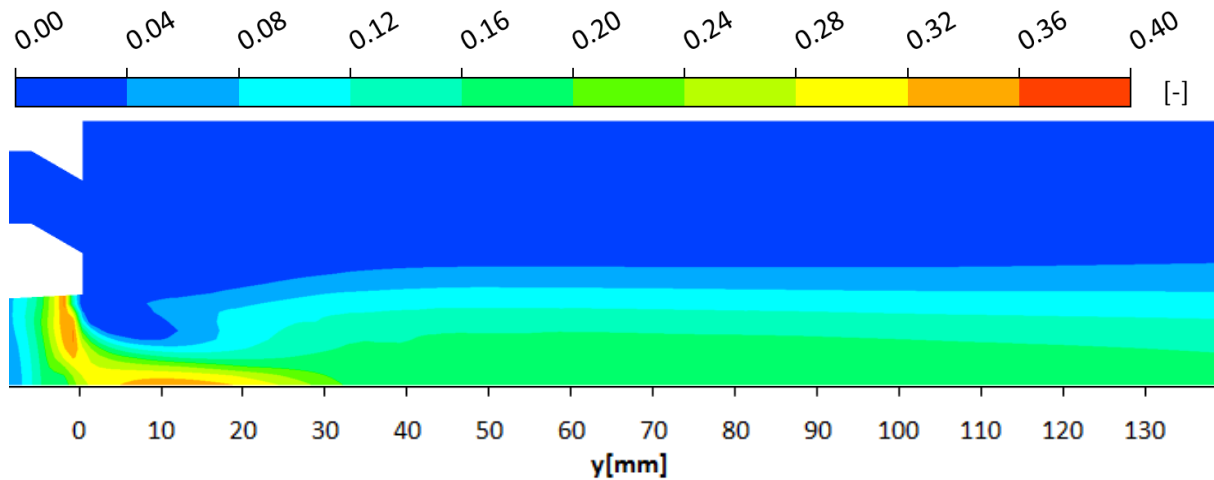


Figure 4.10: N_2 mass fraction plot from simulation with detailed chemistry and diffusion

In a simulation without the discussed implementation for diffusion the N_2 mass fraction would remain in the order of the round-off error of the solver. In this case, however, it would not be possible to obtain a solution as shown in Figure 4.8. As pointed out in section 2.5, a more sophisticated implementation in CFX is very difficult and time-consuming. In a simulation where diffusion is of great importance, and this is always the case in non-premixed laminar flames, it is advisable to use an alternative CFD package, one which has the Stefan-Maxwell equations implemented. For all turbulent flames that are presented in this thesis no individual diffusion coefficients are considered, since it is to be expected that results would rather be distorted than improved.

4.3 Turbulent Flame at Atmospheric Pressure

4.3.1 Experimental Data

Cabra et al. [14] conducted experiments on a lifted turbulent H_2/N_2 jet flame in a vitiated coflow. The combustor consists of a central H_2/N_2 turbulent jet with a coaxial flow of hot combustion products from a lean premixed H_2 /Air flame. The schematic illustration of the burner is shown in Figure 4.11. All conditions are listed in Table 4.1.

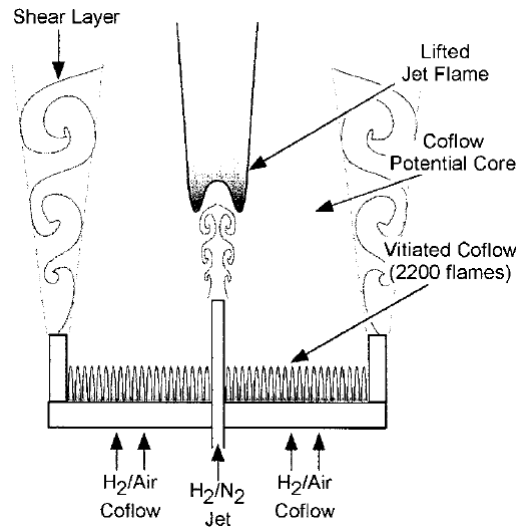


Figure 4.11: Schematic illustration of the vitiated coflow burner [14]

The central jet exits through a nozzle with an inner diameter of $d = 4.57$ mm into the coflow flame, which is stabilized on a perforated disk with an outer diameter of $D = 210$ mm. The nozzle extends 70 mm above the surface of the perforated disk.

Table 4.1: Flame and flow conditions [14]

	T [K]	v [m/s]	Y_{H_2} [-]	Y_{O_2} [-]	Y_{H_2O} [-]	Y_{N_2} [-]
Central Jet	305	107	0.0240	-	-	0.9760
Coflow	1045	3.5	-	0.1709	0.0645	0.7646

4.3.2 Numerical Simulation

Numerical simulations of the lifted H_2/N_2 flame are performed in ANSYS CFX, with the "High Resolution" advection scheme. The computational domain extends to $z/d = 40$ in axial and $r/d = 12$ in radial direction in the area downstream of the nozzle exit. A quasi-two-dimensional 2-degree wedge as described in section 4.2.2 is applied for grid generation. For the initial solution the single step reaction $H_2 + \frac{1}{2} O_2 = H_2O$ with a global reaction expression taken from Marinov et al. [63] is used. The reaction mechanism given in Table A.4 (from Jachimowski [47], modified by Wilson and MacCormack [105]) is used to calculate combustion in the external JBR as described in section 3.4.

4.3.3 Simulation with Detailed Chemistry

A grid refinement study is carried out with grid dimensions listed in Table 4.2. Starting from the coarsest grid the number of nodes is doubled in both directions, radial and axial. Simulations for grid assessment are conducted with detailed chemistry as described in section 3.1, turbulence chemistry-interaction is not considered. With the tabulation method described in section 3.3.1 the relevant range of temperatures (800-1600 K) is subdivided into about 200 steps, the range of each mass fraction into about 20 steps.

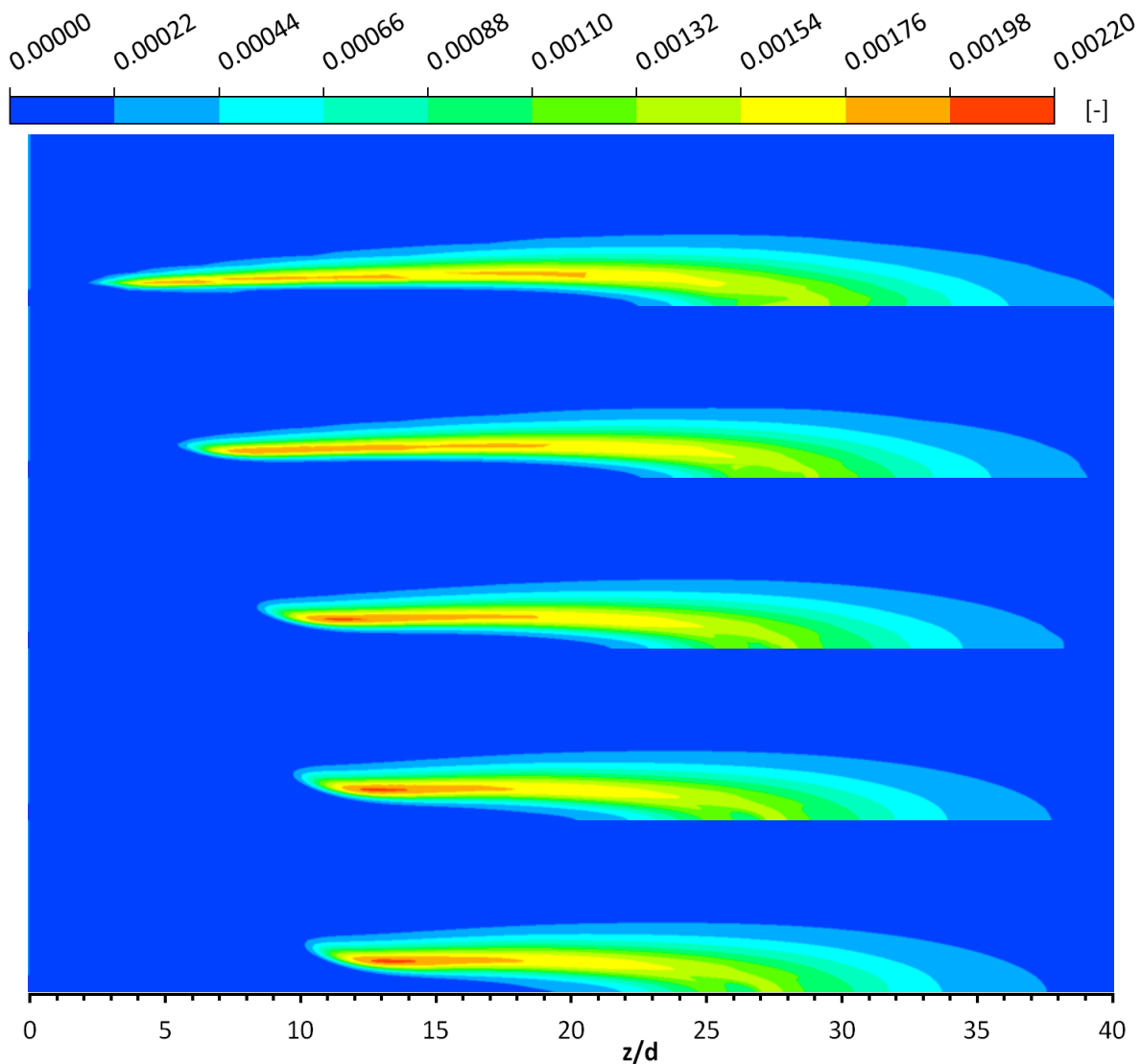


Figure 4.12: *OH mass fraction plots from simulations of the flame from Cabra et al. [14] (grids from top: XS, S, M, L, XL)*

Table 4.2: Dimensions (axial×radial) of grids used for grid convergence

name	XS	S	M	L	XL
grid size	42×21	84×42	168×84	336×168	672×336

The OH plots in Figure 4.12 as well as the temperature plots in Figure 4.13 show that the results depend on the size of the employed grid. The lift-off height on the coarsest grids is notably shorter than for the finer grids. The plots for the two finest grids show almost no differences.

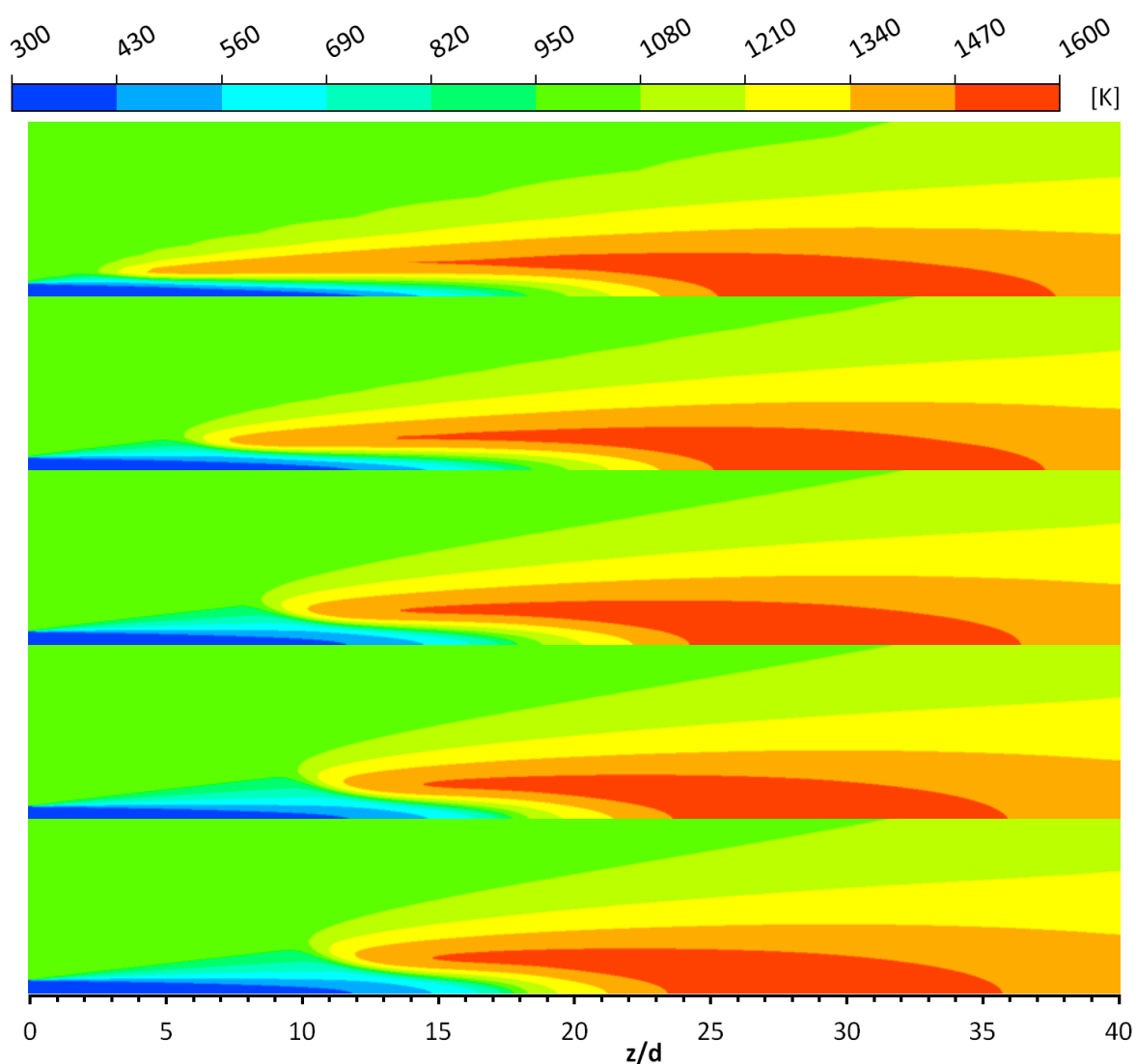


Figure 4.13: Temperature plots from simulations of the flame from Cabra et al. [14] (grids from top: XS, S, M, L, XL)

OH profiles in Figure 4.14 and temperature profiles in Figure 4.15 show results from simulations compared with experiments. The lift-off height in the experiments was at $z/d \approx 10$. Therefore the graphs at $z/d = 1$ and $z/d = 8$ can at most give information with respect to the quality of simulating the mixing process, since contributions from reactions are marginal.

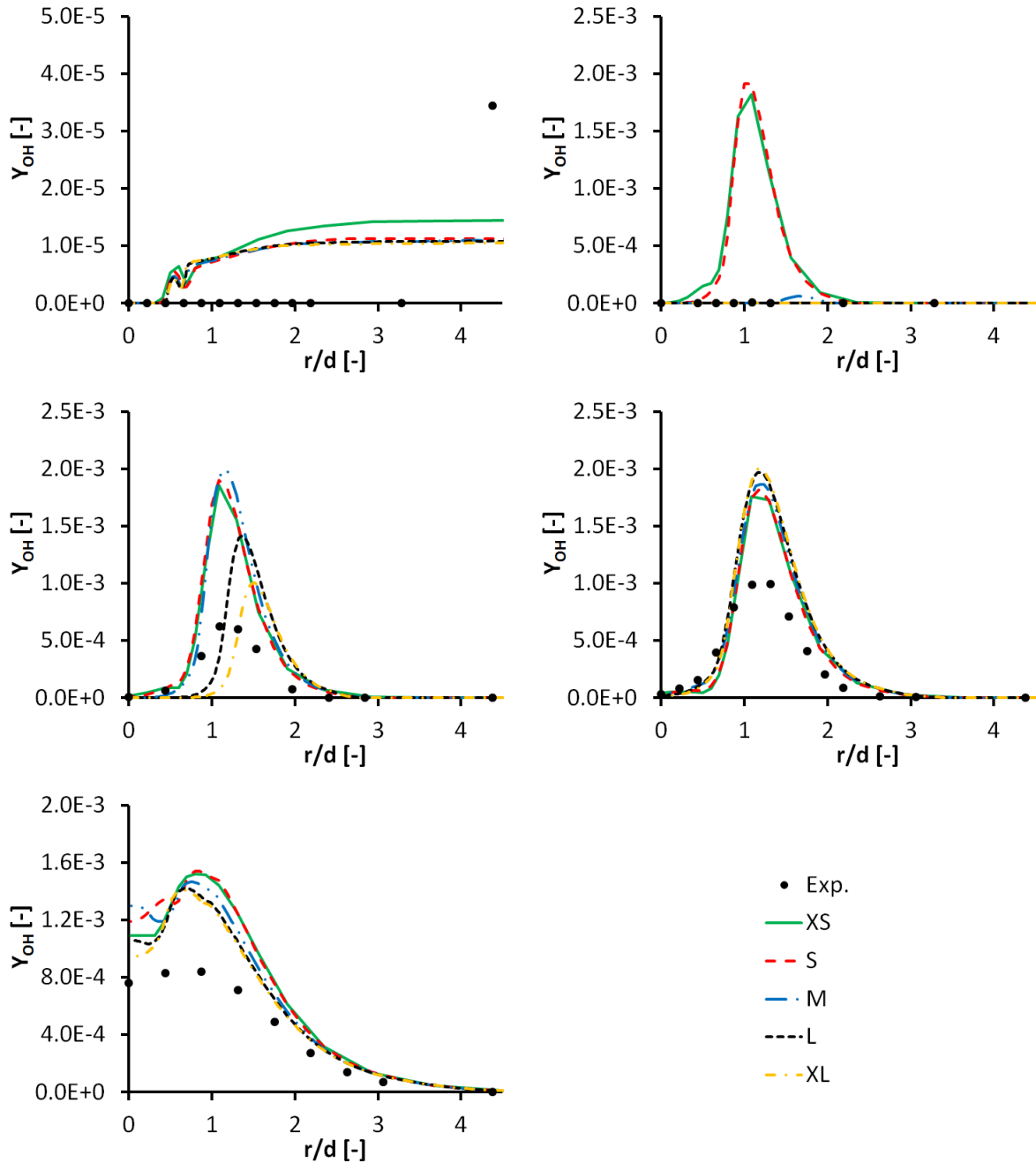


Figure 4.14: OH mass fraction profiles for $z/d = 1, 8, 11, 14$ and 26 (from top left) from simulations of the flame from Cabra et al. [14]

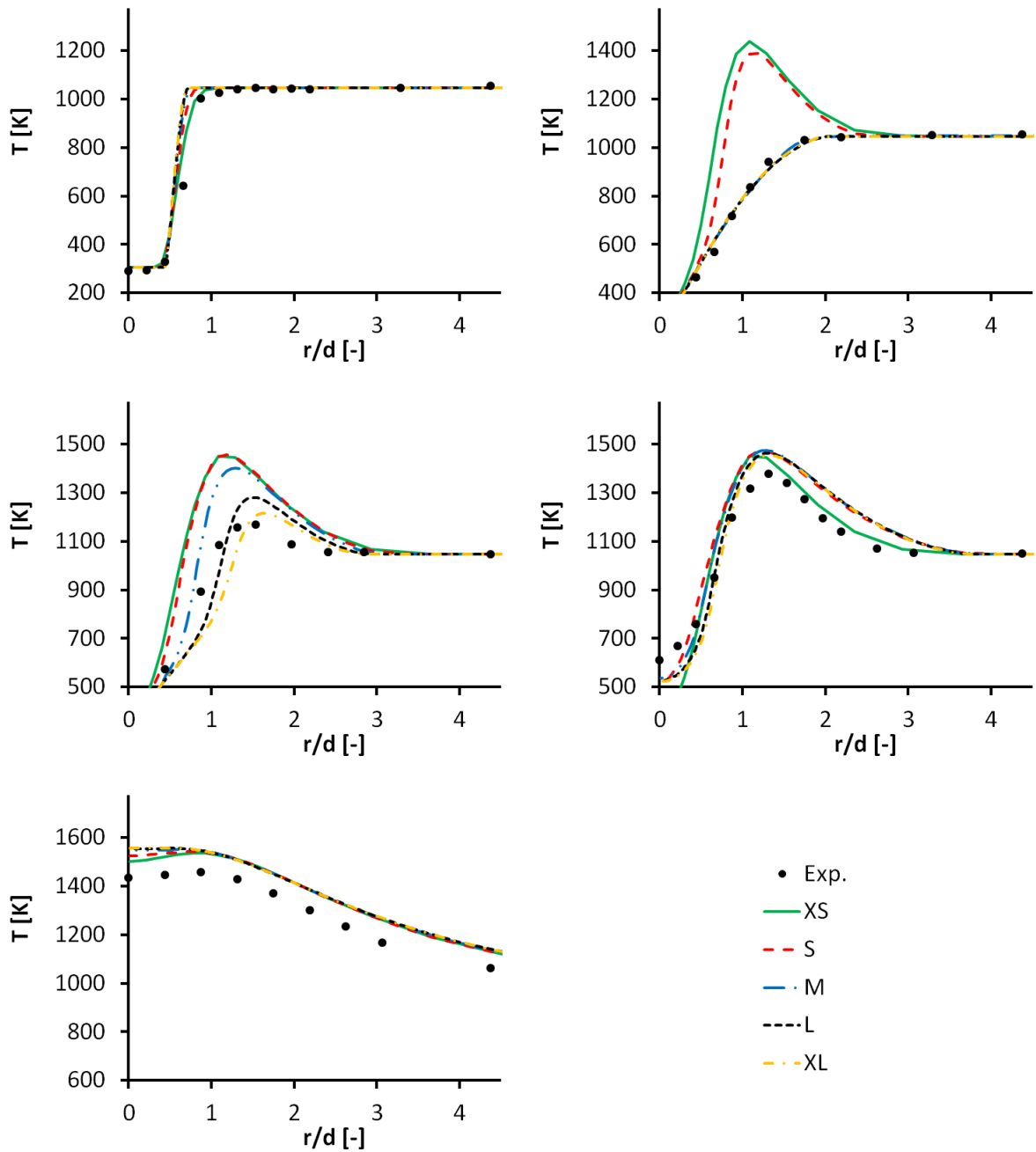


Figure 4.15: Temperature profiles for $z/d = 1, 8, 11, 14$ and 26 (from top left) from simulations of the flame from Cabra et al. [14]

Only on the two coarsest grids is the lift-off height considerably smaller than $z/d = 8$. The lift-off height for the three finest grids is close to $z/d = 11$, which becomes apparent on the corresponding graphs. At $z/d = 14$ and $z/d = 26$ the results from all grids are close to each other. The results are considerably different at $z/d = 11$. The reason for the clear differences is, that the lift-off heights of the three finest grids are very close to $z/d = 11$. But this is also the only place in the

entire domain, where further grid refinements might have a significant effect on the results. Therefore further simulations were carried out on grid M (168×84 nodes). With relatively small computational effort (compared to grids L and XL) it is possible to illustrate how certain factors in the simulation affect the results (see following subsections).

When compared to experimental data it becomes evident that all values of temperatures and OH mass fractions in the simulations are beyond the measured values. Simulations of the constant volume reactor showed that the increase in temperature is correctly predicted. So it is safe to assume that the total amount of heat release can be reproduced correctly. Temperatures may still be higher in the simulation as e.g. radiation losses are not included.

The agreement of profiles from simulations with measured values also depends on how well the simulation can reproduce the exact position of the flame. The most important factor influencing the lift-off height is probably the ignition delay time, which is dependent on the applied reaction mechanism. But it is also important how the flow solver accounts for the mixing of the components. This does not only influence the lift-off height but also the dimension of the flame in both radial and axial direction. Species diffusion according to equation (2.26) is composed of laminar and turbulent diffusion. In turbulent flow it is assumed that turbulent diffusion is much larger than laminar (and based on the findings in section 4.2 species specific molecular diffusion is not included in CFX). Turbulent diffusion is defined by turbulent viscosity μ_t and the turbulent Schmidt number Sc_t . Therefore changes to the standard values of Sc_t or the model constants of the employed turbulence model (which define μ_t) could possibly produce better agreement with experimental data.

4.3.4 Influence of Tabulation

The tabulation of temperatures and mass fractions as described in 3.3.1 reduces the computational cost. But this comes along with a reduction of accuracy, as illustrated in the OH mass fraction plots in Figure 4.16 and the temperature plots in Figure 4.17. Results from three different simulations (all run on grid M) are compared. The first simulation is the same as in the previous section with the same table size. For the second simulation the relevant range of each mass fraction has been subdivided in about 30 (instead of 20) steps, while still about 200 steps are used for temperature tabulation. In the third simulation no tabulation is used – the stiff system of ODEs is solved at all times.

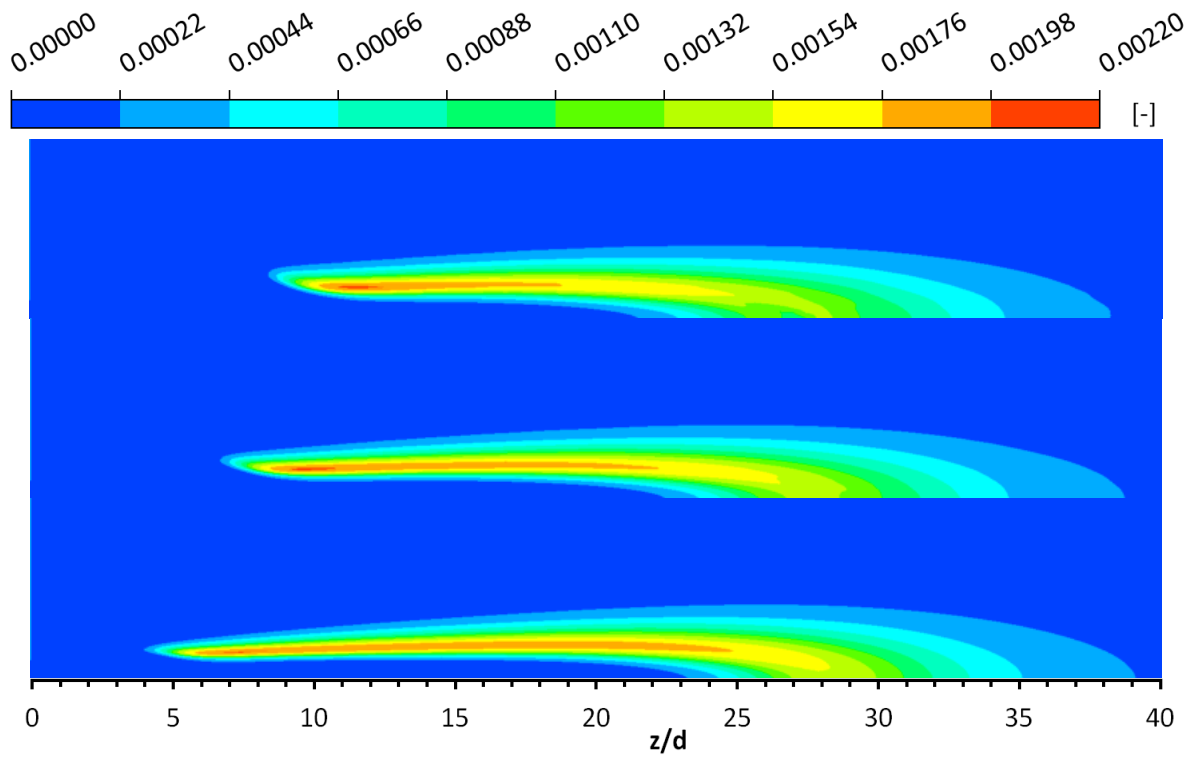


Figure 4.16: *OH mass fraction plots from simulations of the flame from Cabra et al. [14]; top: 20 mf-steps, middle: 30 mf-steps, bottom: no tabulation*

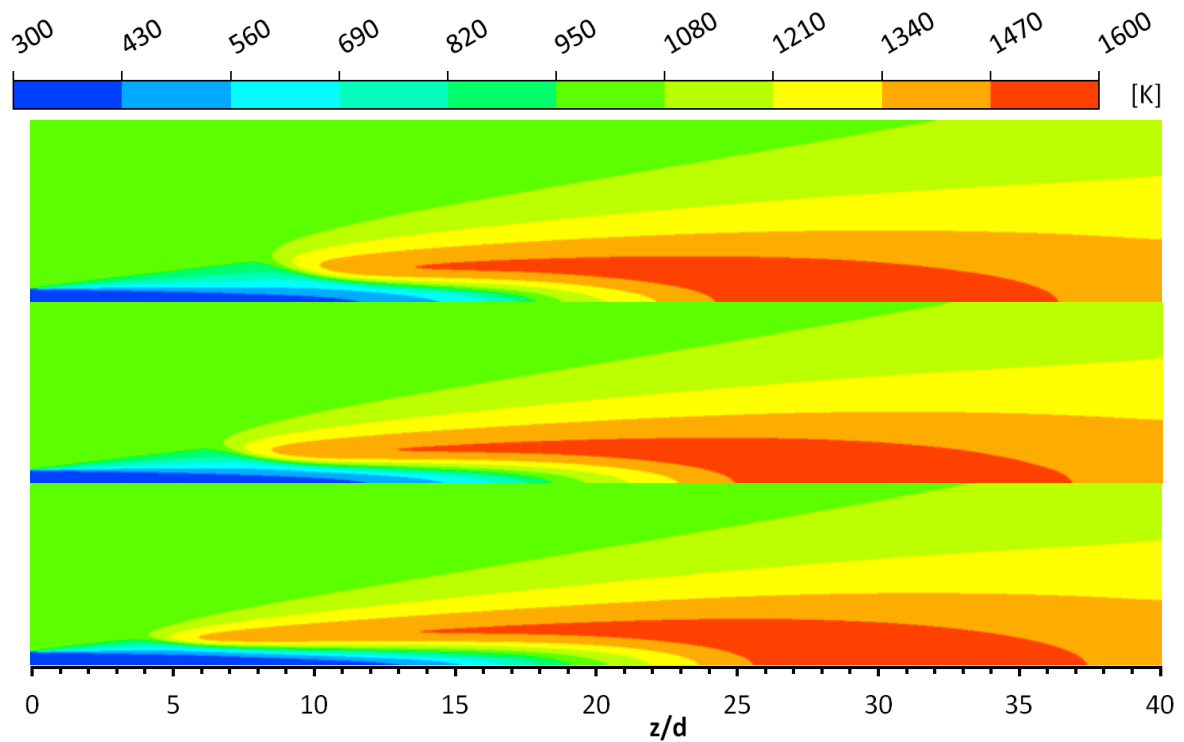


Figure 4.17: *Temperature plots from simulations of the flame from Cabra et al. [14]; top: 20 mf-steps, middle: 30 mf-steps, bottom: no tabulation*

The two figures show that for the given test case the application of the tabulation method results in an increase of the lift-off height. This is to be expected since with the applied tabulation method all factors influencing the reaction process are evaluated separately (see also section 3.3.1). The two figures of course also show that, the finer the table gets, the closer the results get to the solution of the simulation without tabulation. In the present case, the number of cells in the table increased by 50% when the finer table was used. The additional time required for generating the cells resulted in an increase of 25 % in total computational time. However, this is still only 25% of the total computational time that is required to run the simulation without the tabulation method.

4.3.5 Influence of Reaction Mechanism

In the previous calculations the modified reaction mechanism of Jachimowski (see Table A.4) was used. In Figure 4.18 and Figure 4.19 the obtained results are compared with simulations where the reaction mechanism of Ó Conaire et al. [69] (see Table A.6) is used. For the two simulations the same spacing in the tabulation is applied (see section 4.3.3). There is a distinct difference in the appearance of the flame depending on which reaction mechanism is applied. Since in both cases the same thermodynamic database is used, the different results can solely be linked to the effect of chemical kinetics.

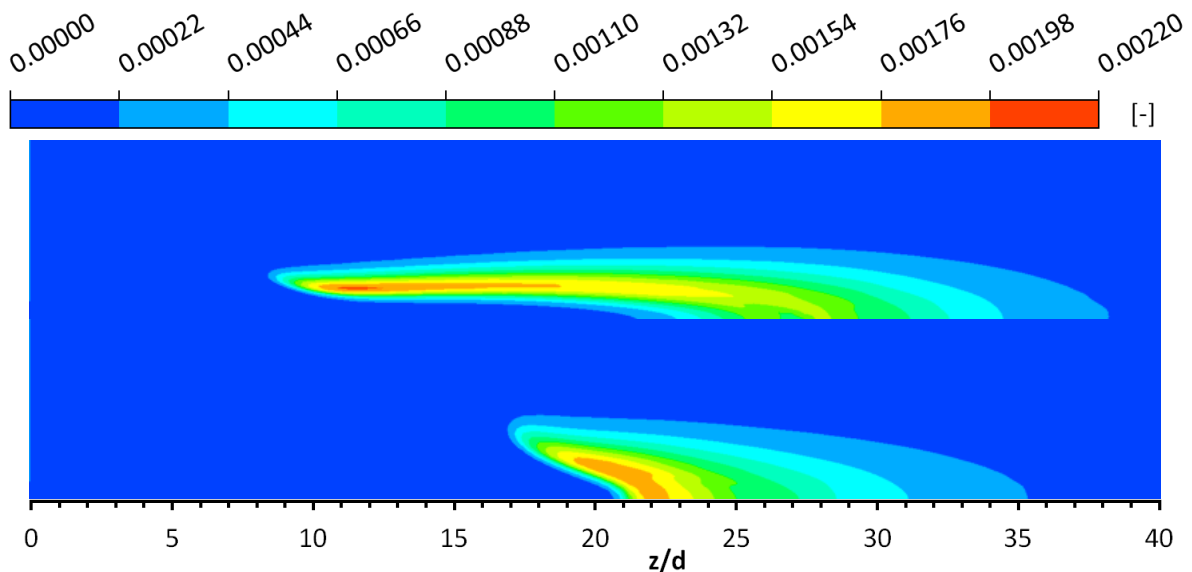


Figure 4.18: *OH mass fraction plots from simulations of the flame from Cabra et al. [14]; above: Jachimowski, below: Ó Conaire*

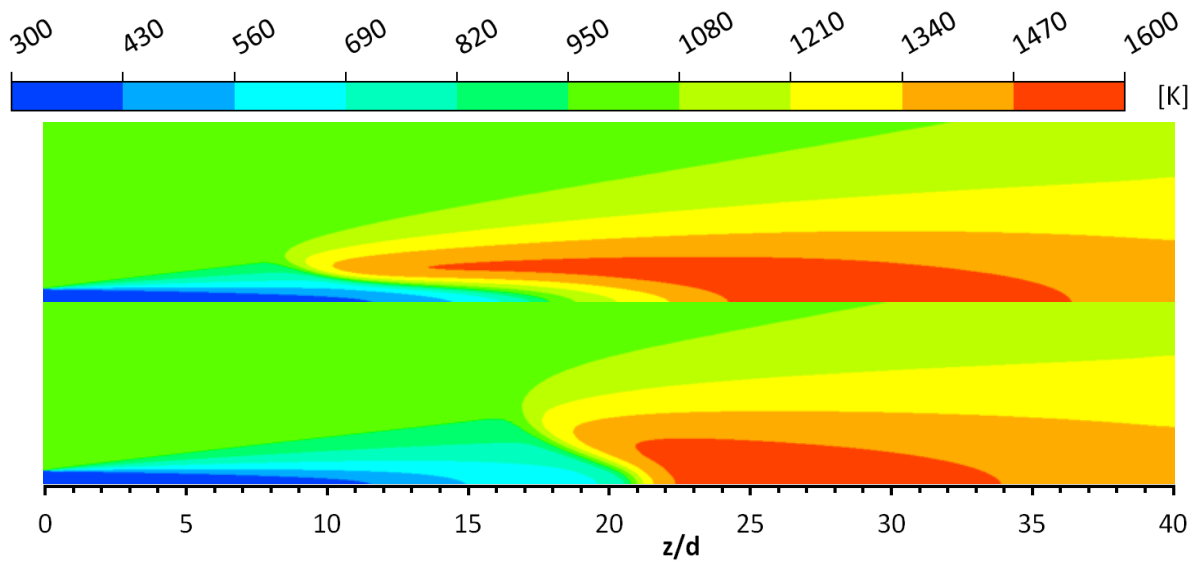


Figure 4.19: Temperature plots from simulations of the flame from Cabra et al. [14]; above: Jachimowski [47], below: Ó Conaire et al. [69]

Figure 4.18 and Figure 4.19 distinctly and visibly show the same tendency that is already observable in Figure 4.3 in the comparison of the two reaction mechanisms. In the constant volume reactor described in section 4.1.2 progress starts to show later with the mechanism of Ó Conaire et al. [69] and still the final state is reached earlier. Analogously in the simulation of the flame from Cabra et al. [14] with the mechanism of Ó Conaire et al. [69] the lift-off height is considerably larger and still the flame is significantly shorter. Given that the lift-off height in the experiments was at $z/d \approx 10$ one can conclude that for the set-up at hand the modified Jachimowski mechanism (see Table A.4) delivers better results. However, no conclusions can be drawn for combustion at high pressures as the behavior of the reactions mechanisms might differ considerably depending on existing conditions (see section 4.1.2).

4.3.6 Influence of Turbulence Chemistry Interaction

As described in section 3.2, two assumed PDFs are used to account for turbulence chemistry interaction: one for temperature and one for composition. To show how they affect the results, four different simulations are compared with each other in Figure 4.20 and Figure 4.21. In the first simulation the turbulence-chemistry interaction is not included (no PDF). In the second simulation only temperature fluctuations are considered (T-PDF), while in the third only fluctuating mass fractions are implied (Y-PDF). In the fourth simulation turbulence-chemistry interaction is included as described in section 3.2 (T- and Y-PDF).

For all calculations the modified reaction mechanism of Jachimowski (see Table A.4) was used. The rate constants were tabulated as described in section 3.3.2. The temperature range (300 K-3000 K) was covered with 270 equidistant steps, while for the fluctuation intensities I_T (in the range from 0.0 to 0.8) 200 evaluation points were used.

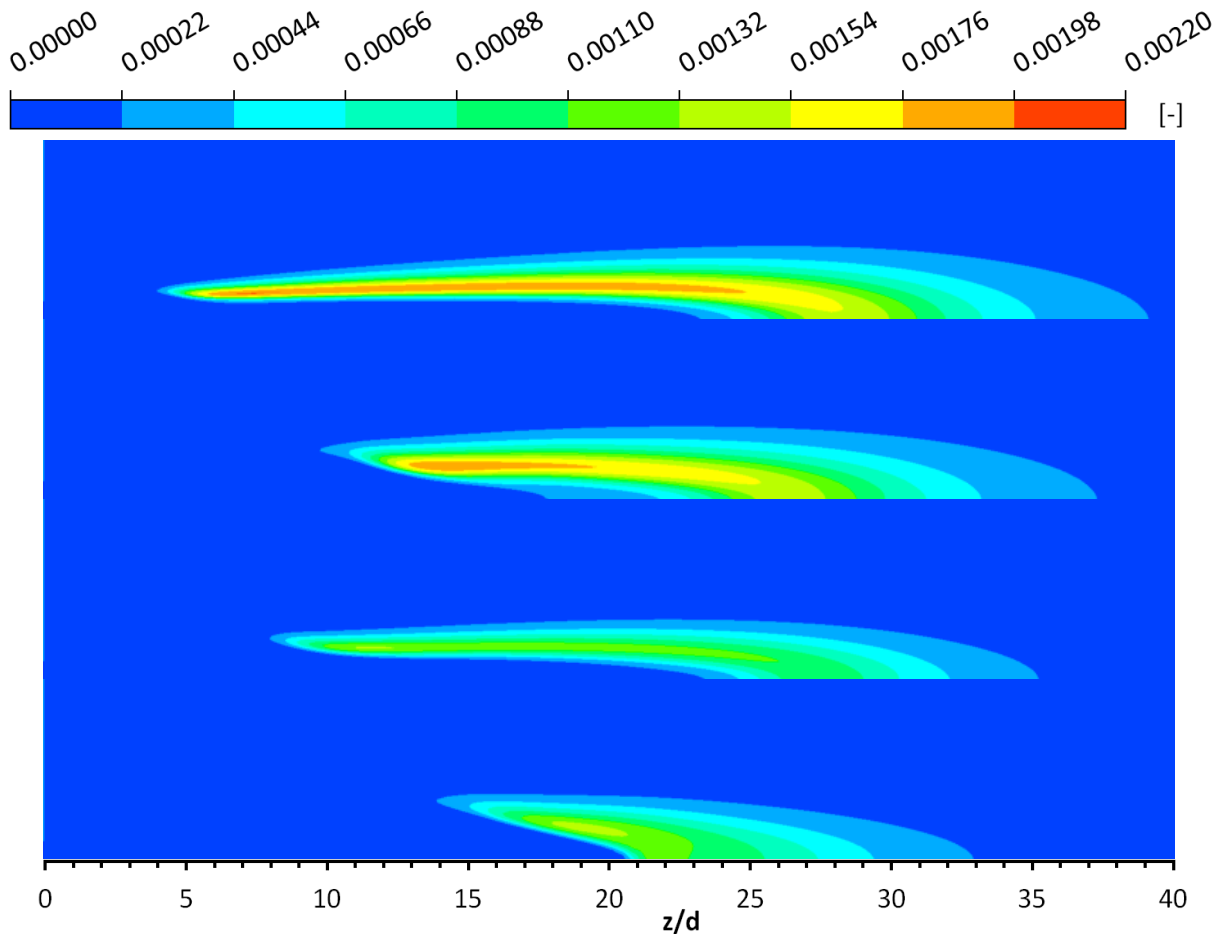


Figure 4.20: *OH mass fraction plots from simulations of the flame from Cabra et al. [14]; from the top: 1. no PDF, 2. T-PDF, 3. Y-PDF, 4. T- and Y-PDF*

Since the assumed PDF of temperature acts on the rate constants, the observed effect of its application always has to be seen in the context of the reaction mechanism that has been applied. For the modified mechanism of Jachimowski in Figure 4.20 and Figure 4.21 a higher lift-off height and a shorter and thicker flame is observed when compared to computations without turbulence-chemistry interaction. For other mechanisms (not shown here) this observation can be the exact contrary (see [19]).

The effects arising from using the assumed PDF of composition are independent of the applied reaction mechanism. Values of σ_Y close to zero are approaching the solution without turbulence-chemistry interaction, while increasing values of σ_Y represent states of growing unmixedness. This then corresponds to decreasing rates of progress. Accordingly, the lift-off height is larger than in the case without turbulence-chemistry interaction. In addition the amount of OH that is present in the flame is becoming smaller.

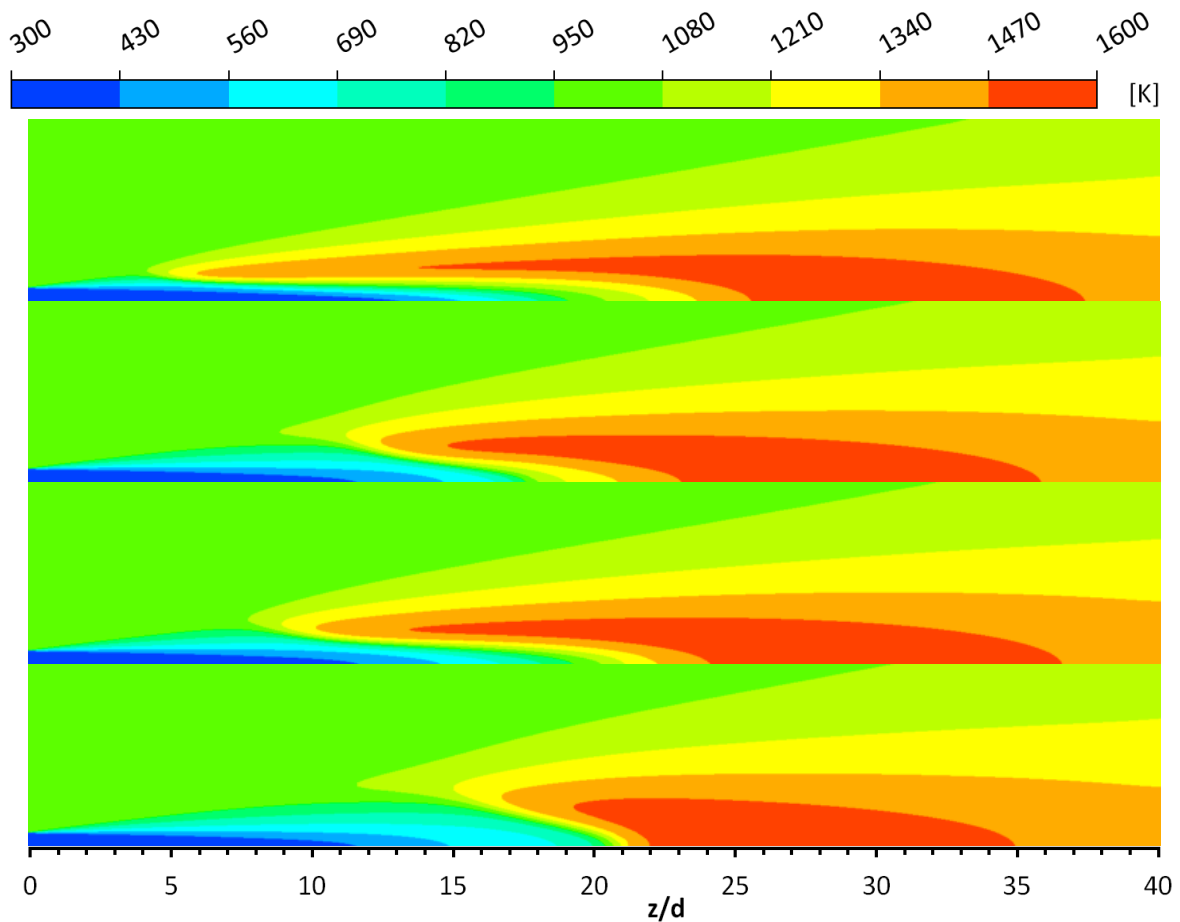


Figure 4.21: Temperature plots from simulations of the flame from Cabra et al. [14]; from the top: 1. no PDF, 2. T-PDF, 3. Y-PDF, 4. T- and Y-PDF

Plots from the simulation where the PDFs of temperature and composition are jointly applied appear to have the effects of both assembled. In this case (last plot in Figure 4.20 and Figure 4.21) the flame from Cabra et al. [14] has the largest lift-off height and small peak values of OH mass fractions. Corresponding plots for the temperature fluctuation intensities I_T and the sum of species mass fraction variances σ_Y^2 are shown in Figure 4.22 and Figure 4.23, respec-

tively. Close to where the flame touches the axis and where the cold jet flow mixes with the hot co-flow large gradients of temperature and of mass fractions exist. At these places the production source terms in equations (3.57) and (3.59) contribute to the large values of I_T and of σ_Y^2 that can be observed in the figures below.

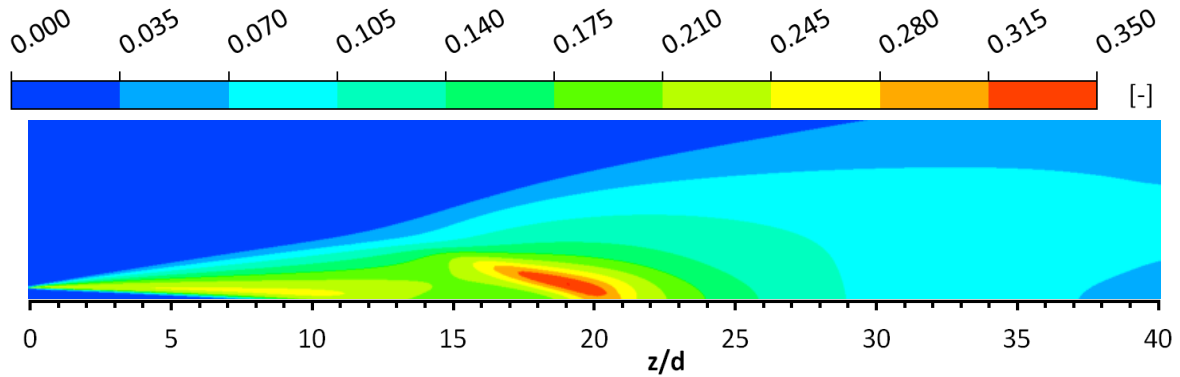


Figure 4.22: I_T plot from the simulation of the flame from Cabra et al. [14] with T- and Y-PDF

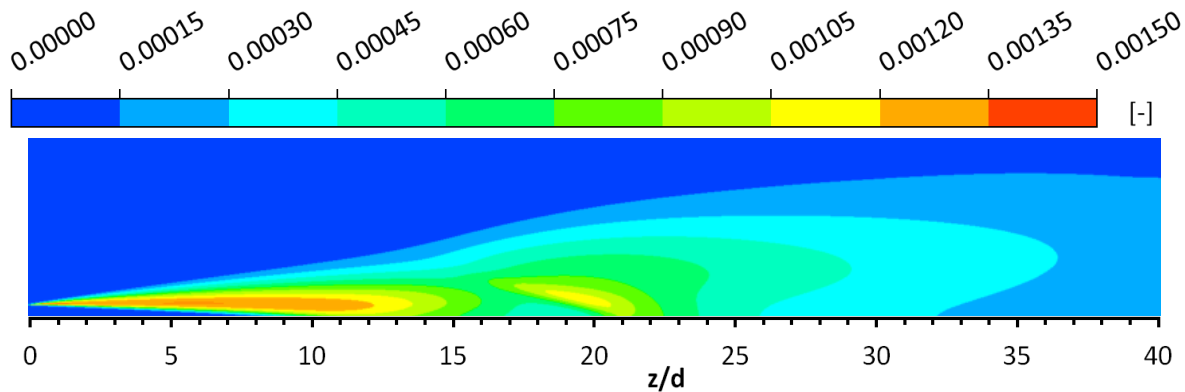


Figure 4.23: σ_Y^2 plot from the simulation of the flame from Cabra et al. [14] with T- and Y-PDF

The OH mass fraction profiles and the temperature profiles from the four different simulations are compared with each other in Figure 4.24 and Figure 4.25. The graphs at $z/d = 1$ give rather an information on the definition of the boundary conditions. In all simulations the lift-off height is too high, as can be seen in the graphs at $z/d = 8$. Here the simulation with both PDFs shows the best agreement with measured data. However, in all other graphs the case where both

PDFs are considered probably produces the worst results. The reduction of OH mass fractions through the use of the assumed PDF of composition brings the profiles closer to the experimental results.

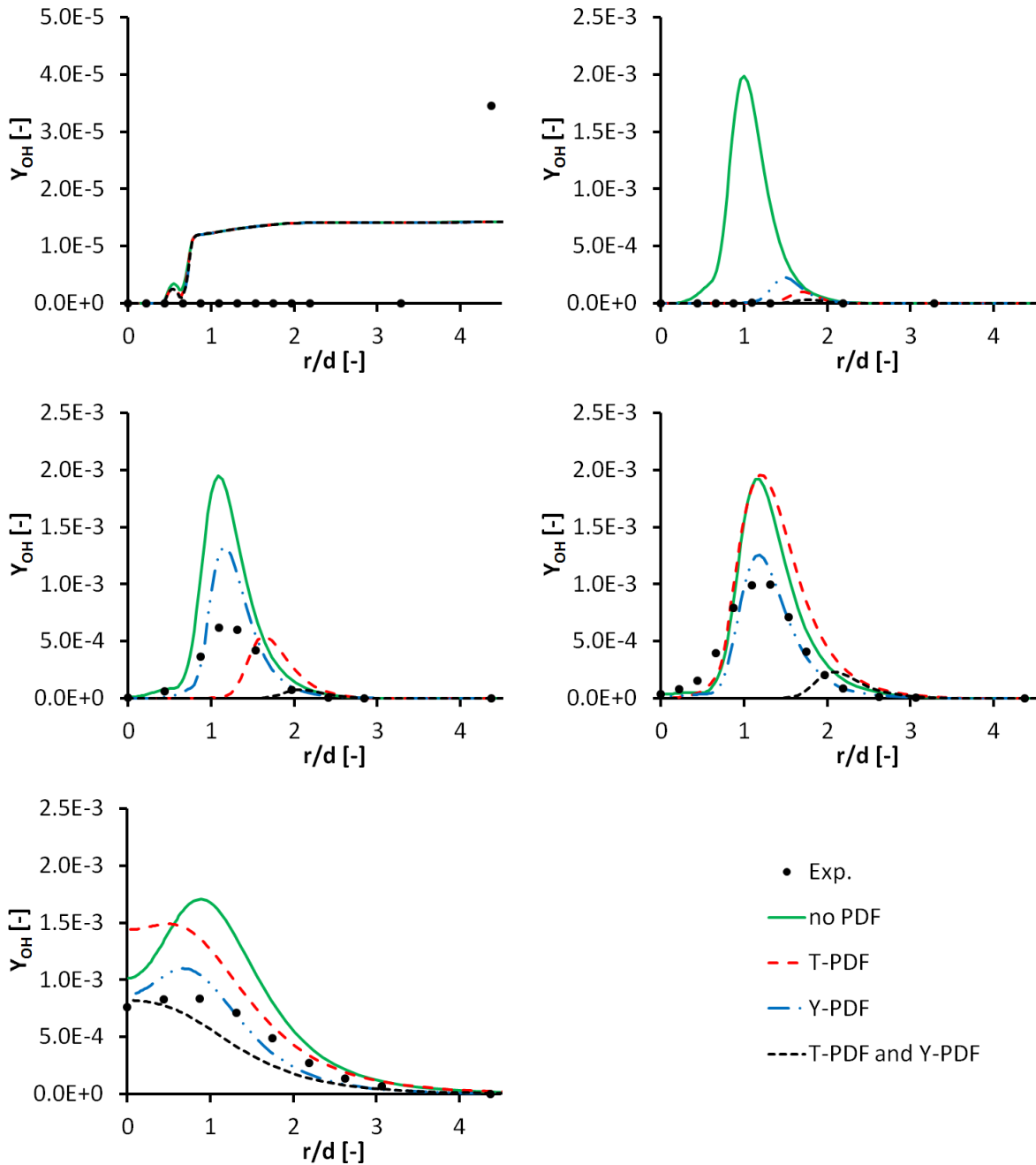


Figure 4.24: Influence of assumed PDF approaches on OH mass fraction profiles at $z/d = 1, 8, 11, 14$ and 26 (from top left) from simulations of the flame from Cabra et al. [14]

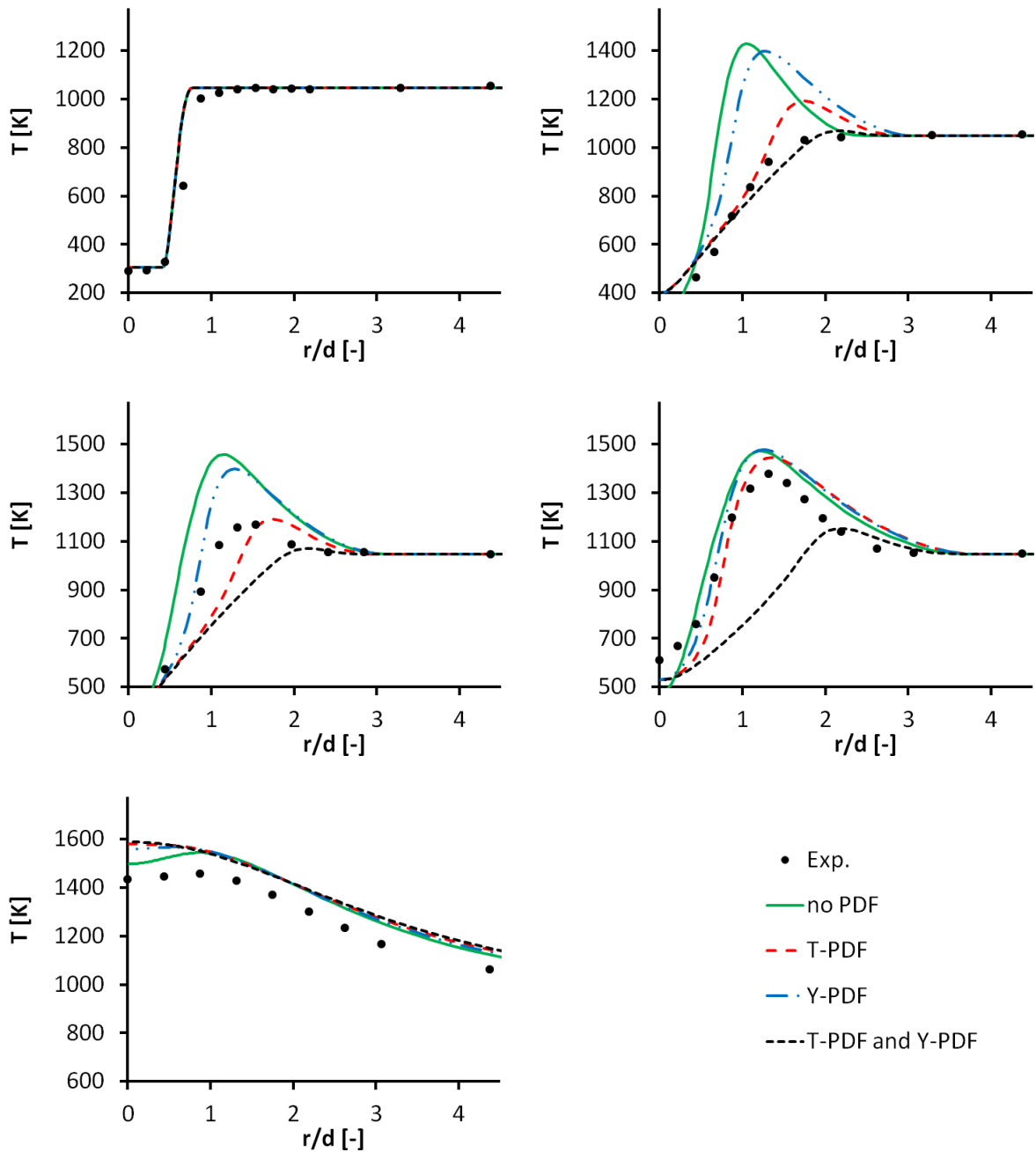


Figure 4.25: Influence of assumed PDF approaches on temperature profiles at $z/d = 1, 8, 11, 14$ and 26 (from top left) from simulations of the flame from Cabra et al. [14]

The results presented suggest that turbulence-chemistry interaction (as presented in sections 3.2 and 3.3.1) is properly implemented and its use for the flame from Cabra et al. [14] justified, since its application improves the agreement with experimental data to some extent. However, the quality of the results also depends significantly on the applied reaction mechanism (see section 4.3.5). With the

opposing characteristics that the reactions mechanisms showed for different conditions (as shown in section 4.1.2) it has to be concluded, that for the application to a rocket engine flame the influence of all factors has to be investigated under conditions (e.g. at high pressures) which are representative for LPRE flames.

4.4 Turbulent Flame at High Pressure

4.4.1 Experimental Data

At the beginning of the 1990s the cryogenic test facility Mascotte [36] was developed by ONERA. It is possible to operate the test facility with combustion chamber pressures over 60 bar. This is higher than the critical pressure of oxygen ($p_{c,O_2} = 50.43$ bar) and therefore allows to run experiments at conditions which are similar to those in real rocket engines, e.g. like the Ariane 5 Vulcain Engine [23].

Data from Mascotte experiments at 60 bar were chosen as RCM-3 test case for the 2nd International Workshop on Rocket Combustion Modelling [37]. The test case with the operating point at 60 bar is called A 60 case. The combustion chamber has a square cross section. Propellants are injected to the combustion chamber through a single coaxial injector with liquid oxygen in the core and hydrogen in the annulus. The details for operating conditions are listed in the table below. This test case has also been used in several papers on modeling supercritical combustion (see e.g. [9], [15], [78], [79]).

Table 4.3: Operating conditions of RCM-3 test case [37]

	H ₂	O ₂
Pressure [bar]	60	60
Mass flow [g/s]	70	100
Temperature [K]	287	85
Density [kg/m ³]	5.51	1177.8
Velocity [m/s]	236	4.35

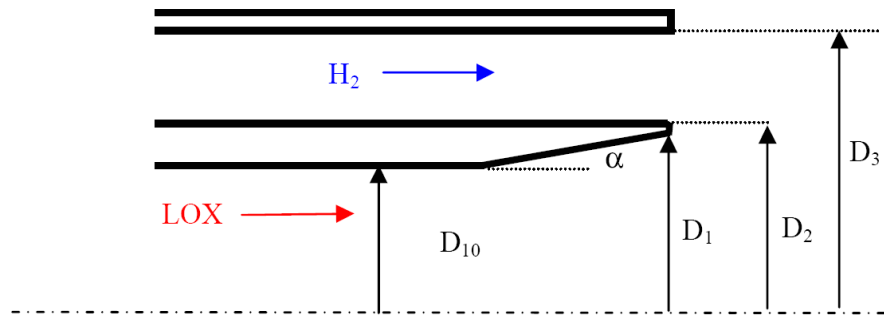


Figure 4.26: Mascotte single injector geometry [68]

The injector geometry is taken from the description of the Mascotte single injector RCM-2 test case for the 3rd International Workshop on Rocket Combustion Modelling [68]. Dimensions are given in Table 4.4.

Table 4.4: Dimensions of the Mascotte single injector illustrated in Figure 4.26

D_1 [mm]	D_2 [mm]	D_3 [mm]	D_{10} [mm]	α [°]
5.0	5.6	10.0	3.6	8

Oxygen is injected with a relatively low velocity but at a very high density, while hydrogen is injected at high speed and low density (see Table 4.3). Once ignited the flame stabilizes in the shear layer between the two propellants as illustrated by the OH* emission images shown in Figure 4.27. Heat transferred from the flame causes an expansion of the oxygen jet. The co-flowing hydrogen stream is thus bent away from the axis. Expansion is limited through the wall of the combustion chamber. A bulge occurs, which is typical for LPRE flames (see also Figure 4.28 and illustrations in section 6.3). Upstream of the bulge a recirculation zone forms between hydrogen stream, outer wall and faceplate. Since the combustor is operated with hydrogen in excess, the oxygen jet is completely consumed by the flame.

4.4.2 Numerical Simulation

For numerical simulation the combustor is approximated by a quasi-2D axisymmetric representation. Again, a 2° wedge is chosen for the domain. The grid, which is consisting of hexahedral elements only, is generated in the same way as described in sections 4.2 and 4.3. The thin surface at the axis is assigned to be an adiabatic wall with “Free Slip” option. In circumferential directions two symmetry planes are used. The domain extends 400 mm in axial and 25 mm in

radial direction. For initial simulations a grid with $200 \times 49 \times 2$ nodes (axial \times radial \times circumferential) was used, which later was refined to $399 \times 97 \times 2$ nodes. The grid is clustered close to the injector in radial and axial direction. The nozzle at the exit was not included. Instead a constant pressure boundary condition at the outlet was chosen (0 Pa relative to the reference pressure of 60 bar). Mass flow rates and temperatures at the inlets are prescribed according to Table 4.3. All other boundaries are adiabatic no slip walls. Turbulence is modeled with the k- ϵ -model, with a turbulence intensity of 5 % at the injector. The length of the inlet duct is chosen to be 40 mm.

The material in the multi-component flow is a variable composition mixture containing 8 species: H_2 , O_2 , H_2O , H, O, OH, HO_2 and H_2O_2 . Transport equations for 7 of these species are solved. H_2O is chosen to be calculated from a constraint equation, making sure that the mass fractions of all components sum up to unity. Only O_2 is treated as a real gas according to equation (2.9). All other species are treated as ideal gases and ideal mixing applies. Following the finding of section 4.2 no species specific diffusion coefficients are considered and it is assumed that turbulent diffusion is much more dominant. The eddy dissipation model (EDM) that is implemented in ANSYS CFX has been used with the single step reaction $\text{H}_2 + \frac{1}{2} \text{O}_2 = \text{H}_2\text{O}$ to obtain an initial solution.

The Upwind option was chosen as advection scheme and the first order backward Euler option as transient scheme with time steps of 1×10^{-5} s. The "Thermal Energy" option is chosen to model heat transfer, since it was not possible to obtain a solution with the total energy equation when oxygen with the Redlich-Kwong equation is involved in the simulation of the flame.

4.4.3 Simulation with Detailed Chemistry

OH* emission images from the experiments are shown in Figure 4.27. The OH mass fractions from numerical simulations are plotted in Figure 4.28. The underlying simulation was carried out with the modified reaction mechanism of Jachimowski (see Table A.4). The plot shows a good agreement with experimental data as far as the flame zone and the expansion angle are considered. The flame in the simulation shows a small lift-off, which in the Abel-transformed emission image seems not to be present. One reason for this could be the ignition delay time of the applied reaction scheme. In simulations with EDM, where combustion is only linked to turbulence and not to reaction kinetics, it stabilizes at the injector.

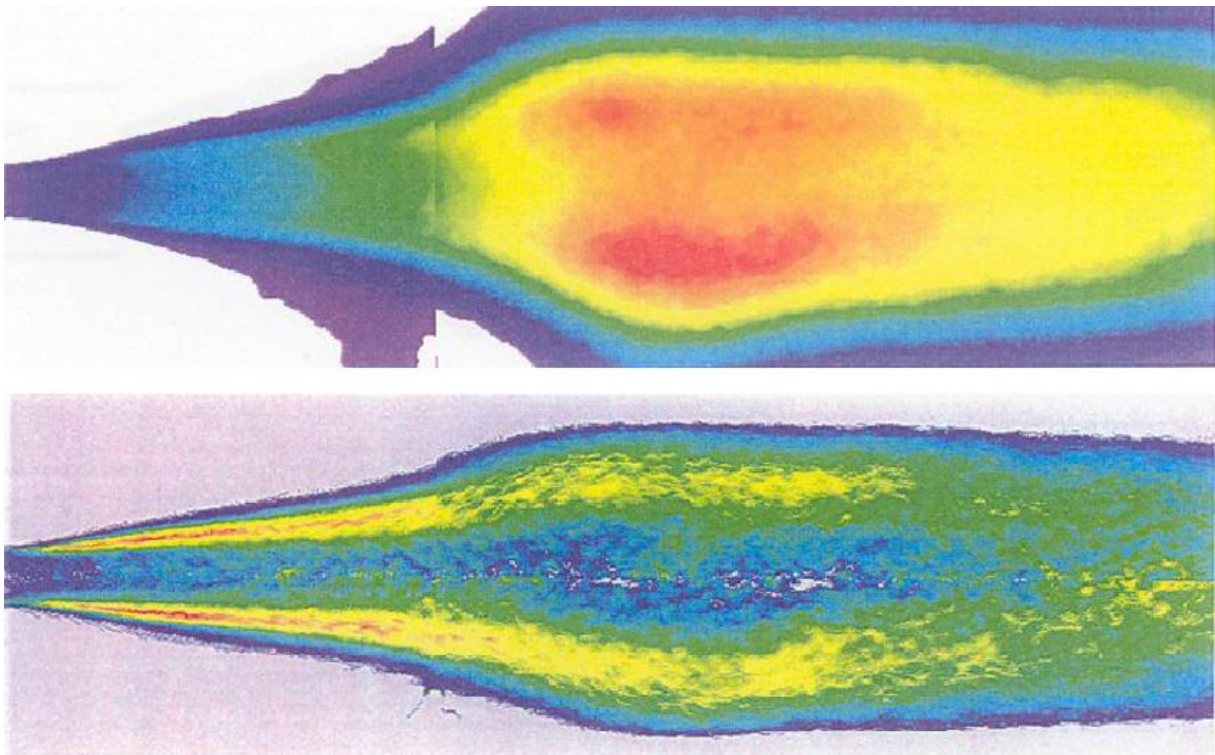


Figure 4.27: OH^* contours from the Mascotte single injector test case [37] (top: average emission image, bottom: Abel-transformed emission image)

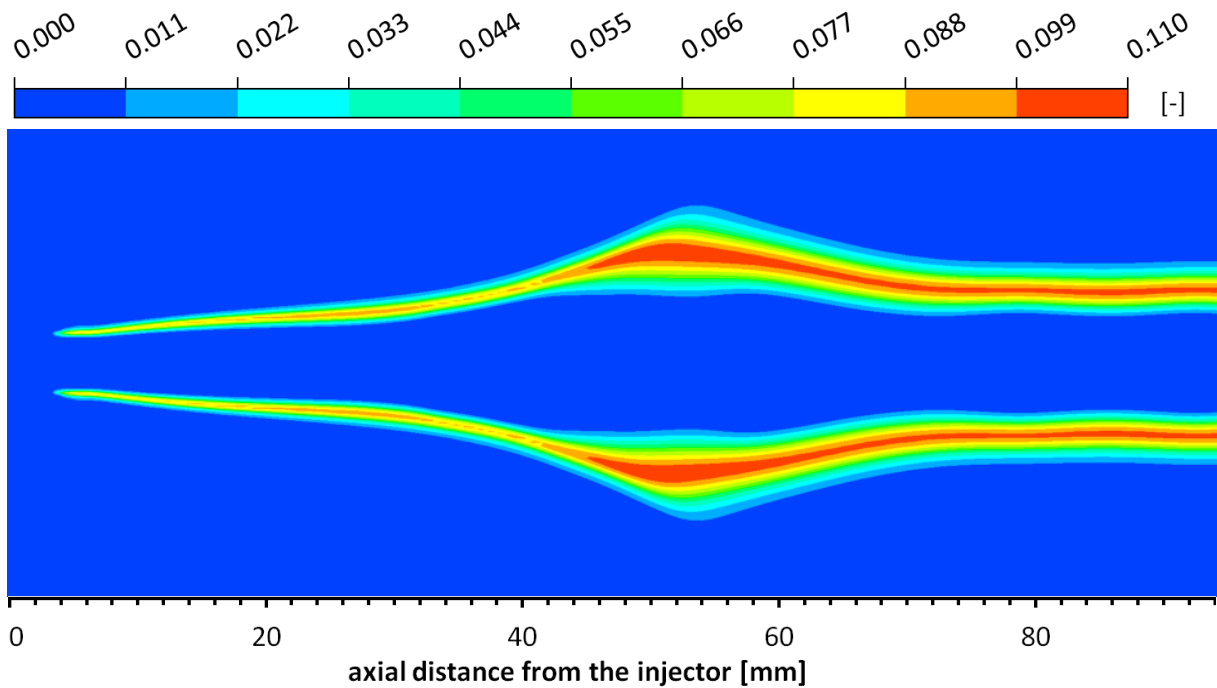


Figure 4.28: OH mass fractions plot from the simulation of the Mascotte single injector test case [37]

Another reason for the lift-off of the flame might be the fact, that the thermal energy equation is used. High Mach numbers exist only in the vicinity of the annulus, but the high kinetic energy of the hydrogen stream is not properly accounted for. A higher temperature in the shear layer would cause a shorter ignition delay time and thus bring the flame closer to the injector. The consideration of multicomponent diffusion could cause a better mixing of the propellants and thus move the flame closer to the injector as well.

A comparison of temperature profiles along the axis is shown in Figure 4.29. The peak temperature of the experiments is reproduced well. The decay in temperature along the axis is in the experiments not as fast as predicted in the simulations. Even though Mach numbers in this region are not so high, this might also be caused by the use of the thermal energy equation.

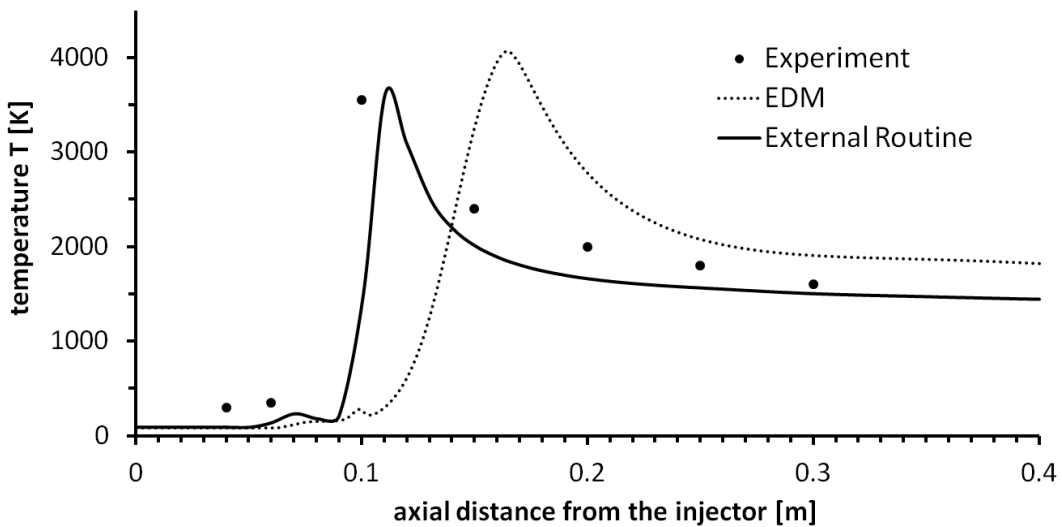


Figure 4.29: Temperatures in the Mascotte single injector [37] in experiment and simulations

4.4.4 Influence of Reaction Mechanism

In Figure 4.30 simulations with the two different reaction mechanisms are compared by means of OH mass fraction plots. Simulations with the mechanism of Ó Conaire et al. [69] show a slightly smaller lift-off height and result in a somewhat longer flame. The smaller lift-off height is supported by simulations of the constant volume reactor as shown in Figure 4.4, which predict a shorter ignition delay time. The longer flame length seems to be in contrast to this finding. However, for Figure 4.4 only the stoichiometric mixture is investigated, while in the flame multiple configurations exist (see e.g. Figure 4.6).

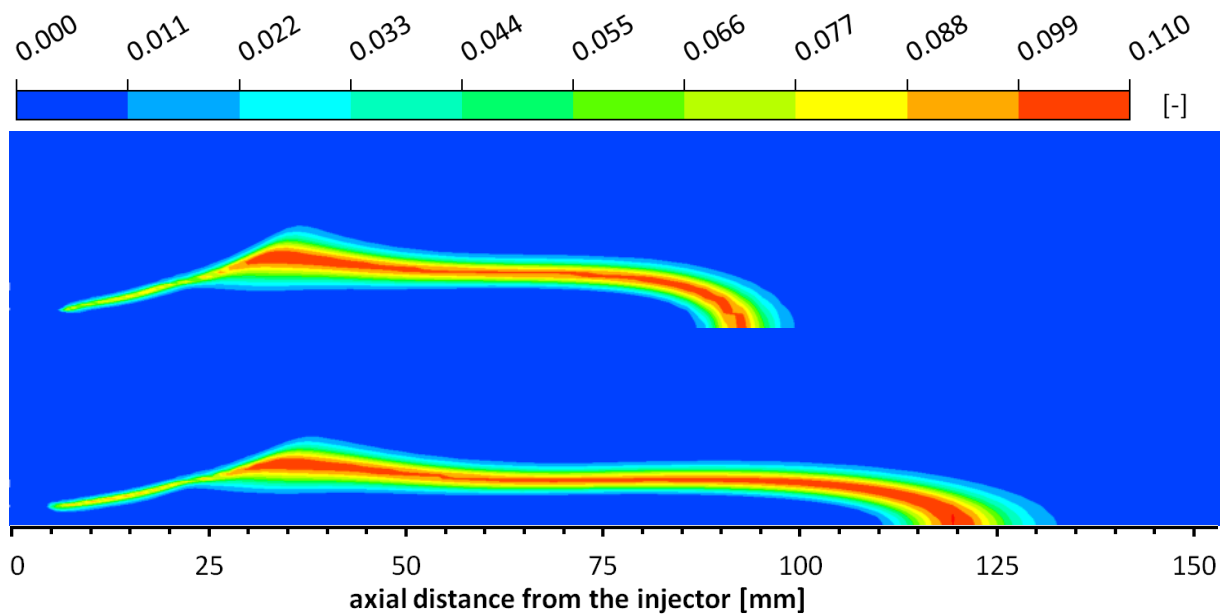


Figure 4.30: *OH mass fraction plots from simulations of the Mascotte single injector test case [37]; above: Jachimowski [47], below: Ó Conaire et al. [69]*

4.4.5 Influence of Turbulence-Chemistry Interaction

Simulations were carried out using the modified mechanism of Jachimowski (Table A.4). The method described in section 3.3.2 is used to tabulate rate constants.

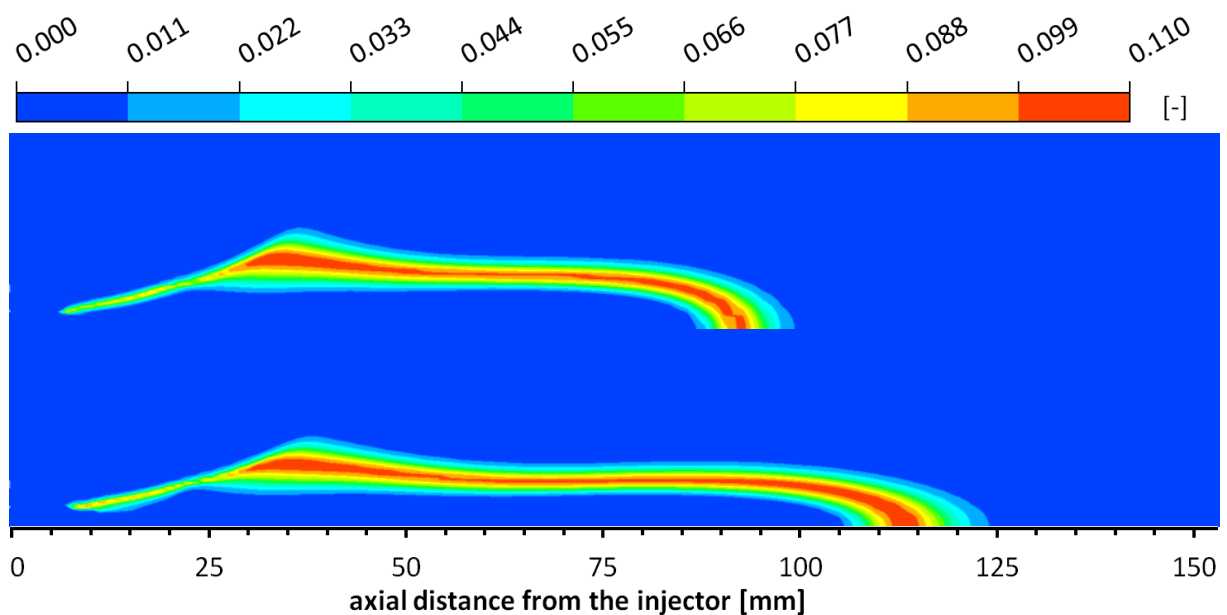


Figure 4.31: *OH mass fraction plots from simulations of the Mascotte single injector test case [37]; above: no PDF, below: T-PDF*

OH mass fraction plots from simulations without turbulence-chemistry interaction on the one hand and assumed PDF of temperature on the other hand are compared in Figure 4.31. The peak value along the axis is further downstream when the temperature PDF is applied. Also, the flame becomes somewhat thicker in the vicinity of the injector, which is not the case in the emission image from the experiment. It should also be noted that the effects observed here can be different when using another reaction mechanism, since the PDF of temperature acts on the rate coefficients.

In simulations with the PDF of composition alone or in conjunction with the PDF of temperature the flame was convected out of the computational domain. Therefore in Figure 4.32 and Figure 4.33 the temperature fluctuation intensities I_T and the sum of species mass fraction variances σ_Y^2 are plotted for the simulation where the PDF of temperatures is used only (i.e. the additional transport equation for the species variance is solved, but not considered for chemical kinetics). The first thing that one notices is that the values are much higher than in the simulations of the flame from Cabra et al. [14]. The reason for that is that the gradients of mass fractions and temperatures are a lot larger here. One could argue that the extremely high values are a consequence of the implementation, where the source terms of the equations (3.57) and (3.59) remain constant over one solver time step. The production term in both equations is independent of the transported variances, while the dissipation term is a function of them. An increase through the production term is not immediately accounted for in the dissipation term, only in the next solver time step for which the source term is recalculated. However, in a simulation that has reached a steady state, this effect is not relevant.

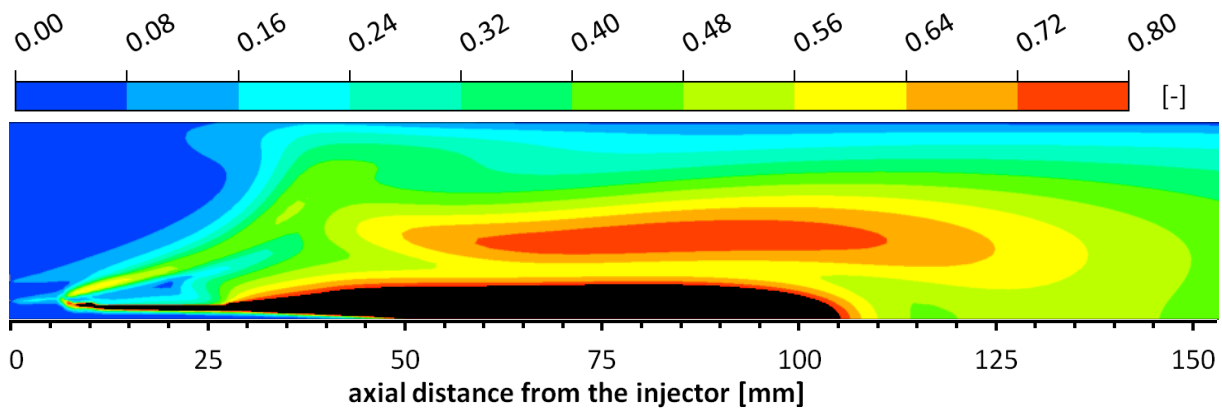


Figure 4.32: I_T plot from the simulation of the Mascotte single injector test case [37] with consideration of the assumed PDF of temperature only

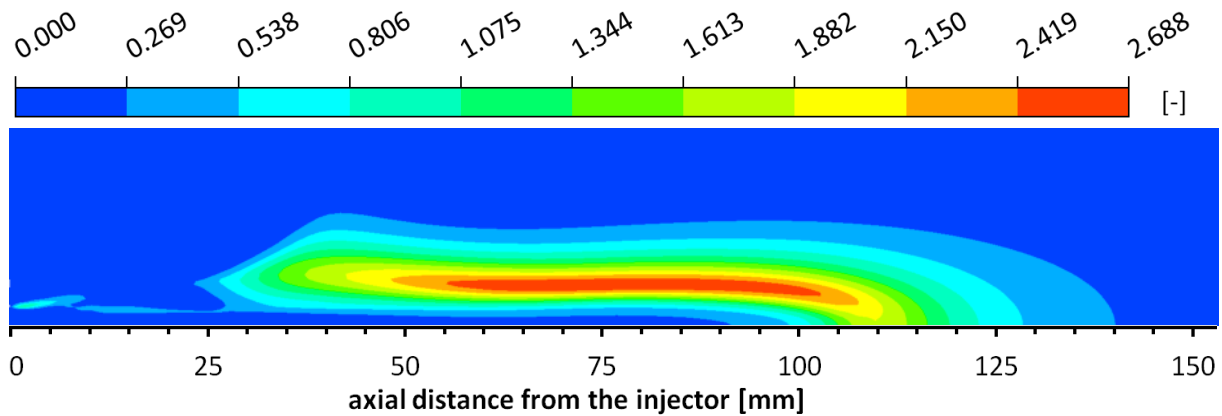


Figure 4.33: σ_y^2 plot from the simulation of the Mascotte single injector test case [37] with consideration of the assumed PDF of temperature only

The fluctuation intensities are only tabulated up to $I_T = 0.8$. Larger values are plotted in black in Figure 4.32. Higher values can cause difficulties in the calculation of the rate constants and furthermore they are also not physically plausible. The maximum value for the sum of species variances is limited according to equation (3.50). For a simulation of 8 species its maximum possible value is 0.875, but it is significantly smaller in most parts of the flame. Consulting Figure 4.33 this would mean that the maximum effect of the assumed PDF of composition would be considered in almost the entire domain. Therefore it is comprehensible that simulations accounting for species fluctuations results in an extinction of the flame.

In summary, it is questionable whether it is necessary or even reasonable to include the assumed PDF of temperature; and applying the assumed PDF of composition is not permitted, because this leads to an extinction not observed in the experiments. Surprisingly, not considering turbulence-chemistry interaction leads to the best reproduction of the experimental data. One has to keep in mind that the assumed PDF approach is just a model to account for the interaction of turbulence and chemistry. It is reasonable to use it for turbulent non-premixed flames at atmospheric pressure (as seen in section 4.3), but it seems not to be qualified for the conditions present in rocket engine flames. The good agreement with experimental data suggests that turbulent mixing of propellants in most parts of the flame is more important than chemical kinetics.

5 Preliminary Studies for the Simulation of Instabilities

5.1 The Hydrodynamic System

Investigations were carried out on a simple test case (from [104]), where a pipe flow arises from an oscillating pressure gradient. It allows comparison of data from numerical simulations with analytical results. The aim is to see how well the connection between pressure and velocity fluctuations is reproduced by the flow solver and to find a guideline for the selection of a proper time step size for the simulation of transient phenomena.

5.1.1 Experimental Data and Theoretical Background

When examining alternating flow in a tube Richardson and Tyler [88] noted that, contrary to expectations, the amplitudes of velocity oscillations are much greater in annuli remote from the center of the tube than at the center itself. Amplitudes reach their maximum in a region near the wall, from where friction causes a rapid drop down to zero velocity. The described near-wall velocity overshoot is now known as *Richardson's annular effect*. The corresponding experiment consisted of an electronic motor that is moving a piston back and forth near one end of the tube.

Sextl [95] could explain this effect by principles of an oscillating laminar flow that is based on common hydrodynamic equations. He assumed to have an incompressible flow that is oscillating harmonically with the angular frequency ω . He could show that the axial velocity u at a distance r from the center of a tube with the inner radius r_0 is:

$$u = \frac{K}{i\omega} \left[1 - \frac{J_0\left(r\sqrt{-i\omega/\nu}\right)}{J_0\left(r_0\sqrt{-i\omega/\nu}\right)} \right] e^{i\omega t} \quad (5.1)$$

K is a constant (for given density and pressure gradient amplitude), J_0 is the Bessel function, ν is the kinematic viscosity and $e^{i\omega t} = \cos \omega t + i \sin \omega t$ with $i = \sqrt{-1}$. To further examine this equation, two series approximations can be used:

$$\text{for small } z < 2: \quad J_0(z) \approx 1 - \frac{z^2}{4} + \frac{z^4}{64} - \dots \quad (5.2)$$

$$\text{for large } z > 2: \quad J_0(z) \approx \sqrt{\frac{2}{\pi z}} \cos\left(z - \frac{\pi}{4}\right)$$

By combining equations (5.1) and (5.2) Sexl could give two series approximations for the velocity. To achieve the form given in equations (5.5) and (5.6) the following dimensionless variables are first defined:

$$r^* = \frac{r}{r_0} \quad \omega^* = \frac{\omega r_0^2}{\nu} \quad u^* = \frac{u}{u_{\max}} \quad (5.3)$$

Here u_{\max} is the velocity in the center of a steady Poiseuille flow with the pressure gradient $-\rho K$ and is defined as:

$$u_{\max} = Kr_0^2/4\nu \quad (5.4)$$

When $\omega^* > 2000$ oscillating flows may become turbulent, therefore the quantity ω^* is sometimes referred to as the kinetic Reynolds number. The equations for velocity now become:

$$\text{for } \omega^* < 4: \quad \frac{u}{u_{\max}} \approx (1 - r^*) \cos \omega t + \frac{\omega^*}{16} (r^{*4} + r^{*2} - 5) \sin \omega t + O(\omega^{*2}) \quad (5.5)$$

$$\text{for } \omega^* > 4: \quad \frac{u}{u_{\max}} = \frac{4}{\omega^*} \left[\sin \omega t - \frac{e^{-B}}{\sqrt{r^*}} \sin(\omega t - B) \right] + O(\omega^{*2}) \quad (5.6)$$

where:

$$B = (1 - r^*) \sqrt{\frac{\omega^*}{2}} \quad (5.7)$$

Averaging equation (5.6) over one cycle (see [104]) leads to:

$$\frac{\overline{u^2}}{K^2/2\omega^2} = 1 - \frac{2}{\sqrt{r^*}} e^{-B} \cos B + \frac{e^{-2B}}{r^*} \quad (5.8)$$

The overshoot occurs where $\cos B + \sin B \approx e^{-B}$, or $B \approx 2.284$, which is shown in Figure 5.1.

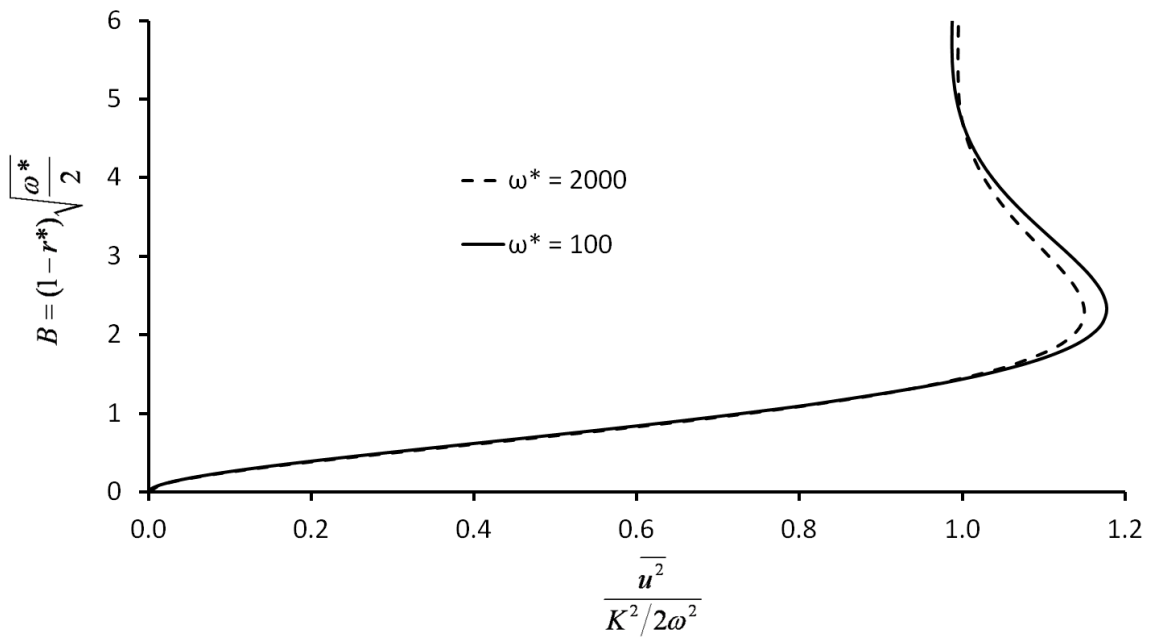


Figure 5.1: The near wall velocity overshoot (Richardson's annular effect)

5.1.2 Set-Up for Numerical Simulations

In his explanation of Richardson's annular effect, Sexl [95] assumed incompressibility. Thus the fluid used in the simulations is air with constant density ("Air at 25 C") from the material library of ANSYS CFX. The computational domain is designed according to the corresponding experiment of Richardson and Tyler [88]. As there is no separate 2D-solver in CFX, the $L = 33$ cm long tube with an inner radius of $r_0 = 3.1$ cm is represented by a quasi-2D grid, according to the recommendation of ANSYS for the axisymmetric case: a 2° wedge with two nodes in circumferential direction and an adiabatic free slip wall at the axis. In order to resolve the near wall velocity overshoot, the grid is designed to have >10 points in the range $0 < B < 2.284$, which resulted in 155 cells in radial direction. The domain is randomly chosen to have 65 cells in axial direction. It is not necessary to pay special attention to the number of cells in axial direction, as the simulation is incompressible.

The Reference Pressure is set to $p_0 = 101325$ Pa. The "Total Energy" option is chosen for heat transfer. No turbulence model is selected (laminar flow). The "High Resolution" option is chosen as advection scheme. The "Second Order Backward Euler" option is set as transient scheme.

As the direction of the flow is alternating between flowing into and flowing out of the domain, the boundary condition at each open end of the tube has to be assigned to be an "Opening". The "Mass and Momentum" option of this type of boundary condition in ANSYS CFX is set to "Opening Pressure and Direction" by default. In this case two different pressures are used for the calculation: total pressure based on the normal component of velocity for inflows and the relative static pressure for outflows. With the option "Static Pressure and Direction" instead, the same pressure is taken, regardless of the direction of the flow.

The piston that was used in the experiment of Richardson and Tyler [88] to generate the oscillating flow in the tube is not modeled in the numerical simulation. Instead the relative pressure is held constant at zero ($p_1 = p_0$) at one end of the tube ($x_1 = 0$ cm) and is alternating ($p_2 = p_0 - \hat{p} \cos \omega t$) at the other end ($x_2 = 33$ cm). As mentioned above, the simulation presented here is incompressible. Therefore the pressure gradient that emerges through the difference in pressure at the two openings is uniform throughout the entire domain.

5.1.3 Results in ANSYS CFX

As the phase shift is not exactly 90° (see Figure 5.2), the simulation needs a certain time to catch up with the analytical solution. From the third cycle on the results do not significantly improve any more.

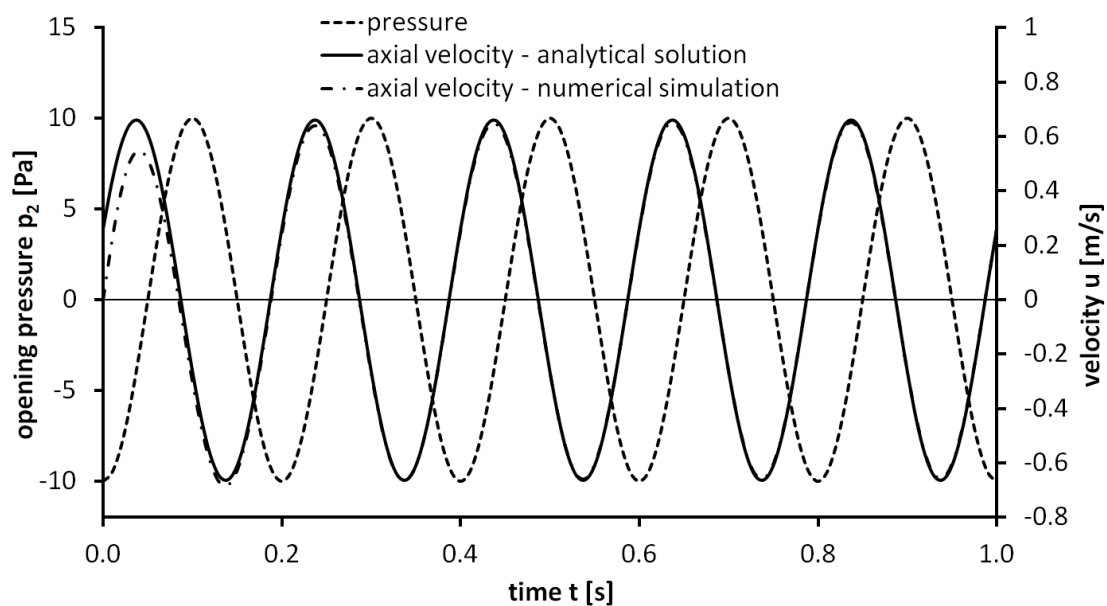


Figure 5.2: Phase shift for $\omega^* = 1950$ and $p_{max} = 10$ Pa at one Opening, with $\Delta t = 0.01s$

The good agreement of results from numerical simulation and analytical solution shows that the connection between pressure and velocity fluctuations is well reproduced. This is to be expected since, as already mentioned in section 2.7, ANSYS CFX is a coupled solver. However, the choice of time step size has to be carefully considered to achieve accurate results (see Figure 5.3).

To obtain the data shown in Figure 5.3 velocities are averaged over one cycle starting at $t = 0.5$ s. Even if the velocities are averaged several cycles later, the results do not improve any more. An improvement can only be achieved by decreasing the time step size in the simulation.

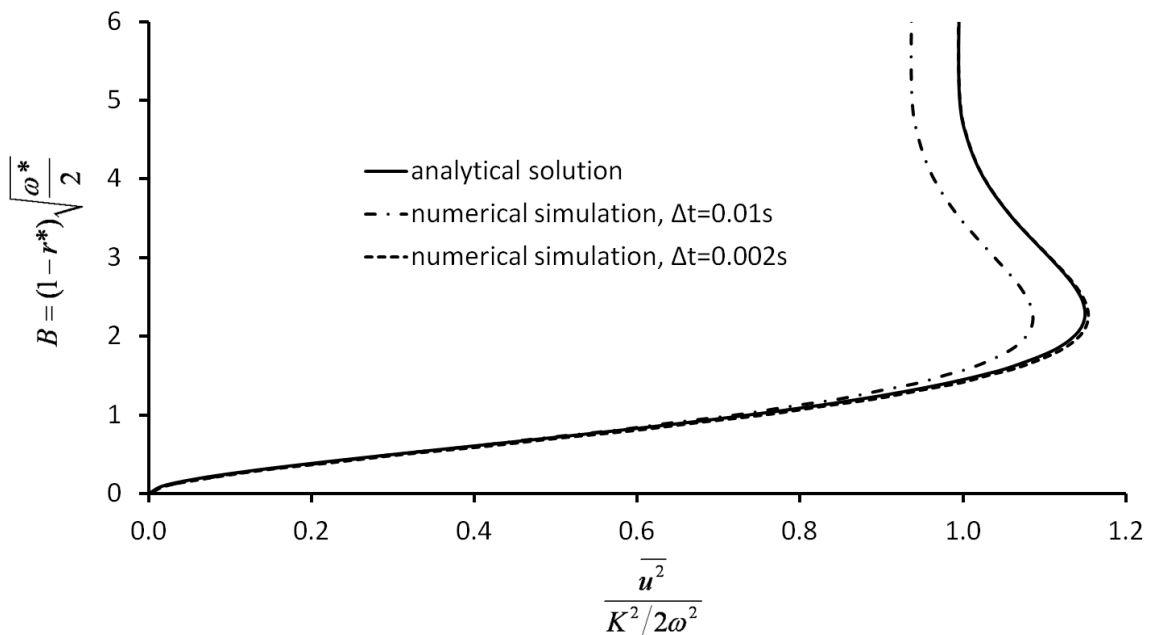


Figure 5.3: Numerical simulation and analytical solution for $\omega^* = 1950$ and $p_{max} = 10\text{Pa}$ at one Opening

A series of calculations are carried out, where the period T , the amplitude of the opening pressure \hat{p} and the time step Δt are changed to see their effect on the results. Furthermore the simulations are also carried out on a shorter domain, where the length of the tube is chosen to be 3.3 cm (while the diameter remains at 6.2 cm, and the number of grid nodes does not change). For all simulations the results are evaluated by comparison with the analytical solution shown in Figure 5.3.

A conclusion that can definitively be drawn is the fact, that results become better for decreasing time steps (as already illustrated in Figure 5.3). But the quality of the results cannot be linked to one decisive factor. In certain simulations even

several hundred time steps per period are not sufficient to achieve a good agreement. The maximum CFL number (or simply Courant number) alone is also an insufficient marker for accuracy. However, good agreement with the analytical values is achieved for all simulations that meet both of the following requirements:

- a) at least 100 time steps per period
- b) a small maximum Courant number (3 or smaller)

These two criteria proved to be suitable for the given test case, but the exact numbers cannot be generalized. A reduction of the time step size by a factor of five shows a significant effect in Figure 5.3 but would barely be noticeable in Figure 5.2. Therefore an assessment of the required time step has to be performed also with respect to the required accuracy. For further calculations it is important to know, that CFX can successfully reproduce the connection between pressure and velocity fluctuations; and that the quality of results has to be evaluated with respect to the number of time steps per period and the CFL number.

5.2 Heat Release and Pressure

A Rijke tube is a vertical tube of length L with two open endings and a heating element placed inside the tube in a distance of $L/4$ from its lower ending. It is named after Rijke [89], who first discovered and described the phenomenon of sound that is produced. Numerical simulations in CFX are performed with the intention to show that CFX can successfully reproduce the interaction of heat release and acoustics.

5.2.1 Set-Up for Numerical Simulation

The set-up of the numerical simulation is not based on the initial experiment of Rijke, but rather on the data given by Hantschk and Vortmeyer [38]: the tube has a length of $L = 3$ m and a radius of $R = 0.05$ m. The domain inside the tube is resolved by a grid of 801 nodes in axial and 21 nodes in radial direction, uniformly distributed in each direction. Similar to section 5.1 a quasi-2D grid is used: a 2° wedge with 2 nodes in circumferential direction. The wall of the tube is set to be an adiabatic wall with "No Slip" option. The thin surface close to the axis is assigned to be an adiabatic wall with "Free Slip" option. The domain is extended at inlet and outlet of the tube in both axial directions by 0.1 m. There

the pressure is assumed to be constant [20]. Since buoyancy is not modeled, the initial axial flow in the tube is not driven by upward moving heated air, but through a pressure difference between the two open ends: the relative static pressure is set to 0.0 Pa at the outlet and 0.5 Pa at the inlet. Inlet and outlet are both "Openings" with the "Static Pressure and Direction" option since in the excited state backflow appears. In both circumferential directions symmetry boundaries are used. One of the two symmetry boundaries contains a gap at $X = 0.75$ m (corresponding to $L/4$ of the tube) in which a wall is inserted. This wall is assigned a constant temperature of 1500 K and serves as heating element. A sketch of this heater is shown in Figure 5.4. It extends over the entire radius but has only one face in axial direction.

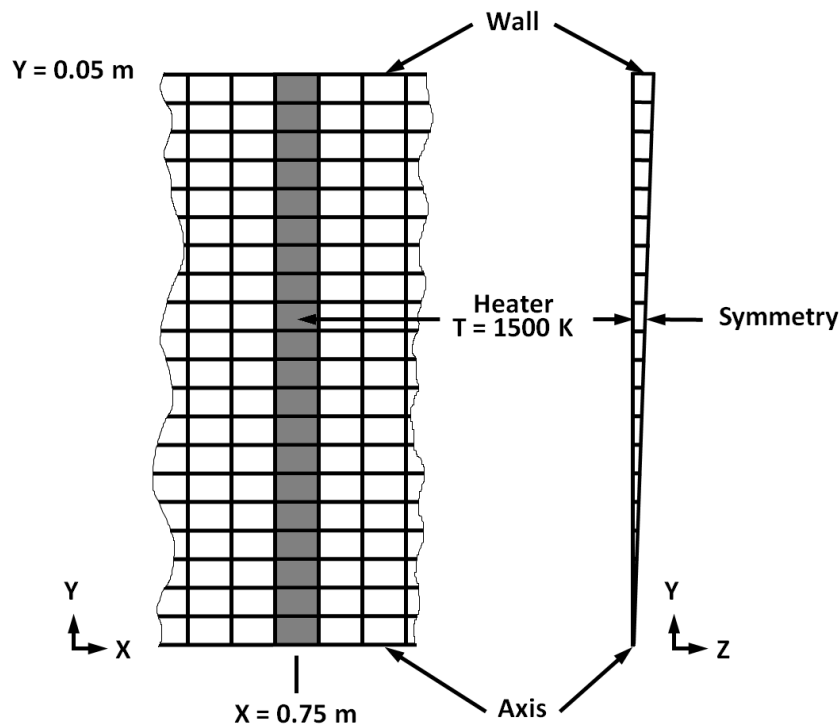


Figure 5.4: Illustration of domain and grid in the Rijke tube at the position of the heater

The reference pressure is set to $p_0 = 1\text{atm}$. The fluid that is applied in the simulations is air as ideal gas. The molar mass ($M = 28.96\text{ g/mol}$), the viscosity ($\mu = 1.831 \times 10^{-5}\text{ kg/m s}$), the specific heat ($c_p = 1004.4\text{ J/kg K}$) and the thermal conductivity ($\lambda = 0.0261\text{ W/m K}$) of the fluid were those of air at $25\text{ }^\circ\text{C}$. The "Total Energy" option has been chosen to model heat transfer. No turbulence model has been selected (laminar flow). The "High Resolution" option has been chosen as advection scheme and the "Second Order Backward Euler" option as transient scheme.

5.2.2 Results in ANSYS CFX

A transient simulation is started from a steady state solution with an additional pressure peak at the position of the heater. This results in an oscillating motion of the fluid. The plot of pressure over time in Figure 5.5 shows that after the initial disturbance pressure oscillations adopt a sinusoidal shape. One period is resolved by roughly 60 time steps (time step size 0.25 ms).

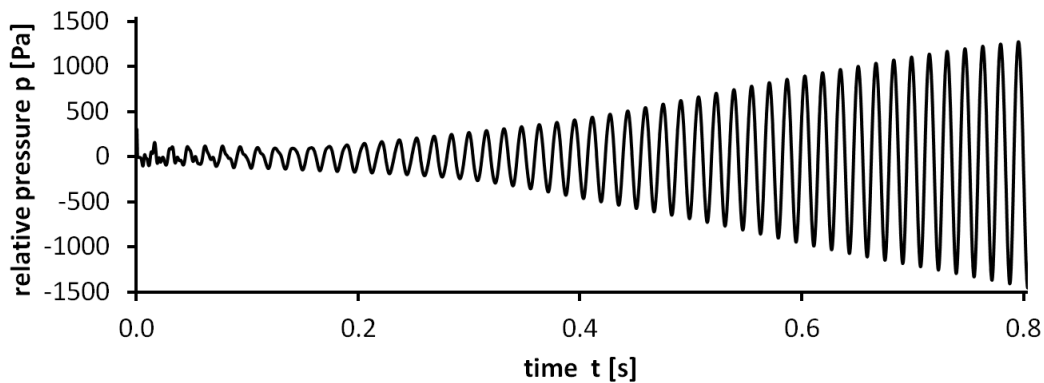


Figure 5.5: Oscillating pressure in the Rijke tube at the position of the heater

Values of pressure and axial velocity are acquired from monitor points at $Y = 0.025$ m at the position of the heater ($X = 0.75$ m). As shown in Figure 5.6 the pressure oscillations lag the velocity oscillations by approximately 90° . While the predominant direction of the flow remains, there is also considerable backflow during each period.

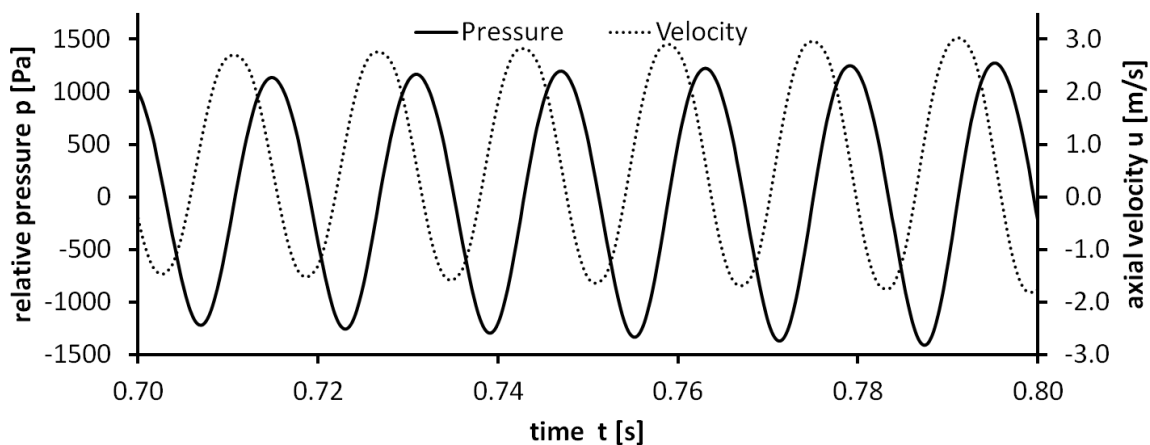


Figure 5.6: Oscillating pressure and velocity in the Rijke tube at the position of the heater

The total heat flux is obtained from summation over all surface elements:

$$\dot{Q} = \sum_i \dot{Q}_i \quad (5.9)$$

where for each surface element i the heat flux transferred to the flow in the adjacent volume element is calculated from:

$$\dot{Q}_i = k \frac{T_{surface} - T_{elementcenter}}{\Delta s} A_{surface} \quad (5.10)$$

Δs is the distance between the center of the surface element and the center of the volume element. The phase shift between oscillating pressure and heat flux is about 40° and is thus in the required range to fulfill the Rayleigh criterion (see [82] and [84]). This explains the growing amplitudes of pressure, velocity and heat flux oscillations.

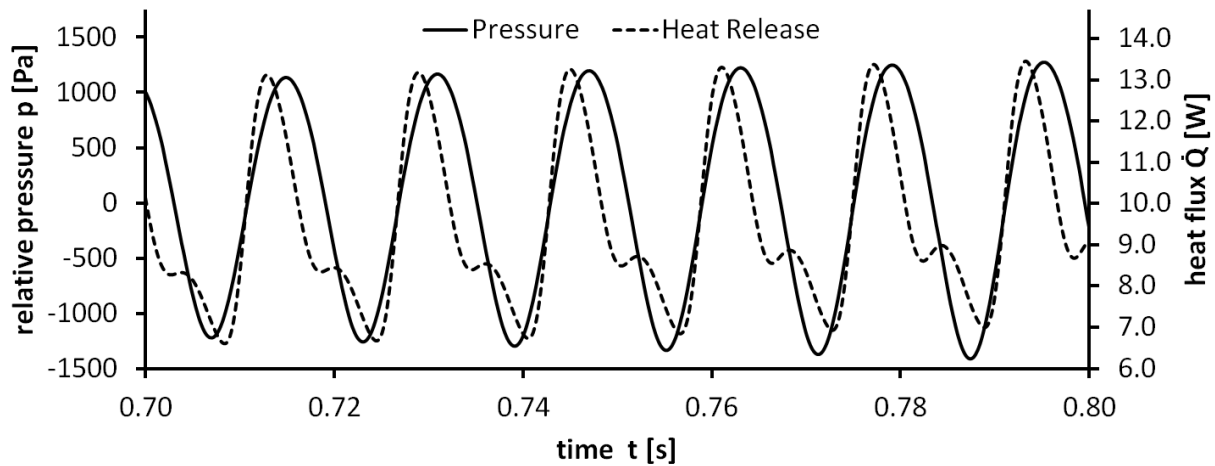


Figure 5.7: Oscillating pressure and heat flux in the Rijke tube at the position of the heater

Backflow at the heater causes nonlinearities on the heat flux, which first show through the appearance of higher harmonics in the heat flux oscillations (see Figure 5.7). Also the formation of a limit cycle can be reproduced (Figure 5.8). At the limit cycle higher harmonics in the pressure oscillations appear as well, which are a consequence of the higher harmonics in the heat flux oscillations. A fast Fourier transform of the heat release in Figure 5.8 delivers the frequency spectrum as shown in Figure 5.9. The amplitudes are scaled relative to the first harmonic of the Rijke tube.

All finding described so far are in agreement with experimental [41] and numerical data [38]. The higher harmonics are however much more distinct in the simulation presented here. This is a consequence of the heater design, which causes

further nonlinearities in the heat flux: As can be seen in Figure 5.4 the distance Δs between the center of the surface element and the center of the volume element is very much dependant on how far away the element is from the axis. Consequently, according to equation (5.10), much more heat is transferred to the flow in the vicinity of the axis than at the confining wall.

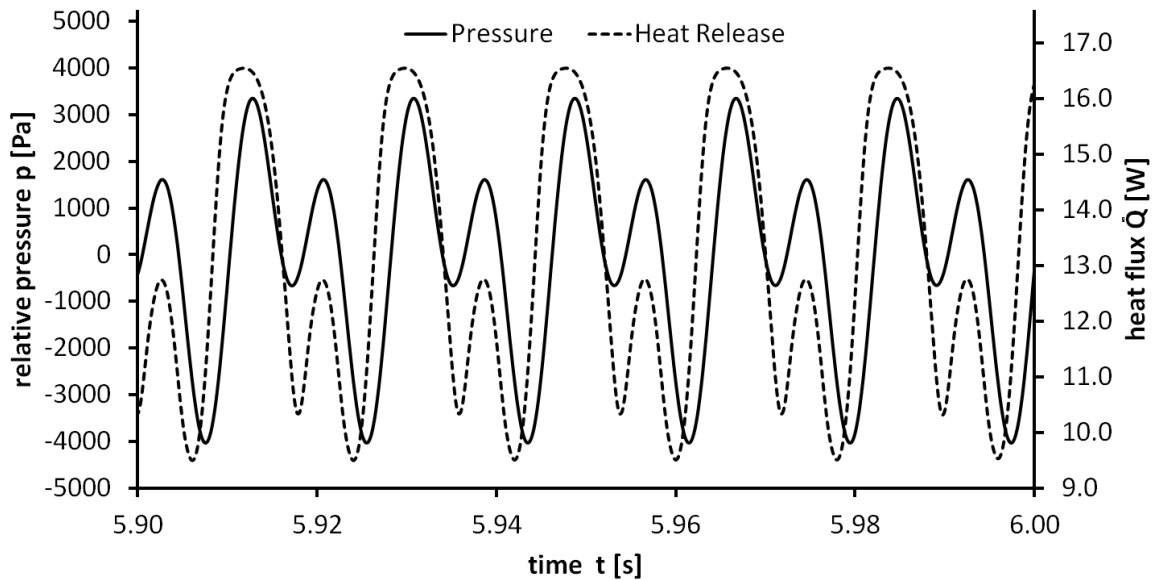


Figure 5.8: Oscillating pressure and heat flux in the Rijke tube at the position of the heater at limit cycle

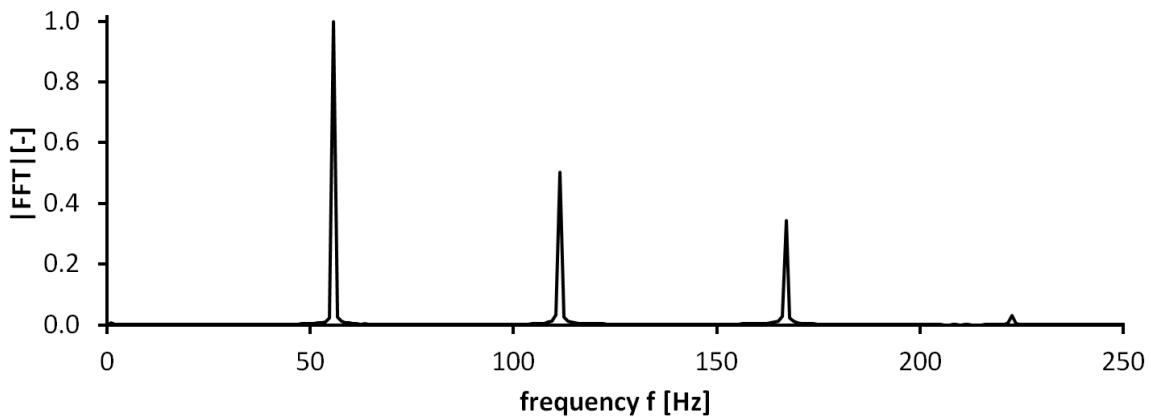


Figure 5.9: FFT gain of the calculated heat release at the limit cycle in Figure 5.9

It can be concluded that the expected characteristics of the Rijke tube are well reproduced in the presented simulation in CFX. Since the velocities in the tube are relatively low in comparison with the speed of sound ($Ma < 0.1$) a simulation with the "Thermal Energy" equation with the "Include Pressure Transient Term" option produces essentially the same results.

5.3 Methods for Simulation of Instabilities

5.3.1 Velocity Excitation

In section 5.1 the alternating pressure at one open end of the domain served as a good method to get an oscillating flow in the pipe. For simulations with incompressible fluid a uniform pressure gradient was achieved in the entire domain. Pressure gradients act on the momentum equations, which in CFX [4] are:

$$\frac{\partial(\rho\mathbf{U})}{\partial t} + \nabla \cdot (\rho\mathbf{U} \otimes \mathbf{U}) = -\nabla p + \nabla \cdot \boldsymbol{\tau} + \mathbf{S}_M \quad (5.11)$$

with \mathbf{S}_M as source terms. Instead of generating a gradient in the pressure field, it is also possible to use the source term to get the fluid in motion:

$$\mathbf{S}_M = -\nabla p \quad (5.12)$$

The results presented in section 5.1 can also be achieved by an alternative set-up. The x-component of the momentum source term is set to:

$$S_{M,x} = -\frac{dp}{dx} \quad (5.13)$$

with (see section 5.1 for reference):

$$\frac{dp}{dx} = \frac{p_2 - p_1}{x_2 - x_1} = -\frac{\hat{p}}{L} \cos \omega t \quad (5.14)$$

With the source term in the momentum equation the motion of the fluid can be manipulated at any place in the domain, also for compressible flow and without directly affecting the pressure field. That is, the influence of velocity fluctuations on the combustion process can be observed separately from the effect of pressure fluctuations.

5.3.2 Velocity and Pressure Excitation

Rey et al. [86] used a simple generic geometry to illustrate modulation techniques. The same set-up is studied here. A flow of air as ideal gas is simulated at a temperature of 300 K and a pressure of 1 bar in a 40 cm long and 25 cm wide domain on a uniform structured mesh ($81 \times 51 \times 2$ nodes). The axial velocity imposed at the inlet is 10 m/s. The first transverse mode of the domain has a frequency of about $f = 700$ Hz. The time step that has been used for all simulations

is 7×10^{-5} s, which corresponds to about 20 time steps per period. The chosen spatial discretization corresponds to 100 nodes per wavelength.

As described in section 5.3.1, a pressure gradient in the source term of the momentum equation can be used to introduce a transverse motion of the fluid. Pressure increases at the walls on the upper and the lower side of the domain when fluid is moving towards them; and decreases when fluid is moving away. The temporal evolutions of both pressure and transverse velocity fluctuations after 350 cycles as shown in Figure 5.10 compare well with the results shown by Rey et al. [86].

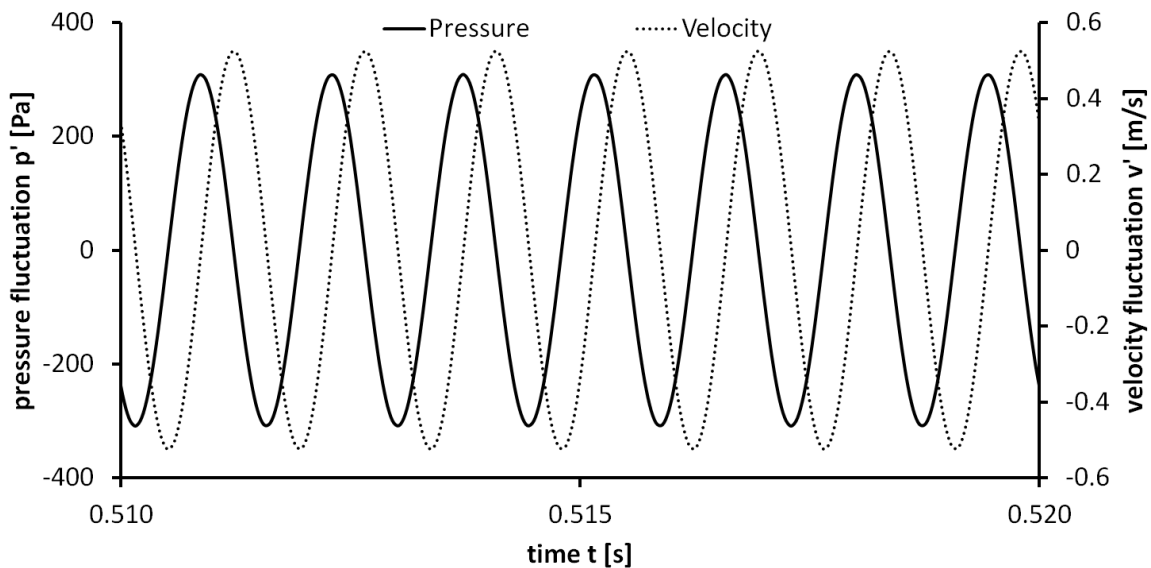


Figure 5.10: Fluctuation of pressure and transverse velocity at $x = 0.20$ m and $y = -0.75$ m

Also the spatial distribution plotted in Figure 5.11 shows good results. Only the first cells close to the inlet and the outlet show different behavior than the rest of the domain. This could be reduced (or even eliminated) by using boundary conditions that change along with the source terms. However, several cycles are necessary at the beginning of the simulation until both, pressure and velocity fluctuations reach their final amplitudes.

As described in section 2.8, ANSYS CFX has a beta feature with which it is possible to have physically non-reflective boundary conditions. This feature can also be used to excite the domain. For this purpose the upper and the lower side of the domain are defined as inlet boundaries instead of walls. When the reflection factor is set to zero, all acoustic waves exit the domain. A velocity excitation with $2u \omega \cos(\omega t)$ is imposed normal to the boundaries, where $u = 0.5$ m/s

(see Rey et al. [86]) and the angular frequency $\omega = 2\pi f$. The same results can be obtained as shown in Figure 5.10 and Figure 5.11. The amplitudes reach their final state at the end of the first cycle already. Since the boundaries are physically non-reflective no feedback processes emerge. Thus with this method the response to the excitation can effectively be obtained.

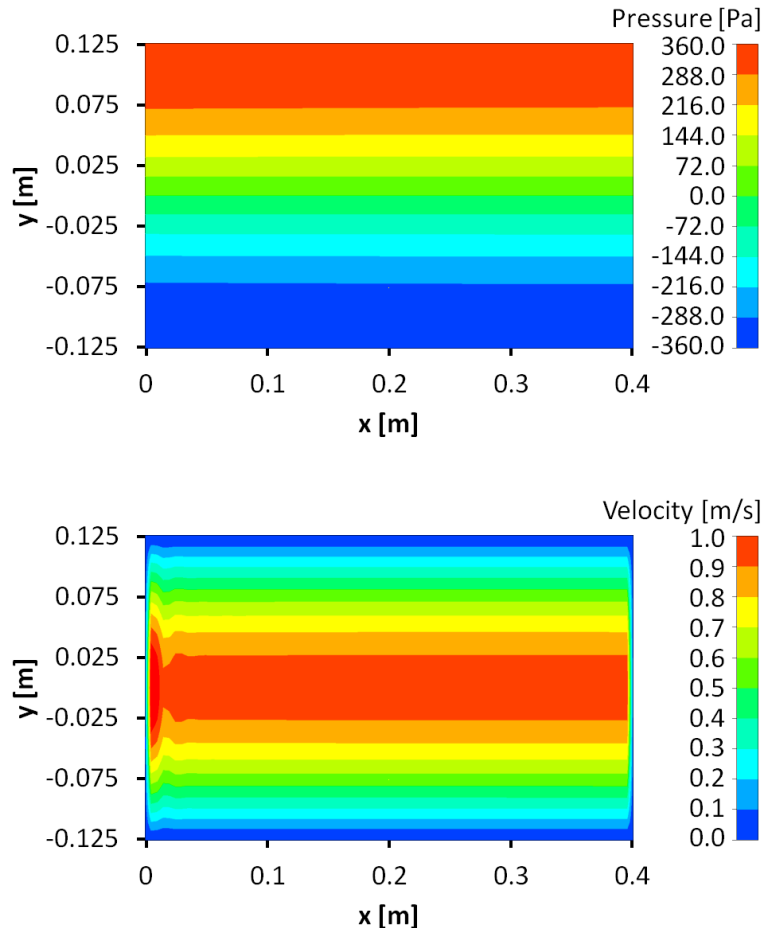


Figure 5.11: Distribution of pressure (above) and velocity (below) in the computational domain

Both excitation methods described in 5.3.2 are able to reproduce matching fields of oscillating pressure and velocity. However, the entire geometry would have to be included in a simulation. The computational effort for a simulation with combustion in a chamber with a large number of injectors would be very high. Therefore it is necessary to limit the scope of the simulation to a single injector and to find a pressure excitation method that requires a reasonable computational effort.

5.3.3 Pressure Excitation

In CFX a reference pressure has to be specified. The solver then takes the difference to the absolute pressure for computations. In the case where relevant changes in pressure are small compared to the absolute pressure, this helps to reduce round-off errors. It was also possible to specify an expression as input for reference pressure. In release 11.0 of ANSYS CFX an expression of the form $p = p_0 + \hat{p} \cos \omega t$ was used to generate an alternating pressure in the entire domain. Simulations showed that it was possible to generate a fluctuating pressure field. However, it was difficult to interpret the obtained results. It would have required detailed insight in solver processes to decide whether this approach was suitable for its desired use. Furthermore, in its later releases ANSYS CFX does not except time dependant expressions as input for reference pressure anymore. Therefore this approach was no longer pursued.

Schmid and Sattelmayer [91] describe a pressure excitation method developed at Lehrstuhl für Thermodynamik, which is applied to CFD simulation of transverse modes on a single injector configuration: For the numerical simulation of an injector, whose diameter is much smaller than the diameter of the combustion chamber, periodic boundaries are used, that are parallel to the main flow. A fluctuating mass source term is applied to all of these boundaries (see Figure 5.12). This source term acts like a fluctuating velocity on the boundary. When it is positive, it adds mass to the domain and causes the pressure to rise. When the source becomes negative, mass is extracted and the pressure in the domain drops. Results obtained from CFD simulations with a single step chemical reaction indicate that the method performs well when applied to rocket engine injectors. The application of this method to CFD simulations with the detailed reaction mechanism is shown in section 6.5.

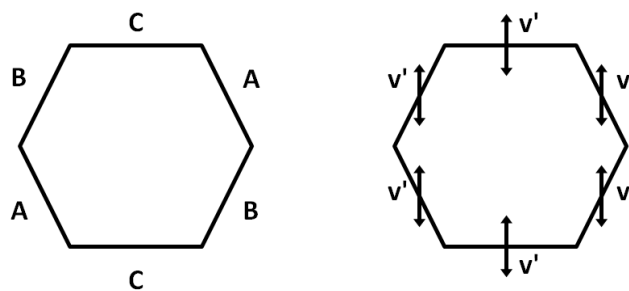


Figure 5.12: Cross section of a 3D computational domain with illustration of the translational periodic boundaries (left) and of the pressure excitation methods (right)

Starting from the same perception (i.e. that the velocity fluctuations cause the pressure fluctuations), another pressure excitation method can be deduced. In this case the boundaries that are parallel to the main flow are defined as adiabatic free slip walls and are subject to displacement. The relative position of these moving walls to their idle position is obtained by integration of the same velocity equation that has been given by Schmid and Sattelmayer [91]. The mesh in the entire domain deforms accordingly. This feature is implemented in CFX [4] and can easily be applied. Simulations on a simple mesh with air as ideal gas show that this excitation method produces the same fluctuating pressures as the method discussed before. The application of moving walls to CFD simulations of the single injector configuration of a rocket engine flame is presented in section 6.5.

The objective for finding a pressure excitation method is to gain knowledge on how pressure fluctuations affect the combustion process. In the present work combustion is calculated in an external routine, which requires temperature and molar concentrations as input parameters. Temperature is read directly from CFX. Molar concentrations are calculated from mass fractions and density. Pressure does not have a direct impact on the combustion process. However, a changing pressure within the flow solver would of course affect temperature and density. Instead of generating a fluctuating pressure within the flow solver, it can also be simulated in the external routine. In this case the routine reads T_{CFX} , ρ_{CFX} and p_{CFX} from the flow solver. Additionally an excitation pressure p_{exc} is given, which varies with time. Since thermoacoustic fluctuations are considered to be isentropic the following equations apply:

$$T_{exc} = T_{CFX} \left(\frac{p_{CFX} + p_{exc}}{p_{CFX}} \right)^{\frac{\gamma-1}{\gamma}} \quad (5.15)$$

$$\rho_{exc} = \rho_{CFX} \left(\frac{p_{CFX} + p_{exc}}{p_{CFX}} \right)^{\frac{1}{\gamma}} \quad (5.16)$$

Equations (5.15) and (5.16) can be used to calculate T_{exc} and ρ_{exc} as new input parameters for the chemical kinetics solver. The isentropic exponent γ can be calculated from specific heat capacities.

6 Simulation of Instabilities on a Rocket Engine Flame

6.1 Experimental Data

Experiments were carried out at DLR Lampoldshausen with a model rocket combustion chamber called BKD, with the intention to investigate interactions between combustion and acoustics [35]. The combustion chamber has a cylindrical form with an inner diameter of 80 mm. Hydrogen and oxygen are injected through 42 coaxial injectors at temperatures around 120 K. All pressures in the experiments were above the critical pressure of oxygen, which is also the case for real H₂-O₂ rocket engines. At several operating points experiments showed self-excited thermoacoustic oscillations of the first transverse mode at about 10000 Hz.

Table 6.1: *Operating conditions for combustion chamber BKD with injector head L42 [35]*

operating point		3	7
chamber pressure [bar]		80.46	61.47
total mass flow [kg/s]	H ₂	0.96	0.95
	O ₂	5.74	3.81
temperature [K]	H ₂	112.75	
	O ₂	126.10	
pressure amplitude [bar]	ca.	10	4

CFD simulations were carried out with data available from operating points 3 and 7 (as listed in Table 6.1). Results from these simulations are presented in the following sections.

6.2 Basic Numerical Setup

The setup is very similar to the simulations of the Mascotte test case [37], which is described in section 4.4: For the multi-component flow 7 transport equations (for H_2 , O_2 , H , O , OH , HO_2 and H_2O_2) and one constraint equation (for H_2O) are solved. Only O_2 is treated as a real gas, all other species are ideal gases and ideal mixing applies. For the simulations in ANSYS CFX external routines are used to calculate the combustion process with detailed chemistry. Simulations are carried out with the upwind option as advection scheme and the first order backward Euler option as transient scheme.

Using detailed chemistry for the calculation of combustion processes is very time consuming. Therefore it is not feasible to include an entire combustion chamber in the simulation. The computational domain is hence limited to a region around the flame from one injector only. Mass flow inlets for H_2 and O_2 are placed at the tip of the coaxial injector. The mass flow rates for one injector are taken to be 1/42 of the total mass flow rates. The domain extends roughly up to the end of the cylindrical part of the chamber, where a pressure-outlet is replacing the nozzle.

Numerical simulations in chapter 4 were run with as well as without a model considering turbulence-chemistry interaction. When compared to data of the lifted flame at ambient pressure (see section 4.3) this model performed well. For simulations at high pressures (section 4.4) the turbulence-chemistry interaction model was not able to produce reasonable results: Its application either resulted in an extinction of the flame (assumed PDF of composition) or had no considerable effect on the flame (assumed PDF of temperature). Simulations without the model showed good agreement with experimental data. Thus for simulation of an L42 flame turbulence-chemistry interaction is not considered.

To get information about the heat released from chemical bonds, for each species the source term in the species transport equation is multiplied by its standard enthalpy of formation. At each node the sum of these products gives the volumetric heat release:

$$\dot{Q}_v = \sum_s^{N_s} S_s h_{f,s}^0 \quad (6.1)$$

For each species s the source term for the transport equation is calculated in the external routine according to equation (3.64). The integration of the volumetric heat release \dot{Q}_v over the entire domain gives the global heat release \dot{Q} .

6.3 Simulation without Excitation

A quasi-2D domain was used in order to get a basic idea of the flame shape and to assess problems that might occur during numerical simulations. The domain is closed off in radial direction by an adiabatic wall with “Free Slip” option. The distance of this wall from the axis is chosen to be $R_1 = 6.172$ mm. A circle constructed with this radius corresponds to 1/42 of the cross-section area of the combustion chamber. In circumferential direction the domain has symmetry boundary conditions.

In a first step a simulation of the cold flow was carried out, so that only H_2 and O_2 were present in the entire domain. Temperatures in the cold flow (around 120 K) are too small for auto-ignition. For ignition the external routine was used. Here the temperature read from CFX serves as an input for the calculation of chemical kinetics. In a small region, in the mixing layer of H_2 and O_2 close to the injector, this input parameter was replaced by a value of 1500 K. The source terms that are thus calculated and given back to CFX cause an increase in temperature within CFX. The rise in temperature would now cause a high rise in pressure. This peak pressure then would ultimately cause the simulation to crash. In order to circumvent this problem, the external routine is also used for overwriting the relative pressure with a value of 0 Pa. This simulation is carried out, until the flame has travelled through the entire domain and reaches the outlet. The thus achieved result serves now as a good initial solution from which a steady state solution can be calculated.

The assessment of grid size and time step size is aiming at two targets: On the one hand the simulation has to accurately reproduce the flame shape. On the other hand computational cost has to be kept low in order to get results in a reasonable amount of time. The target value for the time step size is 2×10^{-6} s. For a frequency of 10000 Hz, which occurs in the experiments, this corresponds to 50 time steps per period. The most important region of the grid is the shear layer between the inflows of H_2 and O_2 , since this is where the flame is. In case of a grid refinement it is also important to pay attention to the Courant number (which is defined as: $Courant = u \Delta t / \Delta x$). The Courant number is not relevant for stability in CFX, but can have an influence on accuracy. A finer grid could therefore require smaller time steps as well.

Another point to consider is that flow and combustion are calculated separately. Through this operator splitting method an error is incorporated that scales with

the time step size (see section 3.4). Simulations with different time steps can give information whether the error through operator splitting is sufficiently small.

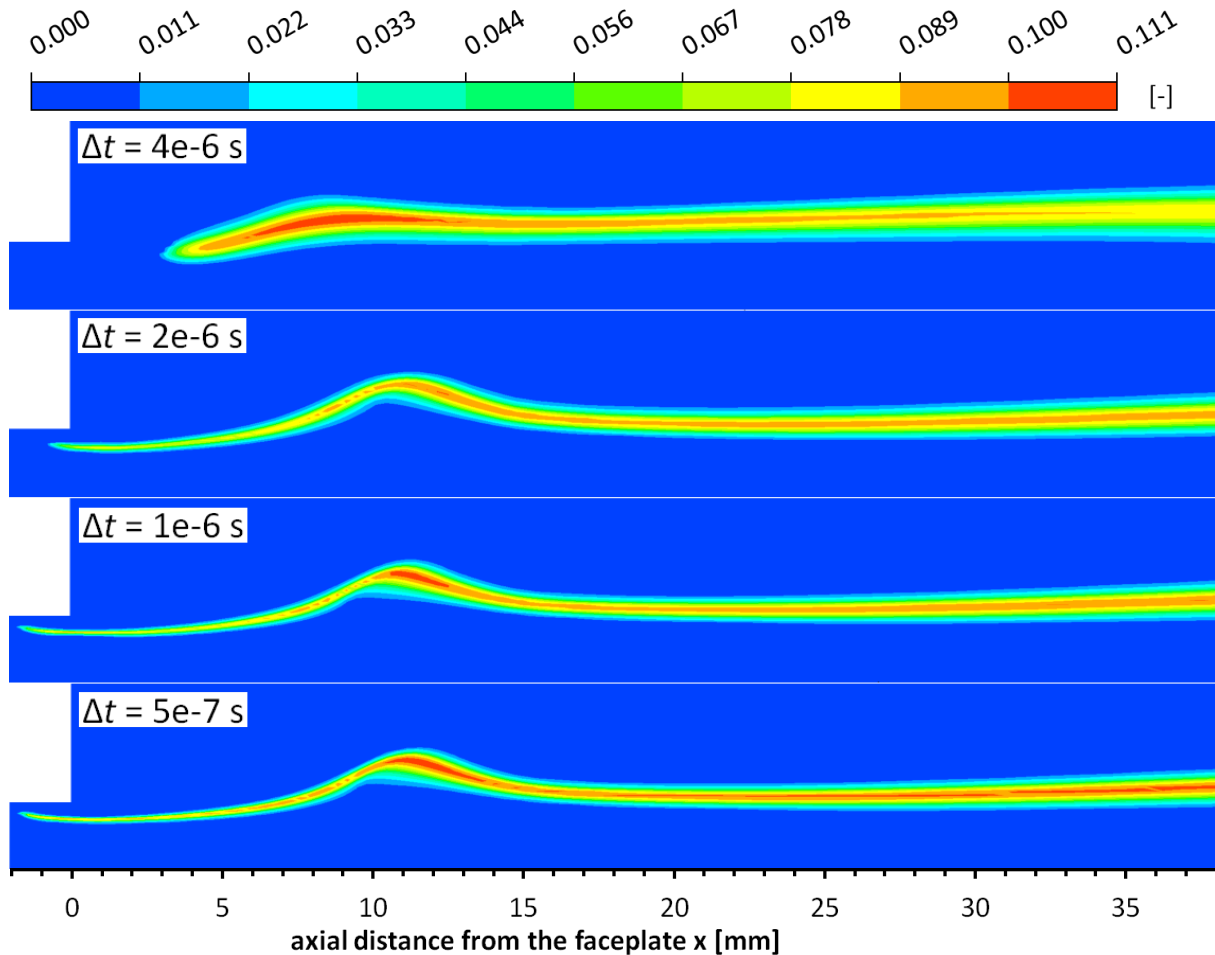


Figure 6.1: *OH mass fraction plots from simulations of OP7 of a single L42 flame on a 2D grid*

Simulations with several grids were used and time step sizes were varied. Results suggest that the shear layer has to be resolved with at least 6 nodes in radial direction and the Courant number has to be below 3 in the region. The final quasi-2D grid has 19264 nodes (with 2 nodes in circumferential direction). It is clustered close to the injector ($\Delta x = 0.2$ mm) and is relatively coarse towards the outlet. With a time step size of 2×10^{-6} s the tip of the flame is kept within the recess. A time step of 1×10^{-6} s brings the flame closer to the injector (0.4 mm instead of 1.4 mm) as can be seen in Figure 6.1 and in Figure 6.2. Further reduction of the time step does not have any noticeable impact on the solution. Even for a finer grid ($\Delta x = 0.1$ mm) and smaller time steps ($\Delta t = 1 \times 10^{-7}$ s) the flame is not directly attached to the injector.

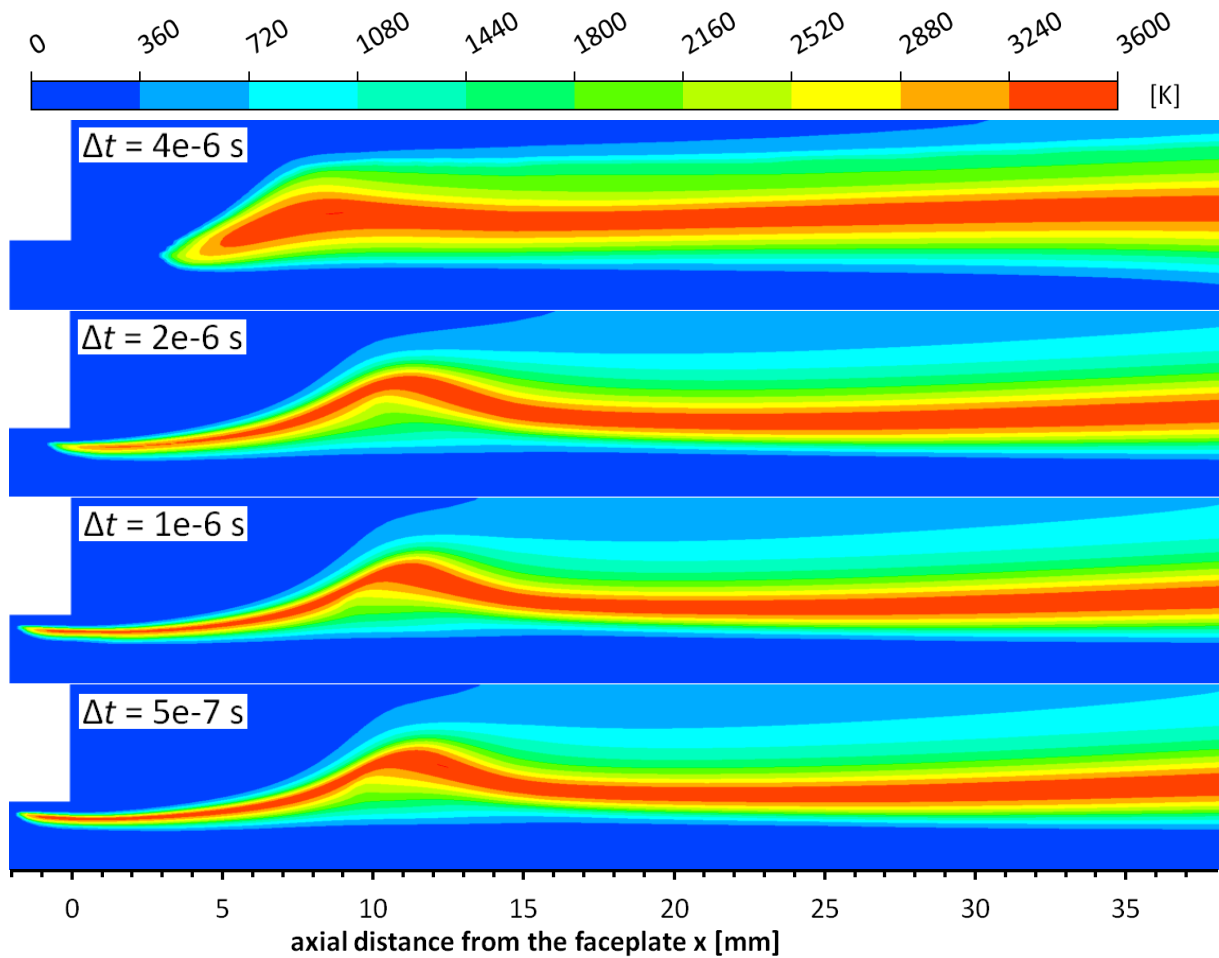


Figure 6.2: Temperature plots from simulations of OP7 of an L42 flame on a 2D grid

For the assessment of grid and time step size the conditions from operating point 7 are used. However, results for operating point 3 are extracted from simulations on the same grid and with the same time step size. For both operating points simulations are conducted with $\Delta t = 5 \times 10^{-7}$. OH mass fraction plots and temperature plots from these simulations are shown in Figure 6.3 and Figure 6.4, respectively.

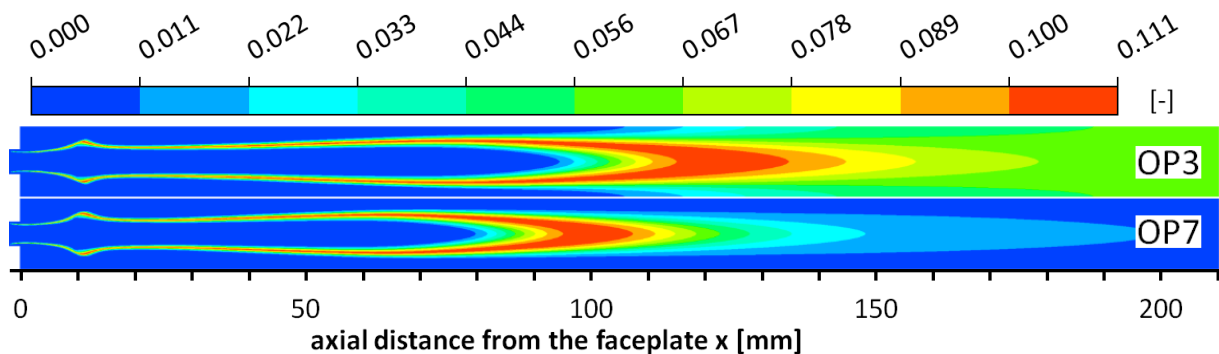


Figure 6.3: OH mass fraction plots from simulations of OP3 and OP7

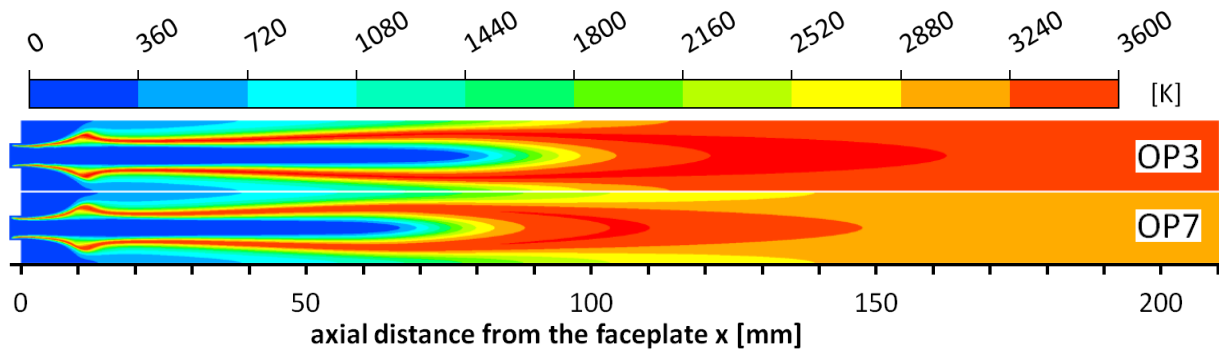


Figure 6.4: Temperature plots from simulations of OP3 and OP7 with

Since the aim of this work is to investigate the response of heat release to acoustic excitation, it is important to know where heat is released within the domain. Figure 6.5 shows the volumetric heat release in the vicinity of the injector. Figure 6.6 shows how heat release is distributed over the domain. On the vertical axis \dot{Q}_x denotes the integration of \dot{Q}_v from the inlet up to an axial distance x from the faceplate; the integration of \dot{Q}_v over the entire domain (from inlet to outlet) gives \dot{Q} .

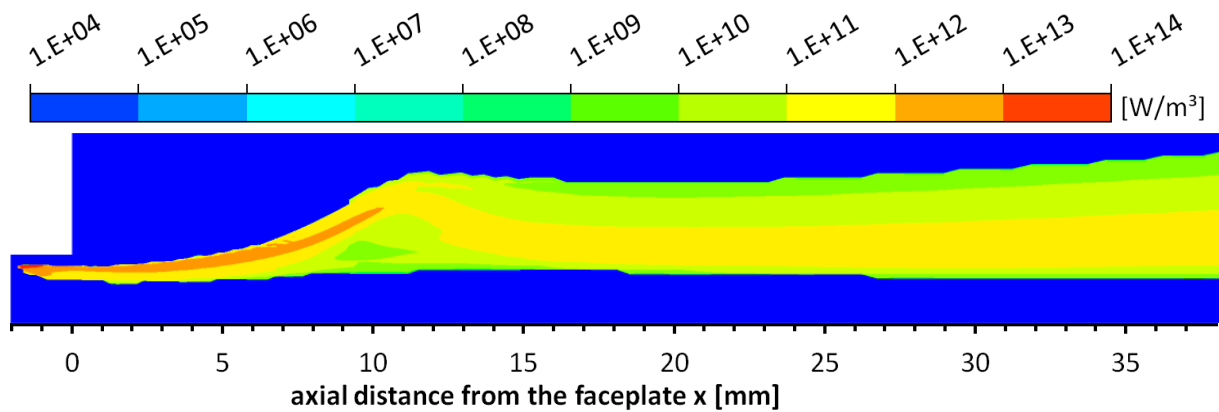


Figure 6.5: Plot of volumetric heat release from simulation of OP7 of the L42 flame

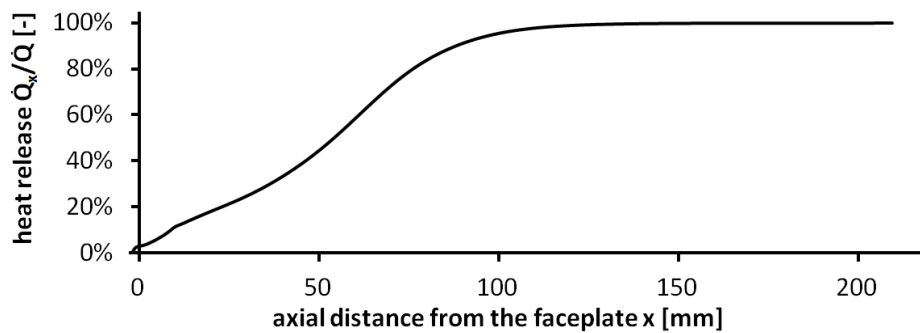


Figure 6.6: Distribution of heat release along the axis from simulation of OP7 of the L42 flame

The heat release is clearly at its maximum at the tip of the flame (Figure 6.5). However, this is only a small percentage of the total heat released in the domain, as shown in Figure 6.6. This figure also shows, that in the non-excited state, most of the heat is released in the first half of the domain.

Some further considerations on the phenomenology of the non-excited flame are accompanied by the next two figures. The streamline plot shows that the cold core of the O_2 stream has only a velocity component in axial direction. The injected oxygen has a very high density and is relatively slow. Since the flame is not attached to the injector, there is a small amount of oxygen that penetrates the annular hydrogen jet (see Figure 6.7). The hydrogen stream that flows through the annulus of the injector has a relatively high velocity but a low density. The co-flow is bent away from the axis in front of the bulge of the flame as can be seen in Figure 6.8. The streamlines show that a recirculation zone is formed close to the faceplate. Temperatures in this zone are around 260 K to 290 K. The composition of the fluid there is roughly as follows: $Y_{H_2} \approx 0.76$, $Y_{H_2O} \approx 0.15$ and $Y_{O_2} \approx 0.08$.

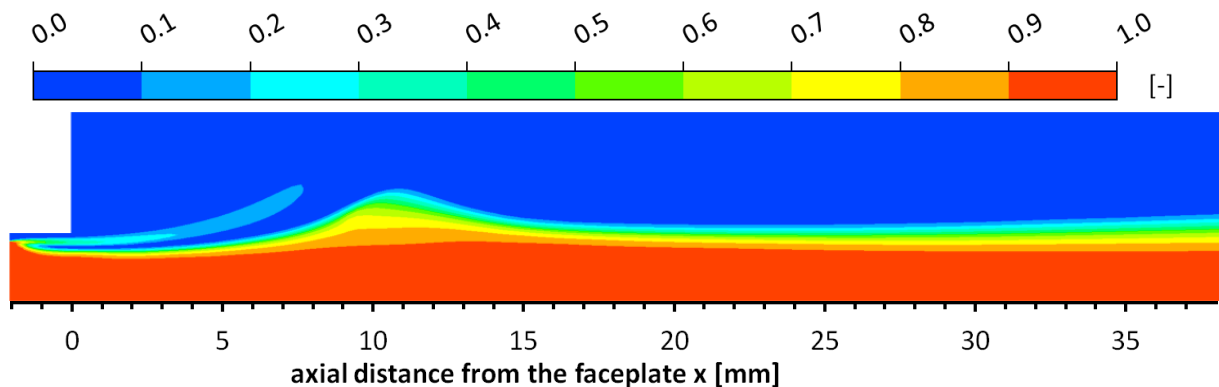


Figure 6.7: O_2 mass fraction plot from simulation of OP7 of an L42 flame on a quasi-2D grid

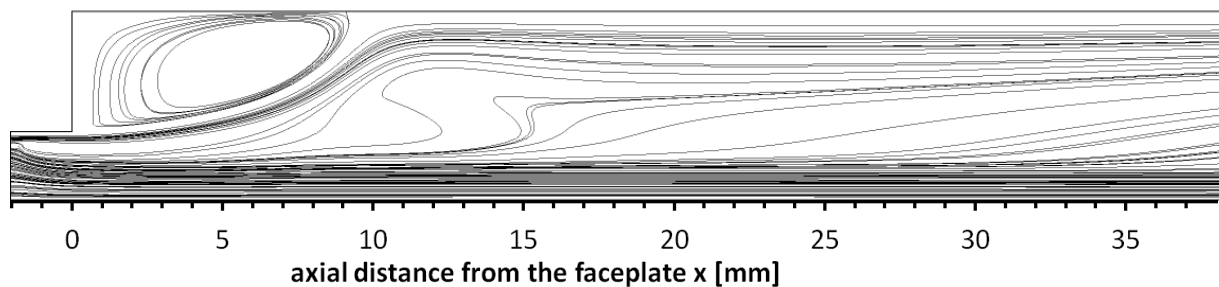


Figure 6.8: Streamlines from simulation of OP7 of an L42 flame on a quasi-2D grid

3D simulations are conducted based upon the findings from the 2D simulations. The three dimensional domain has a hexagonal cross-section. Its cross-section area is equivalent to the cross-section area of the entire combustion chamber divided by 42 (the number of injectors). The generation of the 3D grid was strongly influenced by the form of the final 2D grid. The two grids have exactly the same spacing in axial direction. In the 3D case the grid is designed as an O-grid in the vicinity of the axis. It has about the same number of nodes in radial direction as the 2D grid in this region. In the region away from the axis the grid spacing in radial direction has the same number of nodes and almost exactly the same grid spacing. In circumferential direction the 3D grid is resolved with 72 nodes in the outer region, which corresponds to one grid node every 5° . The final three-dimensional grid has 637531 nodes.

For simulations without excitation, the six boundaries on the lateral sides of the domain are free-slip walls. The ignition procedure is the same as introduced before. A transient simulation is run until a steady state is reached, as indicated by various monitor points in the domain. Results on the 3D grid resemble the results on the 2D grid presented above and serve as an initial solution for simulations with excitation. In order to reach a state that can be considered to be steady, it is necessary to have about 3500 iterations with a time step size of 2×10^{-6} s. The required computational time sums up to about 30 days on 16 cores (on one machine with 64GB memory and two Intel Xeon E5-2660 processors, each with 8 cores at 2.20GHz and no hyperthreading). A time step size of 1×10^{-6} s would require almost twice these resources.

6.4 Velocity Excitation

The domain for simulations with velocity excitation is represented by the previously described 3D grid with hexagonal cross section. The six boundaries parallel to the main flow are now defined as translational periodic interfaces. Flow leaving the domain through one of these boundaries is entering at the same time through the opposing boundary. In simulations without excitation there should be no flow through the interfaces, so that in this case these boundaries are equivalent to the previously used free-slip walls. Velocity fluctuations are then achieved through the use of a source term in the momentum equation as described above (see section 5.3.1). For the specification of this source term it is helpful to visualize the transverse mode that is to be simulated. Figure 6.9 illustrates the T1 mode in a cylinder based on the pressure field.

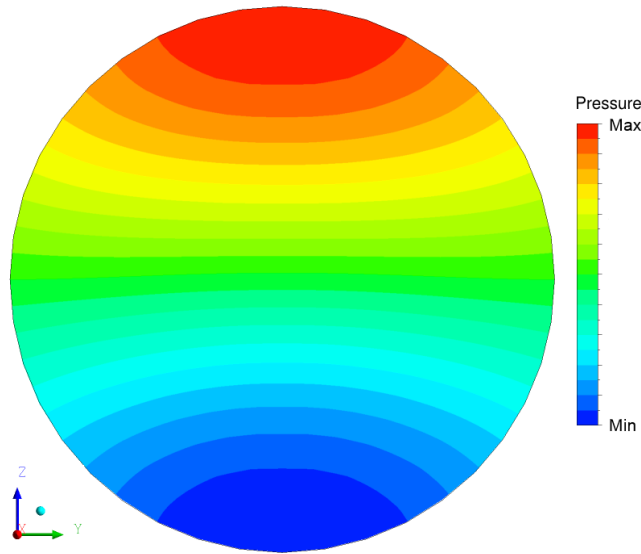


Figure 6.9: Pressure field for the first transverse mode in a cylindrical chamber

In the considered instant the pressure is at its maximum on the top and its minimum at the bottom. The momentum equation in CFX as stated before in equation (2.2) is:

$$\frac{\partial(\rho\mathbf{U})}{\partial t} + \nabla \cdot (\rho\mathbf{U} \otimes \mathbf{U}) = -\nabla p + \nabla \cdot \boldsymbol{\tau} + \mathbf{S}_M \quad (6.2)$$

A look at this equation reveals that, through the first term on the right hand side, the pressure gradient would cause a vertical motion of the fluid within the cylinder. In the simulation of a flame from a single injector there is no pressure gradient present. Instead one component which is at right angles to the mean flow (in this case the z -component) of the source term in equation (6.2) is used to simulate the transverse motion of the fluid within the domain. The source term is set as:

$$S_{M,z} = -\frac{dp}{dz} \quad (6.3)$$

The pressure profile is assumed to be approximately linear in z -direction. In a combustion chamber of diameter D , an injector in the middle of the cylinder would experience a pressure gradient in the order of:

$$\frac{dp}{dz} \approx \frac{2\hat{p}}{D} \cos \omega t \quad (6.4)$$

which is how the source term is specified in the simulation. The value of \hat{p} is taken to be 4 bar. This is the value that has been measured in the experiment at

operating point 7 (see Table 6.1). The source does not act on the flow within the recess, so it is only active for regions with $x > 0$.

A look on the left hand side of equation (6.2) reveals that the magnitude of velocity fluctuations that is caused by the source term depends on density. The motion of the fluids is therefore not uniform. The oxygen core with a density of about 950 kg/m^3 experiences only little deviations from its idle position. In contrast the burnt mixture, with densities slightly above 2 kg/m^3 , shows a strong vertical movement. In the vicinity of the injector this behavior causes a better mixing of the reactants, so that the flame length is shortened as shown in Figure 6.10. Data for the excited state is evaluated at an instant where the flame is at its idle position.

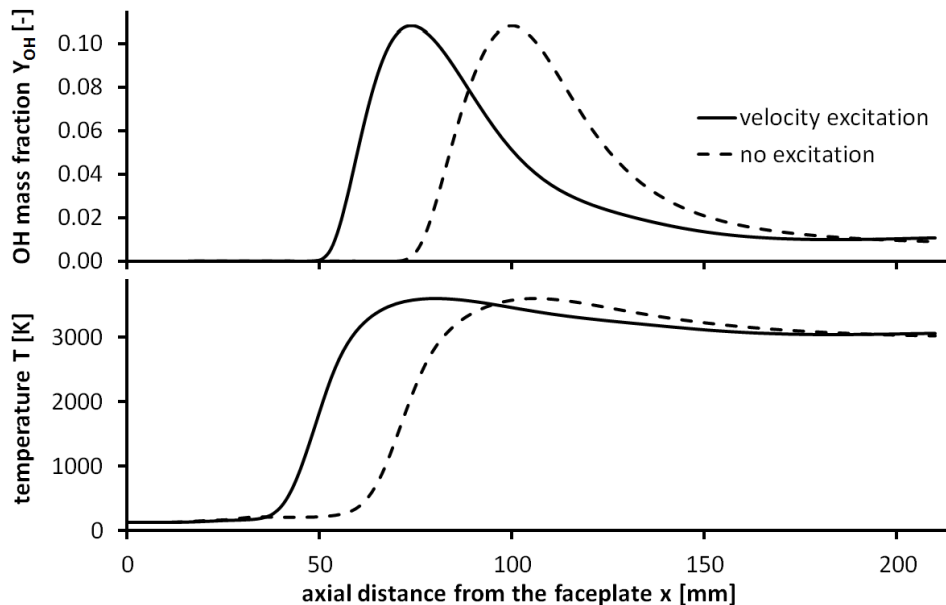


Figure 6.10: Distribution of temperature and OH mass fraction along the axis of an L42 flame with and without velocity excitation

Results from the simulation with velocity excitation are shown in Figure 6.11. The displayed velocity is recorded at the outlet on the axis. On the secondary vertical axis the instantaneous heat release \dot{Q} is associated with the average value \bar{Q} . The graph clearly shows that the global heat release responds with exactly the double frequency of the velocity excitation. The same effect has already been observed by Schmid and Sattelmayer [91], who explained this with the symmetric form of the flame. The heat release is roughly at its maximum when the transverse velocity is at its extreme value; and it is at its minimum when the transverse velocity is zero.

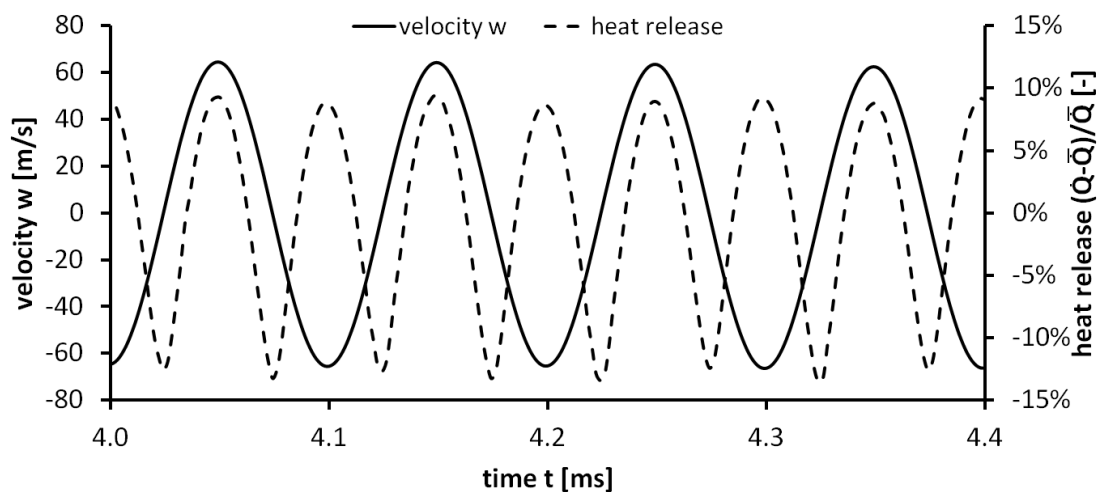


Figure 6.11: Fluctuation of global heat release over time as response to velocity excitation

The conclusion that can be drawn from this finding is the same as constituted by Zellhuber et al. [107]: In experiments a strong signal at the double frequency of the T1 mode can be expected, but it is unlikely that there is a direct coupling between velocity and heat release. The deduction would certainly be the same for operating point 3 and at a smaller time step size (2×10^{-6} s in this simulation). Therefore, especially considering the high computational costs of simulations on the 3D domain, no further calculations are carried out with the velocity excitation method.

6.5 Pressure Excitation

Three different pressure excitation methods were described in 5.3.3. Each of the three is applied to the L42 flame that was presented so far. Results are presented in three separate subsections. Conclusions are summarized in section 6.5.4.

6.5.1 Mass Source and Sink Terms on Boundaries

When source or sink terms are applied to the continuity equation on the boundaries of the domain, as already described in section 5.3.3, a displacement of the fluid relative to the centerline is introduced. This motion is either inwards for source terms or outwards for sink terms. In this case there is no flow in or out of the domain along periodic boundaries that are parallel to the X-axis. Therefore these boundaries can be also taken to be free slip walls. In this case there are two

symmetry planes that can be used to reduce the size of the domain, so that only $\frac{1}{4}$ of the previously used domain is needed. In fact, to reduce the computational cost further, even the quasi 2D grid is sufficient to produce the required results. Which is what is presented in the following. The mass source term is implemented on the boundary as suggested by Schmid and Sattelmayer [91]:

$$\frac{\dot{m}'}{A} = v' \bar{\rho} = \frac{\hat{p}}{c} \cos(\omega t) |\sin(-ky) \bar{n}_y| \quad (6.5)$$

In this equation c is the speed of sound and $k = \omega/c$ is the wave number. The pressure fluctuation that this continuity source term is aiming to achieve in the entire domain is also specified at the outlet boundary:

$$p_{out} = \hat{p} \sin(\omega t) \quad (6.6)$$

Within the domain the local speed of sound varies in a wide range. Therefore an averaged value is taken from the simulation without excitation. Volume weighted averaging over the entire domain gives $c \approx 1634 \frac{m}{s}$.

When a source term is applied in the continuity equation then secondary sources appear in all other equations as well [3]. For the calculation of these secondary source terms on the boundary CFX has to know composition, temperature, turbulence data and velocity components of the fluid mass flux. When the mass source term is negative (sink term) the solver uses local values of the flow for the mass leaving the domain. For a positive source term additional information is required that has to be specified in CFX Pre along with the mass source term. For the specification of these variables it is also possible to use the local values of the flow in the required instant. For simulations presented in this subsection this has been the case for all variables except the species mass fractions.

Several options were considered for the specification of the composition on the boundary. The first was to use the local values, as for all other quantities. In simulations with single step chemistry also using $Y_{H_2O} = 1.0$ on the boundary worked very well, since H_2O is the product of the reaction. Another option was to use $Y_{H_2} = 1.0$ since in the considered experiments the combustion chamber BKD is operated with hydrogen in excess, great part of which flows along the boundary to the outlet. One further consideration was to use an inert species, which in contrast to H_2O and H_2 is not accounted for in the reaction scheme. Amplitude and phase shift of the heat release response to pressure excitation differ considerably from case to case.

In simulations with single chemical reaction there may be only products present at the boundary that is used for excitation. In simulations with detailed chemistry in contrast the fluid at the same boundary is composed of up to eight species that are all involved in a system of forward and backward reactions according to the equations introduced in chapter 3. In a non-excited state, as described in section 6.3, for each species production or consumption due to chemical kinetics are in equilibrium with transport processes in the flow solver according to equation (2.25). A change in pressure due to excitation entails a change in density and temperature, which are both input parameters to the chemical kinetics solver. Through the change in the source term there is a shift in the described equilibrium which implies changes in composition and heat release. But mass that is removed through the sink terms on the boundary is no longer accounted for in the calculation of heat release. Mass that is introduced in the domain through the source terms on the boundary impairs the calculation of heat release in a similar way.

The consequence of using $Y_{H_2O} = 1.0$ is illustrated in Figure 6.12. Fluctuating heat release is related to the value from the steady state solution, which should be the mean during excitation. Even though the flame appears to remain within the domain, the mean value of heat release is smaller than expected. Results from further simulation show that the higher the excitation amplitude is, the more the mean deviates from its supposed value. This is apparently an effect of dissociation reactions, since this effect does not occur in simulations with single step reactions.

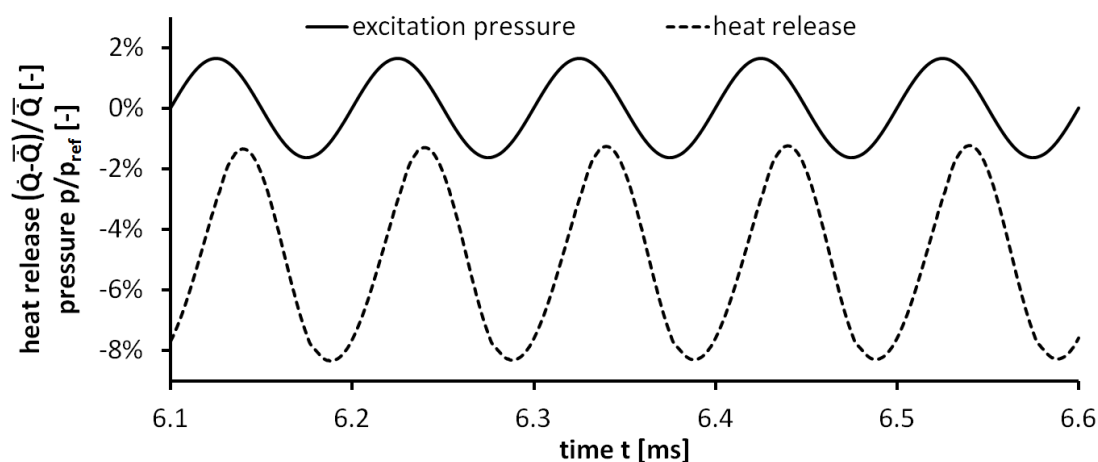


Figure 6.12: Outlet pressure and heat release from excitation with mass source terms on boundaries

Figure 6.13 shows some further data from the simulation with $Y_{H_2O} = 1.0$. Here as well as in Figure 6.12 the pressure amplitude is 1 bar. For a reference pressure of 61.47 bar (i.e. chamber pressure) this corresponds to about 1.63 %. For Figure 6.13 pressures are averaged at numerous locations ($\Delta x = 0.5$ mm) orthogonal to the X-axis. At each location their values are recorded over one period so that their amplitudes and phase offsets can be compared to each other. The pressure amplitude is at its nominal value at the outlet (at $x = 210$ mm). Phase offsets are specified relative to the nominal phase at the outlet. Since fluid composition and properties change a lot on the way from inlet to outlet, the local speed of sound changes accordingly. Thus depending on the axial location pressure waves propagate with different velocities from the excitation boundary towards the axis. Therefore it is consistent that also phase and amplitude of the fluctuating pressure in the domain are varying along the axis when mass source terms on the boundaries are used for excitation.

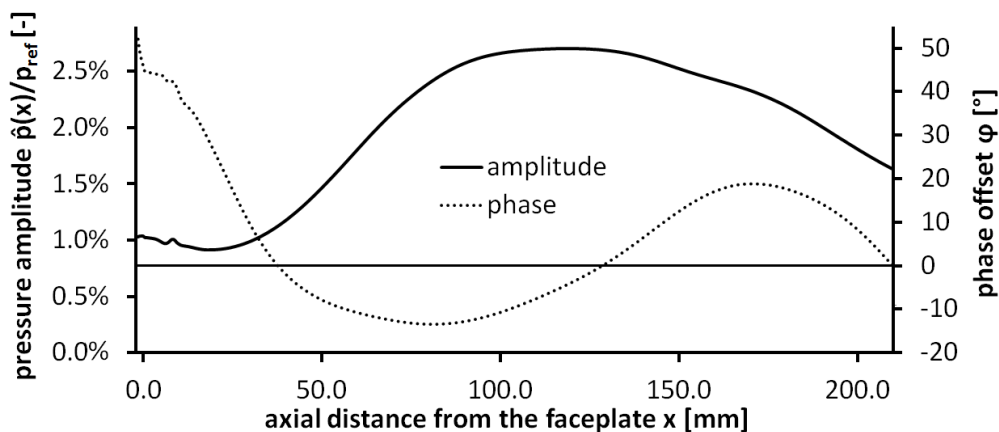


Figure 6.13: Pressure amplitudes and phase offsets resulting from fluctuating mass source terms on boundaries

In order to reduce the effect shown in Figure 6.13 it would be possible to include the local speed of sound in the calculation of the mass source terms on the boundary. However, it is not certain if the acoustic mode would be correctly reproduced. More fundamental experimental research is required to gain knowledge on the exact appearance of acoustic modes in rocket combustion chambers. Then it would be possible to excite the computational domain appropriately. But the main problem with this excitation method (when detailed chemistry is applied) is that the exact heat release response cannot be determined as it is dependent on the specified composition on the boundary.

6.5.2 Moving Wall

To circumvent the difficulty of specifying the composition on the boundary, as already described in section 5.3.3, a moving wall can be used to excite the domain. No mass is removed or added on the boundary and the heat release can be correctly determined. However, one additional information is required, namely a value for density. The equation for the position of the wall at a given instant in time is given relative to its idle position y_0 as:

$$y_{wall} = y_0 \left[\exp\left(-\frac{\hat{p}}{c^2 \bar{\rho}} \sin(\omega t)\right) - 1 \right] \quad (6.7)$$

Values of density within the domain vary to a large extent. However, for each simulation there is just one density that can be used as input to equation (6.7). Therefore its value is obtained from the results of the respective simulation without excitation through volume weighted averaging over the entire computational domain. The thus acquired average density is $\bar{\rho} \approx 15 \text{ kg/m}^3$ for OP3 and $\bar{\rho} \approx 10 \text{ kg/m}^3$ for OP7. Figure 6.14 shows the excitation pressure and the heat release response for OP7 with a pressure amplitude of 1 bar at a frequency of 10 kHz. Here (in contrast to the results shown in Figure 6.12) the mean value of heat release during excitation agrees with the value of heat release from the simulation without excitation. Fluctuations of heat release lag the pressure fluctuations by approximately 22° (by 46° at OP3).

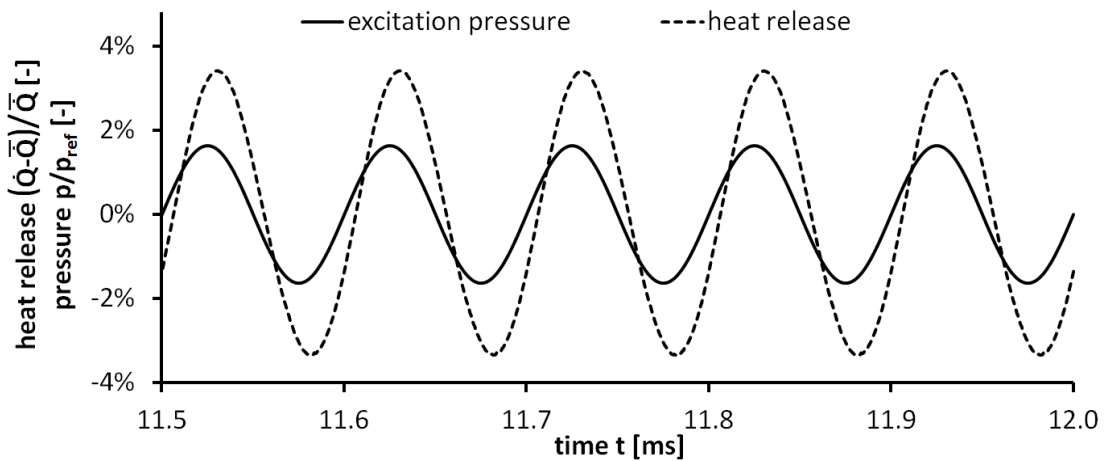


Figure 6.14: Outlet pressure and heat release from excitation with a moving wall at OP7

Putnam and Dennis [82] have noticed that flame-driven oscillations require:

$$\int_0^T \dot{Q}' p' dt > 0 \quad (6.8)$$

This inequality corresponds to the postulate that driving is considered to occur, when the phase shift between heat release and pressure fluctuations is in the range between -90° and $+90^\circ$. Since this integral is based on Lord Rayleigh's hypothesis for flame-driven oscillations [84] the integral is referred to as Rayleigh integral. In Figure 6.15 the Rayleigh integral is given along the axis as $RI(x)$. Heat release is first integrated in space over a plane orthogonal to the X-axis. The fluctuating part of heat release is multiplied with the fluctuating pressure and then integrated over one period to give $RI(x)$. Values greater than zero indicate regions in the flame which contribute to its driving capability, as in this case energy is added to the fluctuations.

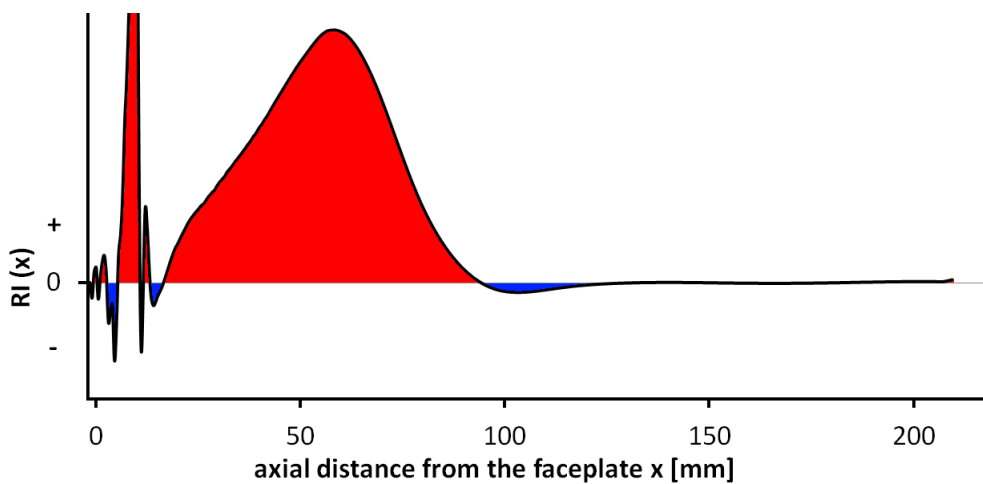


Figure 6.15: Rayleigh-Integral along the axis from simulation of OP7 resulting from excitation with moving wall (at 1 bar and 10000 Hz)

The vicinity of the injector is characterized by closely spaced deflections in both, positive and negative direction. There is a huge amplitude at around $x \approx 10$ mm, which is roughly the place where the bulge in the flame can be observed (see figures in section 3.3). The red field in the range from $x \approx 15$ mm to $x \approx 95$ mm is the most relevant region for the amplification or preservation of acoustic fluctuations. Damping regions (marked blue) are comparably small.

Figure 6.16 is generated in the same way as Figure 6.13. Pressure fluctuations have their nominal form, i.e. values of amplitude and phase offset at the outlet (at $x = 0.21$ m). The range of pressure amplitudes and phase shifts along the axis is even larger than in simulations with mass source terms on boundaries. Varying pressure amplitudes and phase offsets along the axis result in pressure gradients in axial direction, which on their part result in fluctuating axial velocities. It is therefore difficult to separate the influence of pressure fluctuations from other factors that have an effect on heat release fluctuations. Therefore this method is

also not capable to evaluate the direct influence that pressure fluctuations have on heat release fluctuations.

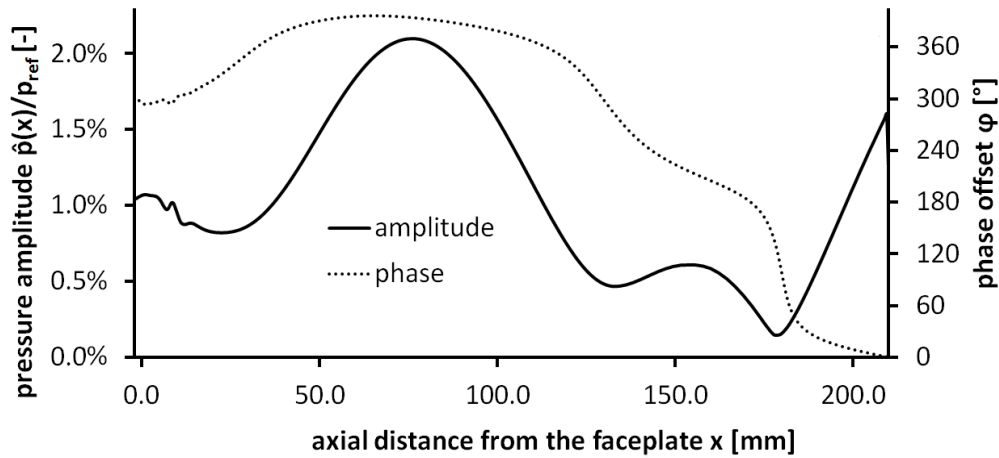


Figure 6.16: Pressure amplitudes and phase offsets resulting from excitation with a moving wall

6.5.3 Fluctuating Pressure as Input to Chemical Kinetics

The third option described in section 5.3.3 is to use no excitation within the flow solver, but to change the input to the chemical kinetics solver. An isentropic process is assumed and pressure change is translated to change in temperature and concentrations according to equations (5.15) and (5.16). For most parts of the flame $\gamma = 1.2$ would be a good approximation. To be more accurate the isentropic exponent γ is determined from the quotient of specific heat capacities, which on their part are read from CFX. The effect of this third excitation method is shown in Figure 6.17. In the corresponding simulation the amplitude of excitation pressure is 1 bar.

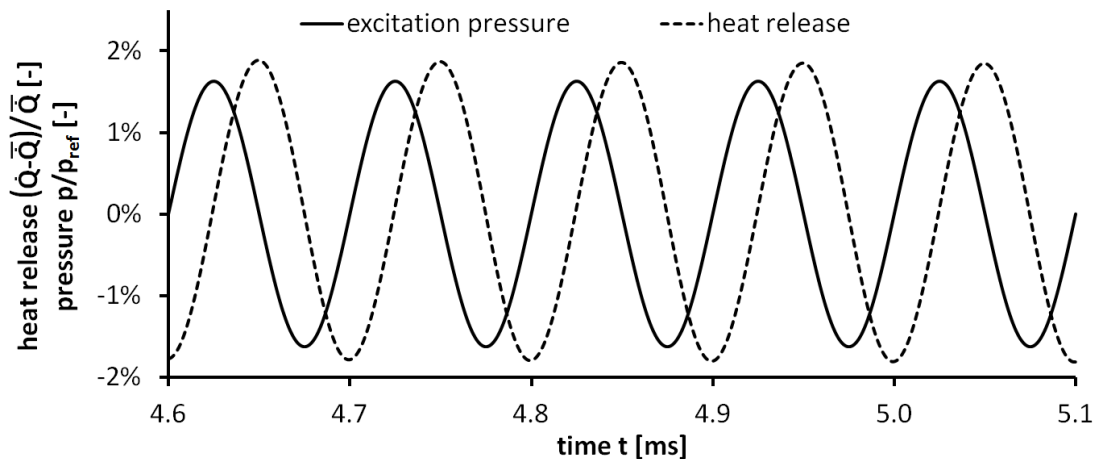


Figure 6.17: Fluctuating pressure and heat release from excitation in external routine

With this excitation method the flow in CFX is only influenced through the source terms in the species transport equations. Changing these source terms in the external routine introduces a change in composition and thereby of course also causes pressure fluctuations within the flow solver. However, these pressure fluctuations are small compared to the excitation pressure (around 5 %) so that the zero pressure outlet boundary that is used is still acceptable. Also radial and axial velocity fluctuations remain small in size. The response in heat release can therefore be ascribed almost exclusively to uniform pressure fluctuations.

In Figure 6.17 the phase shift between excitation pressure and global heat release is very close to 90° . This is not always the case when heat release is investigated at specific locations along the X-axis. In Figure 6.18 the Rayleigh-Integral $RI(x)$ is shown, which is generated in the same way as for Figure 6.15. The scale on the vertical axis is here also the same as in Figure 6.15 to illustrate that the predicted driving capability is smaller than in the previous subsection. The phase offset between excitation pressure and local heat release fluctuations is close to 90° . Red and blue areas are almost similar in size.

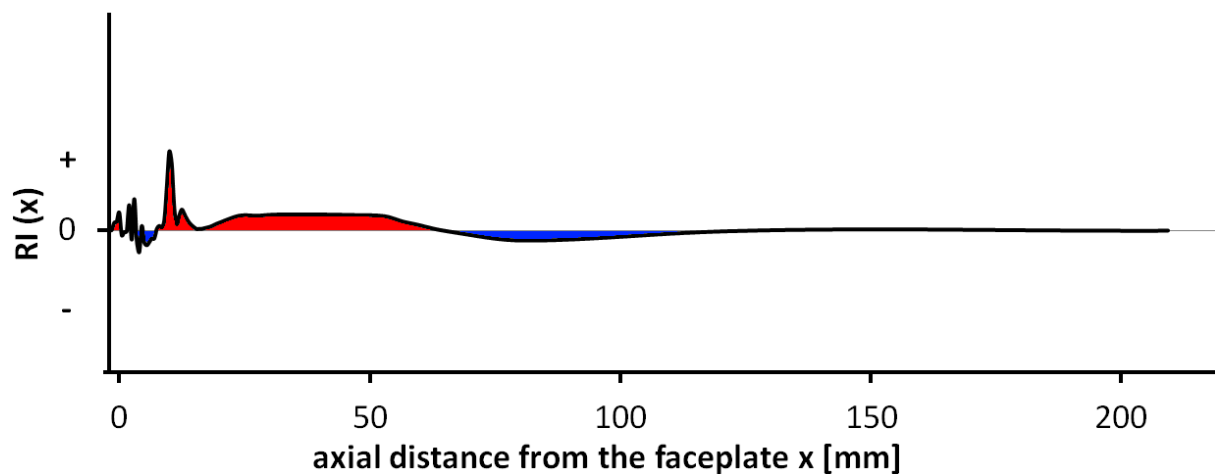


Figure 6.18: Rayleigh-Integral along the axis from simulation of OP7 with excitation (1 bar, 10000 Hz)

Figure 6.18 shows, that even though the pressure excitation is in phase everywhere in the domain, the response in heat release is not. The reason for this is that composition and densities of all constant volume reactors differ considerably in the entire domain. Thus the delay in the response to excitation differs accordingly. Furthermore during excitation the behavior of a constant volume reactor also depends on the behavior of other upstream constant volume reactors. Depending on their performance the convected composition has an additional fluctuation.

In Figure 6.18 there is a larger amplitude at around $x = 10$ mm. This is exactly the place where the bulge in the flame can be observed (see figures in section 6.3). After the first third ($x > 65$ mm) the Rayleigh Integral is negative or close to zero ($x > 135$ mm). Multiple simulations carried out at different frequencies, amplitudes and operating points show similar outcomes. Results from these simulations are also used to plot the phase shift between global heat release fluctuations and excitation pressure as a function of excitation frequency in Figure 6.19.

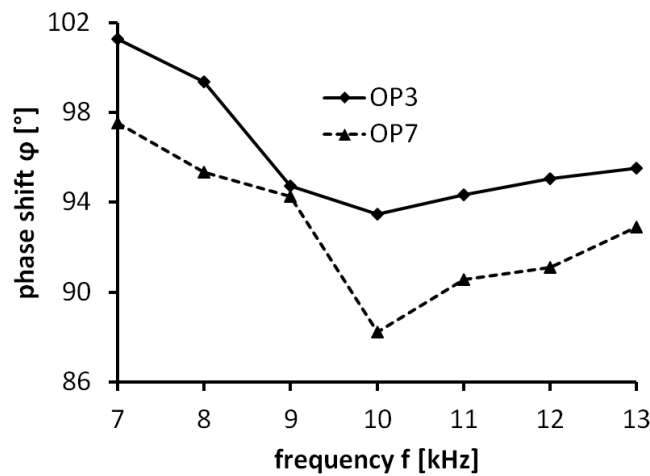


Figure 6.19: Phase shift between pressure and heat release fluctuations for OP3 and OP7

There is just one case where the phase shift (between pressure and heat release fluctuation) is below 90° , so that it thus fulfills the Rayleigh criterion [82]. It is interesting to notice that for both operating points there is a local phase shift minimum at 10 kHz. Even though in the simulation there is no information on the dimension of the combustion chamber, the minimum is at the same frequency that appeared in the experiments. A change in amplitudes has no effect on the phase shift. Also the quotient of amplitudes from excitation pressure and heat release response remains constant.

6.5.4 Conclusion for Pressure Excitation

The phase shift between pressure and heat release fluctuations in all simulations presented in section 6.5.3 is close to 90° . For OP7 there is just one simulation that fulfills the Rayleigh criterion (phase shift $< 90^\circ$); for OP3 there is none. This is contrast to the findings of the experiments [35], where for OP3 the

strongest oscillations were observed. Therefore it has to be concluded that heat release fluctuations which through chemical kinetics are caused by pressure fluctuations are not the reason for the self-excited oscillations in the experiments.

It is much more likely that through pressure gradients in axial direction, as illustrated in Figure 6.16, there are axial velocity gradients which on their part cause heat release fluctuations. And that it is then these heat release fluctuations that couple with pressure fluctuations to yield a Rayleigh integral that is mostly positive and a small phase shift. Therefore it appears to be appropriate to use the results from section 3.5.2 for the calculation of the complex flame transfer function (see section 3.7).

6.6 Extension to Fluctuating Inlet Mass Flow Rates

In the previous section the inlet mass flow rates were held constant. It is more realistic, however, that along with pressure fluctuations in the domain also the mass flow rates would start fluctuating. To identify the amplitude of such fluctuating mass flow rates as well as the phase shift relative to pressure fluctuations two series of simulations are carried out: one for the H_2 and one for the O_2 feed system. In both cases a quasi-2D-domain is used which represents the path of the respective fluid from its dome to the tip of the injector. For illustrative purposes Figure 6.20 shows a simplified depiction of the domains. The location of outlet boundaries in these simulations is identical with the location of inlet boundaries in the previously described simulations of the flame. The inlet is assumed to be a huge reservoir supplied with a constant mass flow rate as specified in Table 6.1. Reference pressure and temperature are taken from the same table. The fluid is a pure substance (H_2 or O_2 , respectively).

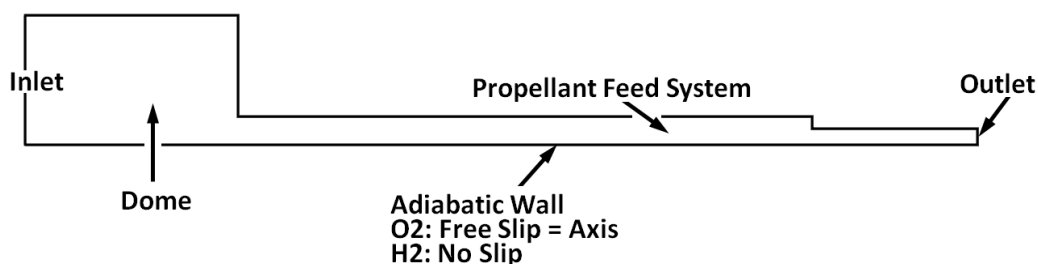


Figure 6.20: Symbolic illustration of the domains used for a propellant feed system

Since there is no combustion involved the computational time is relatively short even for fine grids. Therefore simply equidistant grids are used. Refinements aiming to accurately resolve the boundary layer result in a relatively large number of elements (140000 for H₂ and about 290000 for O₂). The Upwind option is chosen as advection scheme and First Order Turbulence Numeric are employed. In transient simulations the first order backward Euler option is used at a time step size of 2×10^{-6} s.

Simulations without excitation at OP7 are run with constant zero outlet pressure. The pressure difference between inlet and outlet is around 26.2 bar for H₂ and 4.9 bar for O₂, which is close to the measured values from the experiments (24 bar and 4.5 bar, respectively). In transient simulations the outlet pressure is fluctuating as:

$$p_{out} = \hat{p} \sin(\omega t) \quad (6.9)$$

and thereby causes a fluctuating mass flow rate at the outlet. Results from both simulations with a 1 bar pressure amplitude at 10000 Hz are shown in Figure 6.21.

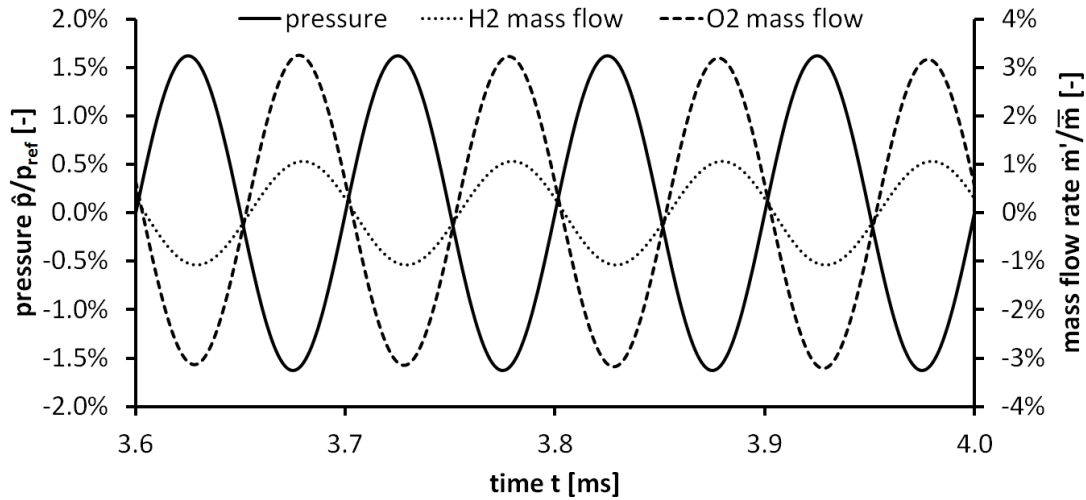


Figure 6.21: Outlet pressure and corresponding mass flow rates at the outlet

In the H₂ feed system a pressure amplitude of 1 bar is relatively small when compared to the pressure difference between inlet and outlet. Consequently this form of excitation has a smaller influence on the mass flow rate. In the O₂ feed system the situation is quite the contrary: the pressure amplitude accounts to more than 20% of the pressure difference between inlet and outlet. As a result

the amplitude of the mass flow rate at the outlet is much larger than in the H₂ feed system. It can also be noticed that fluctuating mass flow rates are not exactly in phase. The phase shift between fluctuating pressure and fluctuating mass flow rate is around -164° for H₂ and -170° for O₂. The different phase shifts are mainly due to different fluid properties and the different geometries of the feed systems. For the sake of completeness one further factor has to be mentioned that also has an influence on the mass flow rates at the outlets: While mass flow rates at the inlets are constant, pressures here are fluctuating and reach almost 10 % of the excitation amplitude at the outlet.

The findings from these preliminary simulations are used to specify fluctuating mass flow rates for the simulation of the flame according to:

$$\dot{m} = \bar{m} + \hat{m} \sin(\omega(t - \Delta t)) \quad (6.10)$$

Simulations of the flame with fluctuating mass flow rates (without applying any further excitation method) show only very small fluctuations of heat release. Accordingly, there is no significant difference in the heat release response whether in a simulation with pressure excitation as described in section 6.5.3 there are additional fluctuating inlet mass flow rates or not. While the amplitude ratios remain the same, the phase shifts between pressure and heat release is decreased to 86.3° (as compared to 88.2° with pressure excitation only). The most significant difference is observable in the Rayleigh-Integral in Figure 6.22, where the peaks in the vicinity of the injector are more distinct (see Figure 6.18 for comparison).

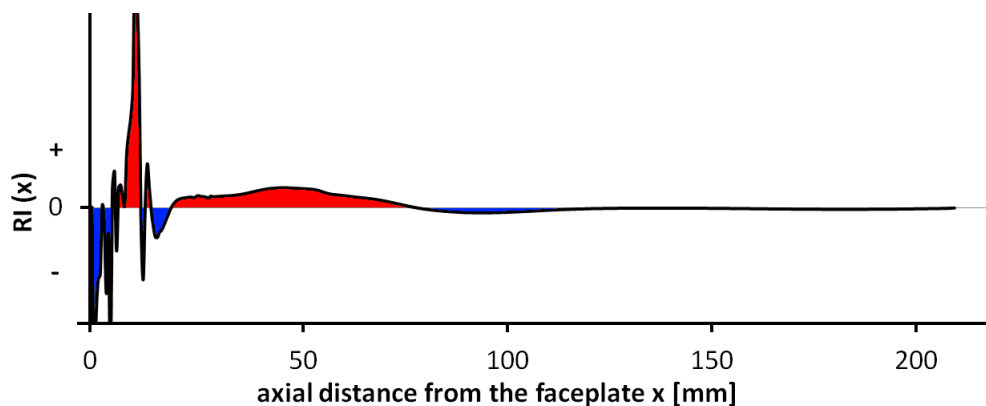


Figure 6.22: Rayleigh-Integral along the axis from simulation of OP7 with fluctuating mass flow rates and pressure excitation (1 bar, 10000 Hz)

Since the phase angle is still close to 90° the fluctuating mass flow rates do not explain the occurrence of combustion instabilities as observed in the experiments. However, the peaks in the Rayleigh-Integral close to the injector provide an indication that processes in the shear layer might be responsible for triggering thermoacoustic oscillations. Therefore an investigation of these phenomena in the vicinity of the injector, with a much finer grid and probably through the use of Large Eddy Simulation appears to be advisable for future projects.

7 Evaluation of Combustion Instabilities

The experiments on the model combustion chamber BKD presented by Gröning et al. [35] show self-excited thermoacoustic fluctuations. An artificial trigger (such as e.g. a bomb) is not required given that in these experiments combustion instabilities are naturally triggered. At all operating points the chamber pressure is above the critical pressure of oxygen so that it is operated at conditions similar to real rocket engines (e.g. see [22] and [23]). Its thrust of 25 kN is comparable to that of an upper stage engine [21]. Data available from these experiments (geometry, mass flow rates, pressure amplitudes, etc.) as well as from CFD simulations (see chapter 6) can be used to evaluate the stability of the chamber.

For the evaluation of combustion instabilities the research code PIANO is used, which was developed at DLR [18]. PIANO uses block-structured curvilinear grids. For spatial discretization it applies a dispersion-relation-preserving finite difference scheme [99], which is a fourth order scheme optimized for computational acoustics. For time integration a fourth order Runge-Kutta scheme is used. It is possible to use either linearized Euler equations (LEEs) or a modification, the acoustic perturbation equations (APEs). In former activities at Lehrstuhl für Thermodynamik APEs were preferred (see e.g. Pieringer [72]). Morgenweck [65] compares results from simulations with APEs and LEEs and discusses the differences. Recently the focus is on using the more general LEEs (e.g. [49], [94]), which deliver better results.

For the simulations in PIANO presented here the faceplate of the combustion chamber is modeled as an inflow with zero mass flow fluctuation. Walls are set to be adiabatic slip walls. Since the divergent part of the nozzle is included, the outflow is placed in the supersonic part of the domain. Therefore the choice of boundary condition at the outflow has no effect on the results within the subsonic part.

7.1 Mean Flow Properties

PIANO requires input data for a mean flow, which can be calculated by a CFD solver – in this case ANSYS CFX [4]. Since requirements for grids are different for calculations in CFX and in PIANO, two different grids are used. The domain in the simulation in CFX is illustrated in Figure 7.1. It is a 2° wedge representing the entire combustion chamber including the cylindrical part and the nozzle. The total number of nodes in this quasi-2D domain is 24000. The entire faceplate is specified as one inlet. The boundary at the end of the nozzle is a supersonic outlet and the outer wall is specified as an adiabatic free slip wall.

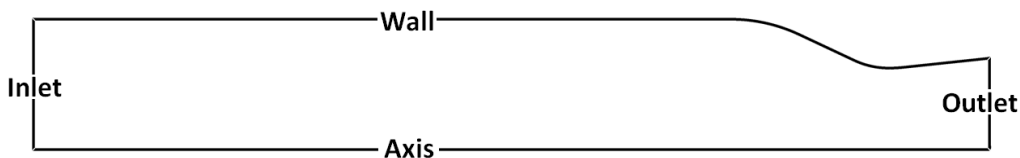


Figure 7.1: Schematic illustration of the domain for the calculation of mean flow properties in CFX

A non-reacting mixture with fixed composition is employed. Mass fraction values for each species are determined as area weighted average at the outlet from results of the steady state simulations of the flame as presented in section 6.3. Heat transfer is simulated with the total energy equation, and the k- ϵ turbulence model is used.

Table 7.1: Operating conditions for the simulation of the combustion chamber in CFX

operating point	3	7
reference pressure [bar]	80.46	61.47
total inlet mass flow [kg/s]	6.70	4.76
inlet temperature [K]	3556	3030

The reference pressure is the same as in the simulation of the flame. The specified temperature value at the inlet is determined from area weighted averaging at the outlet in the simulation with combustion. The mass flow rate specified at the inlet is 1/180 of the total mass flow (sum of oxygen and hydrogen mass flow rates) from the experiments. Data is listed in Table 7.1.

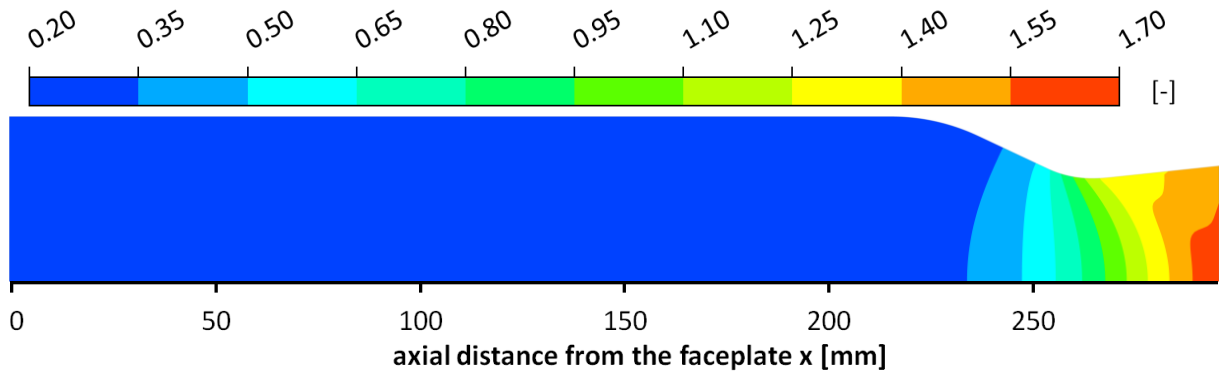


Figure 7.2: Mach number plot from simulation of OP3 in CFX

For each of the two operating points from chapter 6 one simulation is run. Results are projected on the full 3D grid that is required for the simulation in PIANO, which has approximately 0.9 million nodes in 5 blocks. In order to obtain the dimensionless quantities as required for PIANO, values of variables from CFX are reduced by reference quantities according to:

$$\vec{x}_{red} = \frac{x}{L_{ref}}, \quad \rho_{red} = \frac{\rho}{\rho_{ref}}, \quad \vec{v}_{red} = \frac{v}{c_{ref}}, \quad p_{red} = \frac{p}{\rho_{ref} c_{ref}^2} \quad (7.1)$$

Since all employed quantities in PIANO are dimensionless, thus is also the simulated time:

$$t_{red} = t \frac{c_{ref}}{L_{ref}} \quad (7.2)$$

For both simulations the same set of reference quantities was employed: $L_{ref} = 1\text{m}$, $\rho_{ref} = 3\text{kg/m}^3$ and $c_{ref} = 1600\text{m/s}$. The reference pressure is thus $p_{ref} = \rho_{ref} c_{ref}^2 = 76.8\text{bar}$.

7.2 Acoustics Analysis without Combustion

For simulations in PIANO the faceplate of the combustion chamber is modeled as an inflow with zero mass flow fluctuation. Walls are set to be adiabatic slip walls. Since the divergent part of the nozzle is included, the outflow is placed in the supersonic part of the domain. Therefore the choice of boundary condition at the outflow has no effect on the results within the subsonic part. In first simulations in PIANO the two operating points from chapter 6 are run without the FTF being used. An initial acoustic pressure pulse is used to excite the chamber. The pulse has a Gaussian distribution in space and is patched on the previously de-

scribed mean flow. During simulation data is recorded by virtual microphones that are placed on user-defined circles within the domain. In Figure 7.3 the recording of pressure at a virtual microphone is plotted over time.

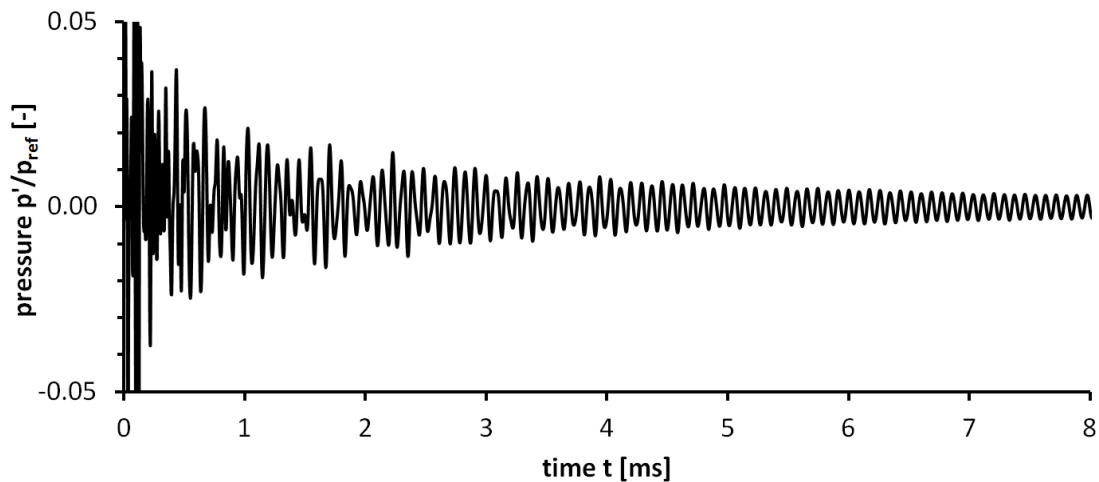


Figure 7.3: Temporal evolution of pressure at a virtual microphone in PIANO for OP3 without combustion being considered

An FFT of the pressure signal in Figure 7.3 can deliver the relevant frequencies within the domain. For operating point 3 this is shown in Figure 7.4. Since values on the vertical axis depend on the considered time range of the pressure signal all values shown in Figure 7.4 are relative to the highest peak.

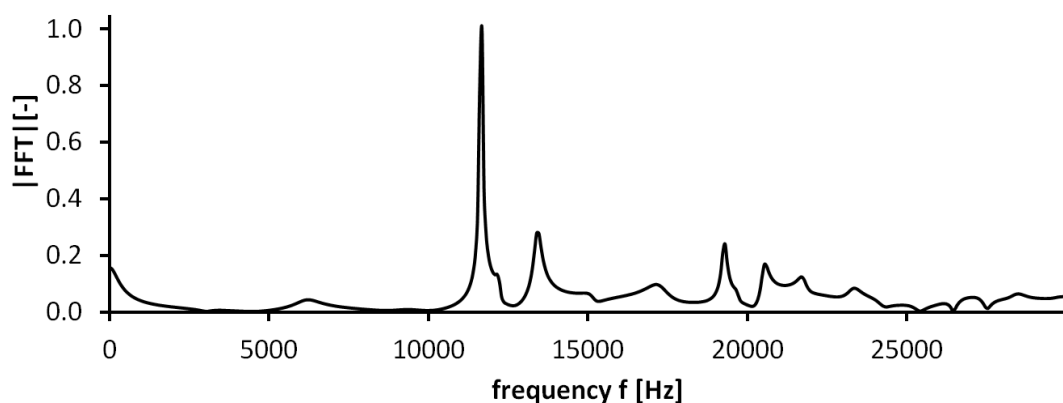


Figure 7.4: FFT gain of the pressure signal from Figure 7.3

The highest peak in Figure 7.4 marks the first tangential mode, which for operating point 3 is at about 11660 Hz. Also the 12560 Hz for operating point 7 is larger than the value of about 10000 Hz that was measured during experiments.

This result is very much dependent on the isentropic exponent that has to be defined in an input file at the beginning of the simulation. The heat capacity ratio γ for both simulations is taken from CFD results of the single flame configuration presented in chapter 6. The area averaged value of the heat capacity ratio is 1.1995 for operating point 3 and 1.2199 for operating point 7. Simulations with lower values of γ as present in the regions of higher temperatures and maximum heat release would produce a value closer to the expected 10000 Hz from experiments.

7.3 Thermoacoustic Analysis with Heat Release

7.3.1 Flame Transfer Function

The idea behind the simulations in chapter 6 was to calculate the parameters of a complex FTF, which then can be used in PIANO. Available thermoacoustic models typically use a simple two parameter formulation [64]. Among these the one introduced by Crocco and Cheng [17] has become most popular over the past decades (see e.g. Pieringer [72]). This FTF has been implemented in PIANO and is currently in use at Lehrstuhl für Thermodynamik (see e.g. [72] or [94]). It relates fluctuations of heat release to pressure fluctuations and has the form:

$$\dot{Q}'(\omega) = \bar{Q} n (1 - e^{i\omega\tau}) \frac{p'(\omega)}{\bar{p}} \quad (7.3)$$

where $\dot{Q}'(\omega)$ and $p'(\omega)$ denote the complex perturbations. Simulations in chapter 6 were conducted with various pressure excitation methods. Results from the simulation with a moving wall at 1 bar amplitude are used to calculate the two parameters n and τ for the FTF.

Table 7.2: Parameters for FTF from the simulation of a single flame in BKD L42

OP	p' [bar]	f [Hz]	φ [rad]	gain [-]	n [-]	τ [-]
3	1	11660	0.803	1.731	1.246	2.096×10^{-5}
7	1	12560	0.384	2.074	1.118	3.008×10^{-5}

The gain is the ratio of the amplitudes of fluctuating heat release rate and pressure normalized with their respective mean values. From phase shift and gain

the interaction index n and time lag τ are calculated. All mentioned parameters are listed in Table 7.2 for two operating points.

7.3.2 Shape Function

Since combustion processes are not evenly spread over the chamber, an additional shape function sf is used:

$$sf(x) = -A^2 [\tanh(Bx - C) + 1] [\tanh(Bx - D) - 1] \quad (7.4)$$

to account for the distribution of heat release. Parameters B , C and D are used to approach the heat release profile along the X-axis. The value of A is determined such, that integration of the shape function over the entire domain gives unity. A value close to zero at the faceplate helps to reduce numerical problems at the inlet boundary. For each of the two operating points a separate set of parameters is determined. Shape function and distribution of heat release along the axis are plotted in Figure 7.5 for OP3.

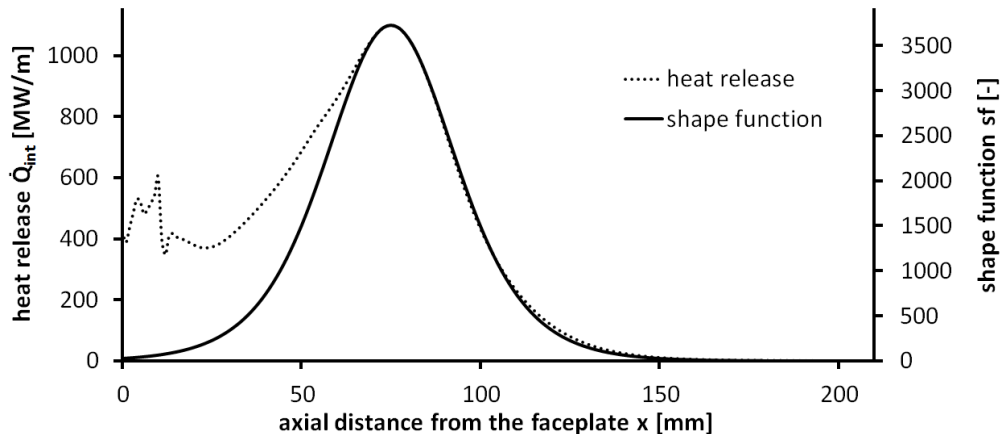


Figure 7.5: Shape function resembling the form of heat release distribution along the axis from the simulation of an L42 flame OP3

7.3.3 Simulation and Results

Simulations with combustion (i.e. a source term in the energy equation) start with the same set-up as described in section 7.2. The initial Gaussian pressure pulse is used to generate a randomly distributed acoustic field. After 1.0 ms the flame transfer function is activated and the pressure response is recorded as plotted in Figure 7.6. The growth of oscillation amplitudes is quite fast and is soon in the range of the mean (or reference) pressure.

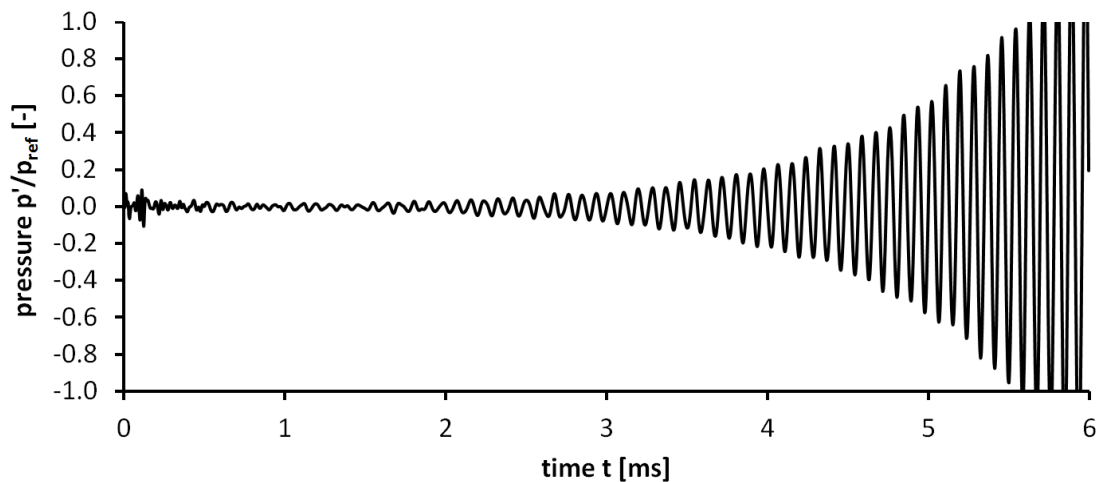


Figure 7.6: Temporal evolution of pressure at a virtual microphone in PIANO for OP3 with combustion being considered after 1.0 ms

Since a linear approach is considered here the growth of amplitudes is not limited. A prediction of pressure amplitudes of the limit cycle would require the application of nonlinear theory. With the linear theory it is possible to evaluate whether for a given configuration there would be an amplification of small perturbations or not. For the parameters chosen here, the amplitudes grow as expected.

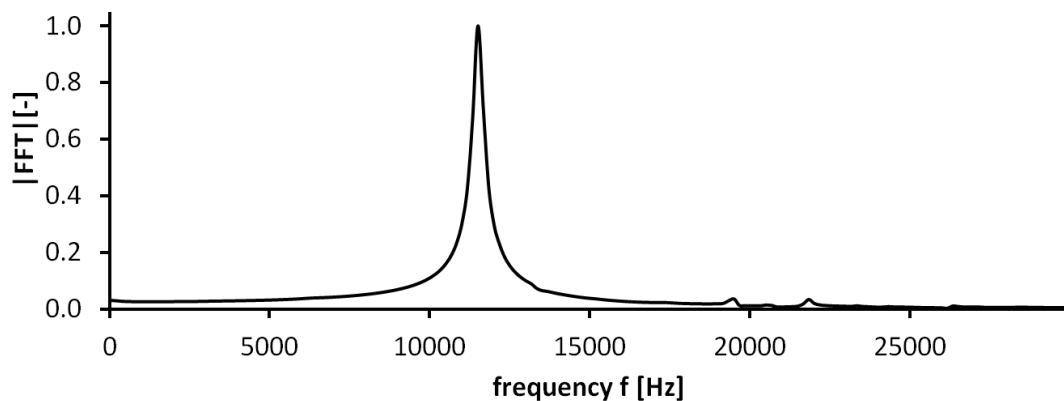


Figure 7.7: FFT gain of the pressure signal from Figure 7.6

The FFT gain plot in Figure 7.7 shows that the most relevant frequency of oscillation is the first transverse mode. The growth rate of acoustic fluctuations can be determined through a gliding FFT investigation [94], which allows evaluating the growth rates of the different acoustic modes separately. The thus calculated growth rate is $987 \frac{1}{s}$ for OP3 and $2005 \frac{1}{s}$ for OP7.

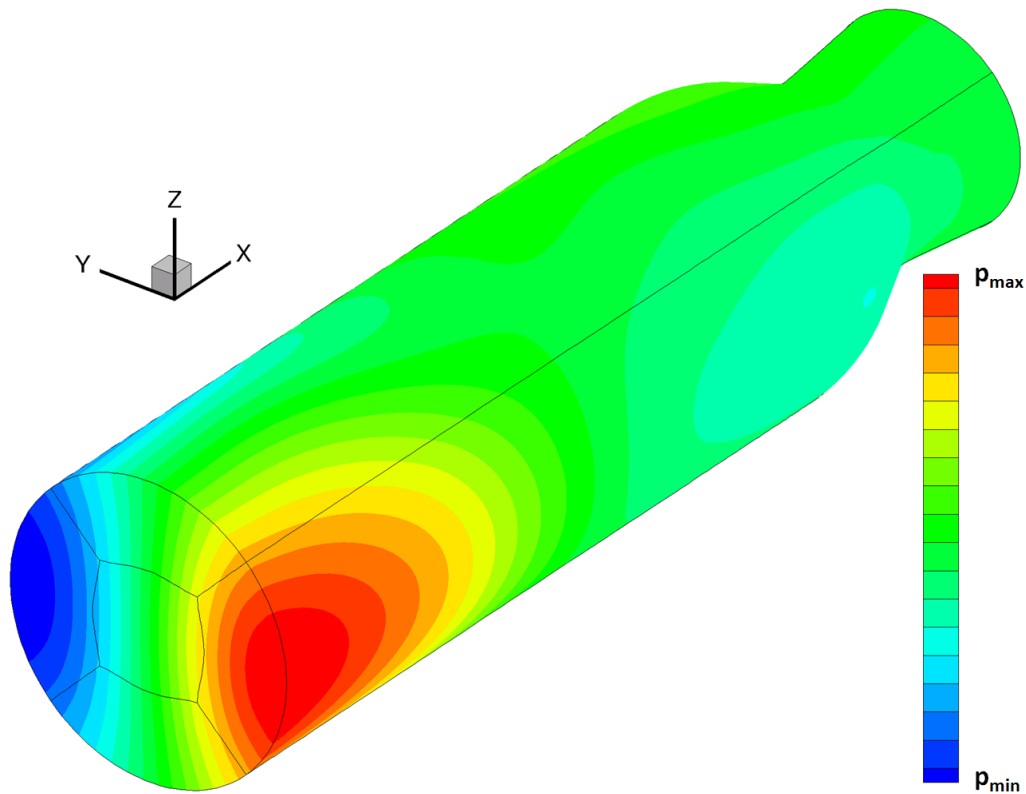


Figure 7.8: Pressure distribution at inflow and combustion chamber wall for OP3

It is interesting to see in Figure 7.8 that the pressure amplitudes are not uniform throughout the domain. Maximum and minimum of pressure are in a plane perpendicular to the X-axis. However this plane is not always in the vicinity of the faceplate as it appears in Figure 7.8, but is rather moving repeatedly from out-flow to inflow. There is no information on whether this behavior also occurs in the experiment.

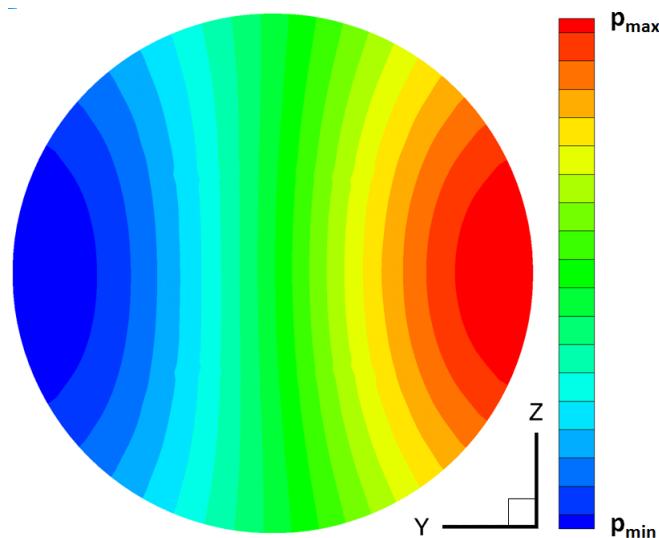


Figure 7.9: Pressure distribution at the faceplate for OP3

Figure 7.9 shows the pressure distribution as it appears after 5 ms in the vicinity of the faceplate, which is where the pressure sensors are located in the experiment [35]. The pressure amplitudes are much larger at this point in the simulation, as with the linear approach the limit cycle cannot be reproduced. However, the distribution itself agrees with experimental data (see [35]).

8 Summary and Conclusions

In this thesis an external routine has been implemented in the commercial flow solver ANSYS CFX to simulate hydrogen-oxygen combustion in a rocket engine. The multi-component flow in CFX contains all eight species of a detailed $\text{H}_2\text{-O}_2$ reaction scheme. Since oxygen is injected into the combustion chamber at high pressures and low temperatures, a real gas equation of state has been used to better describe its behavior. While one species is chosen as constraint, for each of the remaining species in the flow a transport equation is solved. The corresponding source terms are calculated in the external routine. Also reactions with pressure-dependent rate constants can now be considered as well as intermediate complex-forming bimolecular reactions. The detailed reaction mechanisms that were applied in this thesis consist of eight species and 19 reactions. The stiff system of ODEs is solved with a scheme adopted from Press et al. [80]. In order to account for turbulence-chemistry interaction, an assumed PDF approach was implemented. Calculating chemical processes with a detailed reaction mechanism is very time consuming. Therefore tabulation methods have been implemented to reduce the computational cost.

The implementation of the combustion process was validated with quasi 0-dimensional simulations. Simulations of a vitiated co-flow burner at ambient pressure were used to show how the choice of grid size, reaction mechanism, tabulation and turbulence-chemistry interaction affect the results. Data available from the Mascotte test-rig was used for similar simulations at rocket engine conditions. Surprisingly, simulations without considering turbulence-chemistry interaction delivered better agreement with experimental data. Consequently, for the simulation of instabilities on a typical rocket engine flame (L42) turbulence chemistry interaction was not considered.

Velocity excitation of a single L42 flame with source terms in the momentum equation resulted in a response of the global heat release fluctuation with exactly the double frequency of the velocity excitation. Therefore it can be concluded that the velocity coupling has no effect on the amplification of the first transversal mode.

Several pressure excitation methods have been applied in this thesis. The method with mass sources on the boundaries has the drawback that in simulations with detailed chemistry the results are dependent on the specified composition on the boundary. Therefore with a moving wall (and hence deforming mesh) an alternative method has been introduced, which probably has not been previously used for pressure excitation of rocket engine flames. The approach using an external routine for combustion also offered the unique opportunity to apply a third pressure excitation method. This method can give information about the direct effect of chemical kinetics on heat release fluctuations.

In simulations with excitation in the external routine in the range around 10 kHz the phase shift between pressure and heat release fluctuations showed a dependence on frequency. The value of the phase shift was close to but mostly above 90° . According to the Rayleigh integral even for the slightly less than 90° in one simulation there would be only a very weak coupling. This would not explain the self-excited oscillations that have been observed in the experiments. The extension to fluctuating mass flow rates only slightly decreased the phase shift between the fluctuations of pressure and heat release.

A small phase shift between pressure and heat release fluctuations was observed in simulations with a moving wall. In these simulations pressure phase and amplitude were dependent on the location within the domain and may be the reason for the strong coupling: Through pressure gradients in axial direction a fluctuating axial velocity is introduced, which causes additional heat release fluctuations. Results from the simulation with the moving wall were thus used to calculate parameters of a flame transfer function.

In simulations of thermoacoustic fluctuations in PIANO two operating points were compared with each other. The FTF accounts for coupling between pressure and heat release, the shape function is able to consider the distribution of heat release along the axis. With the utilized input parameters both operating points showed a fast growth of amplitudes at the first tangential mode (one slightly stronger than the other). For the prediction of the limit cycle it would be necessary to use a non-linear approach. Possible extension of the FTF would probably be to account for variable (e.g. frequency dependent) parameters.

In future activities improvements to several of the models used in this work could be addressed well. Using real gas representation for oxygen in a multi-component flow in CFX has turned out to be difficult for the simulation of a flame. An improvement in the tabulation of real gas data would probably help to

avoid problems that occur due to the use of tables. In simulations with a deforming mesh all points on the walls moved simultaneously. An expedient improvement of this method would be to have points on the wall which move with various velocities. Results from simulation with fluctuating mass flow rates indicated that processes in the shear layer might be responsible for triggering thermoacoustic oscillations. An investigation of phenomena in the vicinity of the injector appears to be advisable for future projects.

References

- [1] **Anderson, J. D.:** *Hypersonic and High Temperature Gas Dynamics*. AIAA; 2006
- [2] **ANSYS, Inc.:** *ANSYS CFX – Pre User’s Guide*. ANSYS, Inc., Release 13.0; 2010
- [3] **ANSYS, Inc.:** *ANSYS CFX – Solver Modeling Guide*. ANSYS, Inc., Release 13.0; 2010
- [4] **ANSYS, Inc.:** *ANSYS CFX – Solver Theory Guide*. ANSYS, Inc., Release 13.0; 2010
- [5] **ANSYS, Inc.:** *ANSYS FLUENT User’s Guide*. ANSYS, Inc., Release 13.0; 2010
- [6] **Aungier, R. H.:** *A Fast, Accurate Real Gas Equation of State for Fluid Dynamic Analysis Applications*. Journal of Fluids Engineering, Vol. 117, pp. 277-281; 1995
- [7] **Barth, T. J.; Jespersen, D. C.:** *The Design and Application of Upwind Schemes on Unstructured Meshes*. AIAA Paper 89-0366; 1989
- [8] **Baurle, R. A.:** *Modeling of Turbulent Reacting Flows with Probability Density Functions for Scramjet Applications*. Ph.D. thesis, North Carolina State University; 1995
- [9] **Benarous, A.; Liazid A.:** *H2-O2 Supercritical Combustion Modeling Using a CFD Code*. Thermal Science, vol. 13, no. 3, pp. 139-152; 2009
- [10] **Bird, R. B.; Stewart, W. E.; Lightfoot, E. N.:** *Transport Phenomena*. 2nd ed., John Wiley & Sons; 2007
- [11] **Brown, P. N.; Byrne, G. D.; Hindmarsh, A. C.:** *VODE, a Variable-Coefficient ODE Solver*. SIAM Journal on Scientific and Statistical Computing, vol. 10, no. 5, pp. 1038-1051; 1989
- [12] **Burden, R. L.; Faires, J. D.:** *Numerical Analysis*. 7th ed., Brooks/Cole; 2001
- [13] **Burke, S. P.; Schumann, T. E. W.:** *Diffusion Flames*. Industrial and Engineering Chemistry, vol. 20, pp. 998-1005; 1928

- [14] **Cabra, R.; Myhrvold, T.; Chen, J. Y., Dibble, R. W.; Karpentis, A. N., Barlow, R.S.:** *Simultaneous Laser Raman-Rayleigh-LIF Measurements and Numerical Modeling Results of a Lifted Turbulent Jet Flame in Vitiated Coflow*. Proceedings of the Combustion Institute, Vol. 29, pp. 1881-1888; 2002
- [15] **Cheng, G.C.; Farmer, R.:** *Real Fluid Modeling of Multiphase Flows in Liquid Rocket Engine Combustors*. Journal of Propulsion and Power, vol. 22, no. 6, pp. 1373-1381; 2006
- [16] **Contreras Espada, J:** *Numerical Simulation of Reacting Flows under Laminar Conditions with Detailed Chemistry*. Ph.D. thesis, TU Darmstadt/EKT; 2010
- [17] **Crocco, L.; Cheng, S.-I:** *Theory of Combustion Instability in Liquid Propellant Rocket Motors*. Butterworths Scientific Publications; 1956
- [18] **Delfs, J.; Bauer, M.; Ewert, R.; Grogger, H.; Lummer, M.; Lauke, T.:** *Numerical Simulation of Aerodynamic Noise with DLR's Aeroacoustic Code PIANO*. PIANO manual for version 5.2; DLR 2008
- [19] **Di Domenico, M.:** *Numerical Simulations of Soot Formation in Turbulent Flows*. Ph.D. thesis, DLR Institut für Verbrennungstechnik Stuttgart, 2007
- [20] **Dowling, A. P.; Ffowcs Williams, J. E.:** *Sound and Sources of Sound*. Ellis Horwood; 1983
- [21] **EADS Astrium:** *Aestus Rocket Engine*. URL: <http://cs.astrium.eads.net/sp/launcher-propulsion/rocket-engines/aestus-rocket-engine.html> [2013-09-17]
- [22] **EADS Astrium:** *Vinci Rocket Engine - Thrust Chamber*. URL: <http://cs.astrium.eads.net/sp/launcher-propulsion/rocket-engines/vinci-rocket-engine.html> [2013-09-17]
- [23] **EADS Astrium:** *Vulcain Rocket Engine - Thrust Chamber*. URL: <http://cs.astrium.eads.net/sp/launcher-propulsion/rocket-engines/vulcain-rocket-engine.html> [2013-09-17]
- [24] **Fiala, T.; Sattelmayer, T.:** *Heat Release and OH* Radiation in Laminar Non-Premixed Hydrogen-Oxygen Flames*. 51st AIAA Aerospace Sciences Meeting including the New Horizons Forum and Aerospace Exposition; 2013
- [25] **Fiala, T.; Sattelmayer, T.:** *A Posteriori Computation of OH* Radiation from Numerical Simulations in Rocket Combustion Chambers*. 5th European Conference for Aeronautics and Space Sciences; 2013

-
- [26] **Fick, A:** *Ueber Diffusion*. Annalen der Physik, vol. 170, pp. 59-86; 1855
- [27] **Förster, H.; Sattelmayer, T.:** *Computationally efficient Tabulation of H₂-Air Combustion with Turbulence-Chemistry Interaction*. 14th AIAA/AHI Int. Space Planes and Hypersonic Sys. and Techn. Conference, Canberra, AIAA-2006-8038; 2006
- [28] **Förster, H:** *Einfluss der Turbulenz-Chemie Interaktion auf das Zündverhalten schwach stabilisierter Überschallflammen*. Ph.D. thesis, Technische Universität München; 2010
- [29] **Gerlinger, P.:** *Investigation of an Assumed PDF Approach for Finite-Rate Chemistry*. Combustion Science and Technology, vol. 175: 841-872; 2003
- [30] **Gerlinger, P.:** *Numerische Verbrennungssimulation*. Springer; 2005
- [31] **Gerlinger, P.; Möbus, H.; Brüggemann, D.:** *An Implicit Multigrid Method for Turbulent Combustion*. Journal of Computational Physics, vol. 167, pp. 247-276; 2001
- [32] **Gilbert, R. G., Luther, K.; Troe, J.:** *Theory of Thermal Unimolecular Reactions in the Fall-off Range*. II. Weak Collision Rate Constants. Berichte der Bunsengesellschaft für physikalische Chemie, 87: 169-177; 1983
- [33] **Girimaji, S. S.:** *Assumed β -pdf Model for Turbulent Mixing: Validation and Extension to Multiple Scalar Mixing*. Combustion Science and Technology, vol. 78, pp. 177-196; 1991
- [34] **Gordon, S.; McBride, B. J.:** *Computer Program for Calculation of Complex Chemical Equilibrium Compositions, Rocket Performance, Incident and Reflected Shocks and Chapman-Jouguet Detonations*. NASA Report SP-273; 1971
- [35] **Gröning, S; Oswald, M.; Sattelmayer, T.:** *Selbst erregte tangentielle Moden in einer Raketendbrennkammer unter repräsentativen Bedingungen*. 61. Deutscher Luft- und Raumfahrtkongress; 2012
- [36] **Habiballah, M.; Orain, M.; Grisch, F.; Vingert, L.; Gicquel, P.:** *Experimental Studies of High-Pressure Cryogenic Flames on the Mascotte Facility*. Combustion Science and Technology, Vol. 178, pp. 101-128 ; 2006
- [37] **Habiballah, M.; Zurbach, S.:** *Test Case RCM-3, Mascotte single injector, 60 bar*. 2nd International Workshop on Rocket Combustion Modeling; 2001

- [38] **Hantschk, C.-C.; Vortmeyer, D.:** *Numerical Simulation of Self-Excited Thermoacoustic Instabilities in a Rijke Tube*. Journal of Sound and Vibration, vol. 220, pp. 511-522; 1999
- [39] **Harlow, F. H.; Welch, J. E.:** *Numerical calculation of time-dependent viscous incompressible flow of fluid with free surface*. The Physics of Fluids, vol. 8, pp. 2182-2189; 1965
- [40] **Harrje, D. T.; Reardon, F. H.:** *Liquid Propellant Rocket Combustion Instability*. NASA SP-194; 1972
- [41] **Heckl, M. A.:** *Non-linear acoustic effects in the Rijke Tube*. Acustica, vol. 72, pp. 63-71; 1990
- [42] **Hippler, H.; Troe, J.:** *Rate constants of the reaction $HO+H_2O_2 \rightarrow HO_2+H_2O$ at $T \geq 1000$ K*. Chemical Physics Letters, vol. 192, pp. 333-337; 1992
- [43] **Hippler, H.; Troe, J.; Willner, J.:** *Shock wave study of the reaction $HO_2+HO_2 \rightarrow H_2O_2+O_2$: Confirmation of a rate constant minimum near 700K*. Journal of Chemical Physics, vol. 93, pp. 1755-1760; 1990
- [44] **Hirsch, C.:** *Numerical Computation of Internal and External Flows*. 2nd ed., Elsevier; 2007
- [45] **Hirschfelder, J. O., Curtiss, C. F., Bird, R. B.:** *Molecular Theory of Gases and Liquids*. Wiley; 1954
- [46] **Issa, R. I.:** *Solution of the Implicit Discretized Fluid Flow Equations by Operator Splitting*. Journal of Computational Physics, vol. 62, pp. 40-65; 1985
- [47] **Jachimowski, C. J.:** *An Analytical Study of the Hydrogen-Air Reaction Mechanism with Application to Scramjet Combustion*. NASA Technical Paper 2791; 1988
- [48] **Kaess, R.; Koeglmeier, S; Behr, R.; Kniesner, B.; Sattelmayer, T.:** *Impact of Axial Gradients on Combustion Chamber Acoustics*. 5th European Conference for Aerospace Sciences; 2013
- [49] **Kaess, R.; Koeglmeier, S; Schmid, M; Sattelmayer, T.:** *Linearized Euler Calculation of Acoustic of a Rocket Combustion Chamber*. Proceeding of the 2nd REST Modelling Workshop; 2010
- [50] **Kee, R. J.; Dixon-Lewis, G.; Warnatz, J.; Coltrin, M. E.; Miller, J. A.:** *A FORTRAN Computer Code Package for the Evaluation of Gas-Phase, Multicomponent Transport Properties*. Sandia National Laboratories Report, SAND86-8246; 1986

-
- [51] **Kee, R. J.; Grcar, J. F.; Smooke, M. D.; Miller, J. A.:** *A FORTRAN Program for Modeling Steady Laminar One-Dimensional Premixed Flames*. Sandia National Laboratories Report, SAND85-8240; 1985
- [52] **Kee, R. J.; Rupley, F. M.; Meeks, E.:** *CHEMKIN-III: A FORTRAN Chemical Kinetics Package for the Analysis of Gas-Phase Chemical and Plasma Kinetics*. Sandia National Laboratories Report SAND96-8216; 1996
- [53] **Kee, R. J.; Rupley, F. M.; Miller, J. A.:** *CHEMKIN-II: A FORTRAN Chemical Kinetics Package for the Analysis of Gas-Phase Chemical Kinetics*. Sandia National Laboratories Report SAND89-8009; 1989
- [54] **Kee, R. J.; Warnatz, J.; Miller, J. A.:** *A FORTRAN Computer Code Package for the Evaluation of Gas-Phase Viscosities, Conductivities, and Diffusion Coefficients*. Sandia National Laboratories Report, SAND83-8209; 1983
- [55] **Lemmon, E. W.; McLinden, M. O.; Friend, D. G.:** *Thermophysical Properties of Fluid Systems*. NIST Chemistry WebBook, NIST Standard Reference Database Number 69. - URL: <http://webbook.nist.gov>; 2005
- [56] **Li, J.; Zhao, Z.; Kazakov, A.; Dryer, F. L.:** *An Updated Comprehensive Kinetic Model of Hydrogen Combustion*. International Journal of Chemical Kinetics, vol. 36, pp. 566-575; 2004
- [57] **Liang, L.; Kong, S.-G.; Jung C.; Reitz, R. D.:** *Development of a Semi-implicit Solver for Detailed Chemistry in Internal Combustion Engine Simulations*. Journal of Engineering for Gas Turbines and Power, vol.-129, pp. 271-278; 2007
- [58] **Lindemann, F. A.:** *Discussion on "The radiation theory of chemical action"*. Transactions of the Faraday Society, vol. 17, pp. 598-599; 1922
- [59] **Lockwood, F. C.; Naguib, A. S.:** *The Prediction of the Fluctuations in the Properties of Free, Round-Jet, Turbulent, Diffusion Flames*. Combustion and Flame, vol. 24., pp. 109-124; 1975
- [60] **Lutz, A. E.; Kee, R. J.; Miller J. A.:** *SENKIN: A FORTRAN Program for Predicting Homogeneous Gas Phase Chemical Kinetics with Sensitivity Analysis*. Sandia National Laboratories Report SAND87-8248 Revised; 1997
- [61] **Lyubar, A.:** *Numerisch effiziente Modellierung von Überschallbrennkammern mit detaillierter Kinetik*. Ph.D. thesis, Technische Universität München; 2005

- [62] **Majumdar, S.:** *Role of Underrelaxation in Momentum Interpolation for Calculation of Flow with Nonstaggered Grids*. Numerical Heat Transfer, vol. 13, pp. 125-125; 1988
- [63] **Marinov, N. M.; Westbrook, C. K.; Pitz, W. J.:** *Detailed and Global Chemical Kinetics Model for Hydrogen*. Transport Phenomena in Combustion, pp. 118-129; 1996
- [64] **Mitchell, C. E.:** *Analytical Models for Combustion Instability*. Progress in Astronautics and Aeronautics, vol. 169, Liquid Rocket Combustion Instability, chapter 15; 1995
- [65] **Morgenweck, D.:** *Modellierung des Transferverhaltens im Zeitbereich zur Beschreibung komplexer Randbedingungen in Raketenschubkammern*. Ph.D. thesis, Technische Universität München; 2013
- [66] **Mueller, M. A.; Kim, T. J.; Yetter, R. A.; Dryer, F. L.:** *Flow reactor studies and kinetic modeling of the H₂O₂ reaction*. International Journal of Chemical Kinetics, vol. 31, pp. 113-125; 1999
- [67] **Neufeld, P. D.; Janzen, A. R.; Aziz, R. A.:** *Empirical Equations to Calculate 16 of the Transport Collision Integrals $\Omega^{(l,s)*}$ for the Lennard-Jones (12-6) potential*. The Journal of Chemical Physics, vol. 57, pp. 1100-1102; 1972
- [68] **Nicole, A.; Vingert, L.; Habiballah, M.:** *Test Case RCM-2, Mascotte single injector, 60 bar*. 3rd International Workshop on Rocket Combustion Modeling; 2006
- [69] **Ó Conaire, M.; Curran, H. J.; Simmie, J. M.; Pitz, W. J.; Westbrook, C. K.:** *A Comprehensive Modeling Study of Hydrogen Oxidation*. International Journal of Chemical Kinetics, vol. 36, pp. 603-622; 2004
- [70] **Patankar, S. V.:** *Numerical Heat Transfer and Fluid Flow*. Hemisphere Publishing Corp.; 1980
- [71] **Peters, N.:** *Turbulent Combustion*. Cambridge University Press; 2000
- [72] **Pieringer, J. E.:** *Simulation selbsterregter Verbrennungsschwingungen in Raketenschubkammern im Zeitbereich*. Ph.D. thesis, Technische Universität München; 2008
- [73] **Poinsot, T. J.; Lele, S. K.:** *Boundary Conditions for Direct Simulations of Compressible Viscous Flows*. Journal of Computational Physics, vol. 101, pp. 104-129; 2005
- [74] **Poinsot, T.; Veynante, D.:** *Theoretical and Numerical Combustion*. 2nd ed., Edwards; 2005

-
- [75] **Poling, E.; Prausnitz, J. M.; O'Connell, J. P.:** *The Properties of Gases and Liquids*. McGraw-Hill, New York; 2001
- [76] **Pope, S. B.:** *Computationally efficient implementation of combustion chemistry using in situ adaptive tabulation*. *Combustion Theory Modelling*. vol. 1, pp. 41-63; 1997
- [77] **Pope, S. B.:** *Turbulent Flows*. Cambridge University Press; 2000
- [78] **Poschner, M.; Pfitzner M.:** *Real gas CFD simulation of supercritical H₂-LOX combustion in the Mascotte single-injector combustor using a commercial CFD code*. 46th AIAA Aerospace Sciences Meeting and Exhibit, Reno, 7.-10.01.2008, AIAA 2008-952; 2008
- [79] **Poschner, M.; Pfitzner, M.:** *CFD simulation of supercritical LOX/GH₂ combustion considering consistent real gas thermodynamics*. 4th European Combustion Meeting; 2009
- [80] **Press, W. H.; Teukolksy, S. A.; Vetterling, W. T.; Flannery, B. P.:** *Numerical Recipes in C*. 2nd ed., Cambridge University Press; 1992
- [81] **Preuß, E.; Spille-Kohoff, A.:** *Numerical Simulation of Multicomponent Diffusion with ANSYS CFX*. ANSYS Conference & 28th CADFEM Users' Meeting, Aachen; 2010
- [82] **Putnam, A. A.; Dennis, W. R.:** *Burner Oscillations of the Gauze-Tone Type*. *The Journal of the Acoustical Society of America*, vol. 26, pp. 716-725; 1954
- [83] **Ramshaw, J. D.:** *Self-Consistent Effective Binary Diffusion in Multicomponent Gas Mixtures*. *Journal of Non-Equilibrium Thermodynamics*, vol. 15, pp. 295-300; 1990
- [84] **Rayleigh, J. W. S.:** *The Theory of Sound*. Macmillan; 1877
- [85] **Redlich, O.; Kwong, J. N. S.:** *On the Thermodynamics of Solution. V - An Equation of State*. *Fugacities of Gaseous Solutions*. *Chemical Reviews*, Vol. 44, pp. 233-244; 1949
- [86] **Rey, C.; Ducruix, S.; Candel, S.:** *A method for the transverse modulation of reactive flows with application to combustion instability*. *Combustion Theory and Modelling*, vol. 9, pp. 5-22; 2005
- [87] **Rhie, C. M.; Chow, W. L.:** *A Numerical Study of the Turbulent Flow Past an Isolated Airfoil with Trailing Edge Separation*. AIAA Paper 82-0998, 1982

- [88] **Richardson, E. G.; Tyler, E.:** *The Transverse Velocity Gradient near the Mouths of Pipes in Which an Alternating of Continuous Flow of Air is Established.* The Proceedings of the Physical Society, vol. 42, Part I, pp. 1-15; 1929
- [89] **Rijke, P. L.:** *Notiz über eine neue Art, die Luft in einer an beiden Enden offenen Röhre in Schwingung zu versetzen.* Annalen der Physik, vol. 107, pp. 339-343; 1859
- [90] **Rist, D.:** *Dynamik realer Gase.* Springer; 1996
- [91] **Schmid, M.; Sattelmayer, T.:** *Influence of pressure and velocity perturbations on the heat release fluctuations for coaxial GH₂/GO₂ injection.* 4th European Conference for Aerospace Sciences; 2011
- [92] **Schöyer H. F. R.:** *Combustion Instability in Liquid Rocket Engines.* esa WPP-062; 1993
- [93] **Schultz, E.; Shepherd, J.:** *Validation of Detailed Reaction Mechanisms for Detonation Simulation.* Explosion Dynamics Laboratory Report FM99-5; 2000
- [94] **Schulze, M.; Urbano, A.; Zahn, M.; Schmid, M.; Sattelmayer, T.; Oswald, M.:** *Thermoacoustic Feedback Analysis of a Cylindrical Combustion Chamber under Supercritical Conditions.* 50th AIAA/ASME/SAE/ASEE Joint Propulsion Conference, AIAA 2014-3776, Cleveland, Ohio, USA, 2014
- [95] **Sexl, T.:** *Über den von E. G. Richardson entdeckten "Annulareffekt".* Zeitschrift für Physik, vol. 61, pp. 349-362; 1930
- [96] **Smooke, M. D.; Mitchell, R. E.; Keyes, D. E.:** *Numerical Solution of Two-Dimensional Axisymmetric Laminar Diffusion Flames.* Combustion Science and Technology, Vol. 67, pp 85-122; 1989
- [97] **Sutton, G. P.; Biblarz, O.:** *Rocket Propulsion Elements.* 7th ed., John Wiley & Sons; 2001
- [98] **Svehla, R. A.:** *Estimated Viscosities and Thermal Conductivities of Gases at High Temperatures.* NASA Technical Report R-132; 1962
- [99] **Tam, C. K. W.; Webb, J. C.:** *Dispersion-Relation-Preserving Finite Difference Schemes for Computational Acoustic.* Journal of Computational Physics, vol. 107, pp. 262-291; 1993
- [100] **Troe, J.:** *Theory of Thermal Unimolecular Reactions in the Fall-off Range. I. Strong Collision Rate Constants.* Berichte der Bunsengesellschaft für physikalische Chemie, 87: 161–169; 1983

-
- [101] **Turns, S. R.:** *An Introduction to Combustion*. 2nd ed., McGraw-Hill; 2000
- [102] **Van Doormaal, J. P.; Raithby, G. D.:** *Enhancements of the SIMPLE Method for Predicting Incompressible Fluid Flows*. Numerical Heat Transfer, vol. 7, pp. 147-163; 1984
- [103] **Warnatz, J.; Maas, U.; Dibble R. W.:** *Combustion*. 4th ed., Springer; 2006
- [104] **White, F. M.:** *Viscous Fluid Flow*. McGraw-Hill, 3rd ed.; 2006
- [105] **Wilson, G. J.; MacCormack R. W.:** *Modeling Supersonic Combustion Using a Fully Implicit Numerical Method*. AIAA Journal, vol. 30, pp. 1008-1015; 1992
- [106] **Yang, B.; Pope, S. B.:** *An Investigation of the Accuracy of Manifold Methods and Splitting Schemes in the Computational Implementation of Combustion Chemistry*. Combustion and Flame, vol. 112., pp. 16-32; 1998
- [107] **Zellhuber, M.; Tay Wo Chong, L.; Polifke, W.:** *Non-Linear Flame Response at Small Perturbation Amplitudes - Consequences for Analysis of Thermoacoustic Instabilities*. Proceedings of the European Combustion Meeting; 2011
- [108] **Zwart, P.; Abshoff, J.:** *Non-reflective Boundary Conditions in CFX-5*. CFX Validation Report, CFX-VAL01/07042/10/2005, Ansys Canada Ltd.; 2005

A Appendix

A.1 Material Properties

Table A.1: Molar masses of the species involved in combustion

	H	H ₂	H ₂ O	H ₂ O ₂	HO ₂	O	O ₂	OH	N ₂
M [g/mol]	1.01	2.02	18.02	34.01	33.01	16.00	31.99	17.01	28.01

Table A.2: Coefficients for the polynomials in equations (3.3), (3.4) and (3.5) in the lower temperature range (up to 1000 K)

	a_1 [-]	a_2 [K ⁻¹]	a_3 [K ⁻²]	a_4 [K ⁻³]	a_5 [K ⁻⁴]	a_6 [K]	a_7 [-]
H	2.500000E+00	0.000000E+00	0.000000E+00	0.000000E+00	0.000000E+00	2.547160E+04	-4.601176E-01
H ₂	3.298124E+00	8.249440E-04	-8.143010E-07	-9.475430E-11	4.134870E-13	-1.012520E+03	-3.294094E+00
H ₂ O	3.386842E+00	3.474980E-03	-6.354700E-06	6.968580E-09	-2.506590E-12	-3.020810E+04	2.590233E+00
H ₂ O ₂	3.388753E+00	6.569230E-03	-1.485010E-07	-4.625810E-09	2.471510E-12	-1.766310E+04	6.785363E+00
HO ₂	2.979963E+00	4.996700E-03	-3.791000E-06	2.354190E-09	-8.089020E-13	1.762270E+02	9.222724E+00
O	2.946429E+00	-1.638170E-03	2.421030E-06	-1.602840E-09	3.890700E-13	2.914760E+04	2.963995E+00
O ₂	3.212936E+00	1.127490E-03	-5.756150E-07	1.313880E-09	-8.768550E-13	-1.005250E+03	6.034738E+00
OH	3.637266E+00	1.850910E-04	-1.676160E-06	2.387200E-09	-8.431440E-13	3.606780E+03	1.358860E+00
N ₂	3.298677E+00	1.408240E-03	-3.963220E-06	5.641510E-09	-2.444860E-12	-1.020900E+03	3.950372E+00

Table A.3: Coefficients for the polynomials in equations (3.3), (3.4) and (3.5) in the upper temperature range (above 1000 K)

	a_1 [-]	a_2 [K ⁻¹]	a_3 [K ⁻²]	a_4 [K ⁻³]	a_5 [K ⁻⁴]	a_6 [K]	a_7 [-]
H	2.500000E+00	0.000000E+00	0.000000E+00	0.000000E+00	0.000000E+00	2.547160E+04	-4.601176E-01
H ₂	2.991423E+00	7.000640E-04	-5.633830E-08	-5.633830E-08	1.582750E-15	-8.350340E+02	-1.355110E+00
H ₂ O	2.672146E+00	3.056290E-03	-8.730260E-07	1.201000E-10	-6.391620E-15	-2.989921E+04	6.862817E+00
H ₂ O ₂	4.573167E+00	4.336140E-03	-1.474690E-06	2.348900E-10	-1.431650E-14	-1.800700E+04	5.011369E-01
HO ₂	4.072191E+00	2.131300E-03	-5.308140E-07	6.112270E-11	-2.841160E-15	-1.579730E+02	3.476029E+00
O	2.542060E+00	-2.755060E-05	-3.102800E-09	4.551070E-12	-4.368050E-16	2.923080E+04	4.920308E+00
O ₂	3.697578E+00	6.135200E-04	-1.258840E-07	1.775280E-11	-1.136430E-15	-1.233930E+03	3.189166E+00
OH	2.882730E+00	1.013970E-03	-2.276880E-07	2.174680E-11	-5.126300E-16	3.886890E+03	5.595712E+00
N ₂	2.926640E+00	1.487980E-03	-5.684760E-07	1.009700E-10	-6.753350E-15	-9.227980E+02	5.980528E+00

A.2 Reaction Mechanisms

Table A.4: Reaction mechanism from Jachimowski [47], modified by Wilson and MacCormack [105].

Reactions			A_r	β_r	E_r
(1)	$\text{H} + \text{O}_2$	$\rightleftharpoons \text{OH} + \text{O}$	$2.60 \cdot 10^{14}$	0	16800
(2)	$\text{O} + \text{H}_2$	$\rightleftharpoons \text{OH} + \text{H}$	$1.80 \cdot 10^{10}$	1.00	8900
(3)	$\text{OH} + \text{H}_2$	$\rightleftharpoons \text{H}_2\text{O} + \text{H}$	$2.20 \cdot 10^{13}$	0	5150
(4)	$\text{OH} + \text{OH}$	$\rightleftharpoons \text{H}_2\text{O} + \text{O}$	$6.30 \cdot 10^{12}$	0	1090
(5)	$\text{H} + \text{OH} + \text{M}$	$\rightleftharpoons \text{H}_2\text{O} + \text{M}$	$2.20 \cdot 10^{22}$	-2.00	0
(6)	$\text{H} + \text{H} + \text{M}$	$\rightleftharpoons \text{H}_2 + \text{M}$	$6.40 \cdot 10^{17}$	-1.00	0
(7)	$\text{H} + \text{O} + \text{M}$	$\rightleftharpoons \text{OH} + \text{M}$	$6.00 \cdot 10^{16}$	-0.60	0
(8)	$\text{H} + \text{O}_2 + \text{M}$	$\rightleftharpoons \text{HO}_2 + \text{M}$	$2.10 \cdot 10^{15}$	0	-1000
(9)	$\text{H}_2 + \text{O}_2$	$\rightleftharpoons \text{HO}_2 + \text{H}$	$1.00 \cdot 10^{14}$	0	56000
(10)	$\text{HO}_2 + \text{H}$	$\rightleftharpoons \text{OH} + \text{OH}$	$1.40 \cdot 10^{14}$	0	1080
(11)	$\text{HO}_2 + \text{H}$	$\rightleftharpoons \text{H}_2\text{O} + \text{O}$	$1.00 \cdot 10^{13}$	0	1080
(12)	$\text{HO}_2 + \text{O}$	$\rightleftharpoons \text{O}_2 + \text{OH}$	$1.50 \cdot 10^{13}$	0	950
(13)	$\text{HO}_2 + \text{OH}$	$\rightleftharpoons \text{H}_2\text{O} + \text{O}_2$	$8.00 \cdot 10^{12}$	0	0
(14)	$\text{HO}_2 + \text{HO}_2$	$\rightleftharpoons \text{H}_2\text{O}_2 + \text{O}_2$	$2.00 \cdot 10^{12}$	0	0
(15)	$\text{H} + \text{H}_2\text{O}_2$	$\rightleftharpoons \text{H}_2 + \text{HO}_2$	$1.40 \cdot 10^{12}$	0	3600
(16)	$\text{O} + \text{H}_2\text{O}_2$	$\rightleftharpoons \text{OH} + \text{HO}_2$	$1.40 \cdot 10^{13}$	0	6400
(17)	$\text{OH} + \text{H}_2\text{O}_2$	$\rightleftharpoons \text{H}_2\text{O} + \text{HO}_2$	$6.10 \cdot 10^{12}$	0	1430
(18)	$\text{H}_2\text{O}_2 + \text{M}$	$\rightleftharpoons \text{OH} + \text{OH} + \text{M}$	$1.20 \cdot 10^{17}$	0	45500
(19)	$\text{O} + \text{O} + \text{M}$	$\rightleftharpoons \text{O}_2 + \text{M}$	$6.00 \cdot 10^{13}$	0	-1800

Units are s, mol, cm³, cal and K.

Table A.5: Efficiency factors $\neq 1$ for the mechanism in Table A.4.

third bodies	Reactions				
	(5)	(6)	(7)	(8)	(18)
M = H ₂		2.0		2.0	
M = H ₂ O	6.0	6.0	5.0	16.0	15.0

Table A.6: Reaction mechanism from Ó Conaire et al. [69].

Reactions			A_r	β_r	E_r
(1)	$\text{H} + \text{O}_2$	$\rightleftharpoons \text{O} + \text{OH}$	$1.91 \cdot 10^{14}$	0	16440
(2)	$\text{O} + \text{H}_2$	$\rightleftharpoons \text{H} + \text{OH}$	$5.08 \cdot 10^4$	2.67	6292
(3)	$\text{OH} + \text{H}_2$	$\rightleftharpoons \text{H} + \text{H}_2\text{O}$	$2.16 \cdot 10^8$	1.51	3430
(4)	$\text{O} + \text{H}_2\text{O}$	$\rightleftharpoons \text{OH} + \text{OH}$	$2.97 \cdot 10^6$	2.02	1340
(5)	$\text{H}_2 + \text{M}$	$\rightleftharpoons \text{H} + \text{H} + \text{M}$	$4.57 \cdot 10^{19}$	-1.40	105100
(6)	$\text{O} + \text{O} + \text{M}$	$\rightleftharpoons \text{O}_2 + \text{M}$	$6.17 \cdot 10^{15}$	-0.50	0
(7)	$\text{O} + \text{H} + \text{M}$	$\rightleftharpoons \text{OH} + \text{M}$	$4.72 \cdot 10^{18}$	-1.00	0
(8)	$\text{H} + \text{OH} + \text{M}$	$\rightleftharpoons \text{H}_2\text{O} + \text{M}$	$4.50 \cdot 10^{22}$	-2.00	0
(9)	$\text{H} + \text{O}_2 + \text{M}$	$\rightleftharpoons \text{HO}_2 + \text{M}$	$3.48 \cdot 10^{16}$	-0.41	-1.12
	$\text{H} + \text{O}_2$	$\rightleftharpoons \text{HO}_2$	$1.48 \cdot 10^{12}$	0.60	0
(10)	$\text{HO}_2 + \text{H}$	$\rightleftharpoons \text{H}_2 + \text{O}_2$	$1.66 \cdot 10^{13}$	0	820
(11)	$\text{HO}_2 + \text{H}$	$\rightleftharpoons \text{OH} + \text{OH}$	$7.08 \cdot 10^{13}$	0	300
(12)	$\text{HO}_2 + \text{O}$	$\rightleftharpoons \text{OH} + \text{O}_2$	$3.25 \cdot 10^{13}$	0	0
(13)	$\text{HO}_2 + \text{OH}$	$\rightleftharpoons \text{H}_2\text{O} + \text{O}_2$	$2.89 \cdot 10^{13}$	0	-500
(14)	$\text{HO}_2 + \text{HO}_2$	$\rightleftharpoons \text{H}_2\text{O}_2 + \text{O}_2$	$4.20 \cdot 10^{14}$	0	11980
	$\text{HO}_2 + \text{HO}_2$	$\rightleftharpoons \text{H}_2\text{O}_2 + \text{O}_2$	$1.30 \cdot 10^{11}$	0	-1629
(15)	$\text{H}_2\text{O}_2 + \text{M}$	$\rightleftharpoons \text{OH} + \text{OH} + \text{M}$	$1.27 \cdot 10^{17}$	0	45500
	H_2O_2	$\rightleftharpoons \text{OH} + \text{OH}$	$2.95 \cdot 10^{14}$	0	48400
(16)	$\text{H}_2\text{O}_2 + \text{H}$	$\rightleftharpoons \text{H}_2\text{O} + \text{OH}$	$2.41 \cdot 10^{13}$	0	3970
(17)	$\text{H}_2\text{O}_2 + \text{H}$	$\rightleftharpoons \text{H}_2 + \text{HO}_2$	$6.03 \cdot 10^{13}$	0	7950
(18)	$\text{H}_2\text{O}_2 + \text{O}$	$\rightleftharpoons \text{OH} + \text{HO}_2$	$9.55 \cdot 10^6$	2.00	3970
(19)	$\text{H}_2\text{O}_2 + \text{OH}$	$\rightleftharpoons \text{H}_2\text{O} + \text{HO}_2$	$1.00 \cdot 10^{12}$	0	0
	$\text{H}_2\text{O}_2 + \text{OH}$	$\rightleftharpoons \text{H}_2\text{O} + \text{HO}_2$	$5.80 \cdot 10^{14}$	0	9.56

Units: s, mol, cm³, cal and K.

Reactions 14 and 19 are expressed as the sum of the two rate expressions.

Table A.7: Troe parameters for the mechanism in Table A.6.

Reactions	a	T^{***} [K]	T^* [K]	T^{**} [K]
(9)	0.5	$1.0 \cdot 10^{-30}$	$1.0 \cdot 10^{30}$	$1.0 \cdot 10^{100}$
(15)	0.5	$1.0 \cdot 10^{-30}$	$1.0 \cdot 10^{-30}$	

Table A.8: Efficiency factors $\neq 1$ for the mechanism in Table A.6.

third bodies	Reactions					
	(5)	(6)	(7)	(8)	(9)	(15)
M = H ₂	2.5	2.5	2.5	0.73	1.3	2.5
M = H ₂ O	12.0	12.0	12.0	12.0	14.0	12.0
M = Ar		0.83	0.75	0.38	0.67	0.45
M = He		0.83	0.75	0.38	0.67	0.45